

INJECTABLE CONTROLLED DELIVERY IMMUNOTHERAPIES FOR THE
TREATMENT OF MELANOMA

A Dissertation

Presented to the Faculty of the Graduate School

of Cornell University

in Partial Fulfillment of the Requirements for the Degree of

Doctor of Philosophy

by

Mintai Peter Hwang

August 2019

Copyright © by Mintai Peter Hwang

2019

INJECTABLE CONTROLLED DELIVERY IMMUNOTHERAPIES FOR THE TREATMENT OF MELANOMA

Mintai Peter Hwang, Ph.D.

Cornell University 2019

The World Health Organization estimates close to 10 million deaths each year due to cancer. In particular, melanoma is a highly aggressive and metastatic skin cancer that has nearly tripled and quadrupled in incidence since 1975 among female and male populations, respectively. The clinical mainstay for the treatment of melanoma continues to include surgical resection. While earlier treatment plans included chemotherapy in conjunction with surgery, sub-par patient responses and the recent advent of checkpoint inhibitors have shifted much of the focus towards a combinatory approach of surgery and immunotherapy. Comprised of immune-activating cytokines such as IL-2 and checkpoint inhibitors such as α PD-1 and α CTLA-4 antibodies, current immunotherapy regimens necessitate a high dose to overcome immunosuppressive tumor mechanisms. However, due to the nature of immunotherapy, in which immune activators are enhanced while inhibitors are suppressed, severe adverse effects are commonly observed. Furthermore, the high cost of immunotherapy results in an unsustainable economic model; the annual use of α PD-1 antibody alone would generate a bill of over \$1,000,000

per patient. Taken together, the use of a controlled delivery platform is highly attractive in its capacity to preserve its payload while simultaneously protecting patients against immunotoxicities.

This dissertation examines the utility of various controlled delivery platforms for different immunotherapeutic proteins including IL-12 and α PD-1 antibody. The first part examines the feasibility of using a heparin-based complex coacervate platform to deliver IL-12 in the context of a pre-clinical murine melanoma model. Our results are the first to demonstrate the use of complex coacervation to deliver proteins for anti-cancer applications and provide evidence of significantly improved responses compared to equivalent amounts of IL-12 delivered via bolus injections. The second part of the dissertation investigates the development of a novel polycation using glycine betaine as a pendant group. Our results indicate that the resulting polymer is biocompatible with anti-bacterial and anti-angiogenic properties, underscoring its potential use in anti-cancer applications. Finally, the third part of this dissertation combines the heparin-based complex coacervate with a novel shear-thinning hydrogel based on the glycine betaine-functionalized polycation. The composite platform encapsulates both IL-12 and α PD-1 antibody and is applied in a murine melanoma model. Our results highlight the combined effect of an anti-angiogenic hydrogel and the controlled delivery of immunotherapeutic proteins on improved survival and therapeutic indices. Collectively, this dissertation characterizes the development of minimally-invasive injectable immunotherapies in a preclinical melanoma model.

BIOGRAPHICAL SKETCH

Mintai Peter Hwang was born in Seoul, Republic of Korea and moved to the United States six months later with his parents. After moving back to Korea in 1995, Mintai spent five collective years in elementary, middle school, and high school, the last year of which he spent at Daewon Foreign Language High School. In 2000, Mintai moved to Seattle with his family right before his Junior year at Newport High School. Beginning in 2002, Mintai studied Biomedical Engineering at Johns Hopkins University and obtained his Bachelor of Science degree in 2006. He directly went on to pursue a Master of Science degree in Biomedical Engineering from Columbia University, where he worked in the lab of Dr. Samuel K. Sia. After graduation, Mintai moved to Seattle to pursue his passion in teaching, working as a math and science tutor for one year. In 2008, he began studying towards a doctoral degree at the University of Pittsburgh under the guidance of Dr. Steven R. Little. In 2011, shortly after his 3rd year developing biomimetic PLGA constructs as a platform to investigate bone cell interactions, Mintai returned to Korea to fulfill his mandatory military service. He was accepted into the Korea Institute of Science and Technology (KIST) as a research scientist during this time and continued to work at KIST after completion of his mandatory service. In 2015, Mintai returned to the University of Pittsburgh with a fellowship from KIST and started in the lab of Dr. Yadong Wang. Mintai transferred to Cornell University in August 2017 where he continued his research on developing controlled delivery platforms to deliver immunotherapeutic proteins for the treatment of melanoma. Mintai has authored

10 peer-reviewed articles during his time as a doctoral candidate (4 with Dr. Yadong Wang as corresponding author, 2 with collaborators, and 4 with KIST) and a total of 31 peer-reviewed publications, 1 book chapter, with 4 more in preparation.

ACKNOWLEDGEMENTS

What a journey! 11 years have passed since I first started a Ph.D., in what was anything but direct. Naturally, I've had time to think about how I've changed. There's a word in Korean that translates to '*people fortune*', meaning that one has the fortune of being surrounded by good people. That is precisely what links all the different ways I've changed for the better. And I would like to thank God for opening doors and opportunities to meet such awesome people.

I have become more patient, confident, and loving, for which I thank my family. No one has seen my struggles like my wife, Youmi, and nobody has been there for me like she has. From constant encouragement, tasty meals, drives to/from lab in the wee hours at night, to hugs, tears, and plain out silliness, I thank you and love you. I look forward to how we'll grow individually but am at ease knowing that you are there for me. I would also like to thank my Mom and Dad for raising me in an environment in which nothing ever felt deprived, even when I'm sure they couldn't afford it as Ph.D. students themselves. I would like to thank them for instilling a sense of curiosity and a drive for learning to this day. Oh, and Dad, thanks for the genes; I've lost more hair since 11 years ago. Last but not least, I thank my sister, Michelle, for being there for me when things got too stressful. I miss having you around to argue and laugh about all the small things, but am excited for what lies ahead of you. And Riley! Thanks for all the poo, pee, and dog hair. You're still cute.

I have become more experienced in science, or at least how to approach it. After all, who hasn't tried to do a ton of experiments all at once in the name

of efficiency, only to not get any reliable results because you made a mistake? I would first like to thank Dr. Wang. I remember when we randomly met in Korea at a conference, at which point we had only met a couple of times. From that meeting, you continued to offer me advice until you eventually took me on as a student; I still remember my tears of joy the night I received your acceptance email. Thank you for being open-minded to allow me the leeway to try out different ideas and thank you for your guidance with... well, everything. My appreciation for science has grown exponentially since joining as a part of your family. I couldn't have asked for a better mentor. I would also like to thank my committee members: Dr. Putnam and Dr. Singh for their valuable insight, guidance, and genuine enthusiasm to provide a learning experience. I also thank Dr. Kwideok Park at KIST for taking me on in a time of need, for fostering a caring and stimulating environment for my growth as a scientist. And how can I forget Dr. Jonghoon Choi? Thank you for always looking out for me both professionally and personally. I've only felt love from you and always look forward to our next meeting.

I have become more optimistic and still manage to have some bit of goofiness left in me. For that, I thank my friends. Thank you Mikey and Dan. You've all been there for me more than I could ever ask for and I couldn't ask for better friends. Daeho, Geunsun, Alex, In Gul hyung, thank you. I would also like to thank all my new friends here in Ithaca, from the tennis club to the 'drinking' club. I didn't know how I'd like it in Ithaca, but I am loving every bit of it thanks to you. Last but not least, I would like to express my sincerest gratitude

to all present and past members – post-doc, graduate and undergraduate – at the Biofoundry Lab. We're all in it together and I don't think I would have made it this far without all of you.

TABLE OF CONTENTS

BIOGRAPHICAL SKETCH.....	v
ACKNOWLEDGEMENTS.....	vii
TABLE OF CONTENTS	x
LIST OF FIGURES.....	xiv
LIST OF TABLES	xvi
Chapter 1. Introduction.....	1
1.1 Melanoma on the Rise.....	1
1.2 Current Treatment Methods and Obstacles.....	3
1.2.1 Surgical Resection and Chemotherapy.....	3
1.2.2 Immunotherapy	4
1.3 Controlled Delivery Platforms	9
1.4 Objectives.....	13
Chapter 2. Single Injection of Heparin-based IL-12 Complex Coacervate Inhibits B16F10 Melanoma Tumor Progression.....	16
2.1 Introduction	17
2.2 Materials and Methods	20
2.2.1 Materials	20
2.2.2 Synthesis of PEAD.....	21
2.2.3 Preparation of IL-12 Coacervates	22
2.2.4 Cryo-SEM	23
2.2.5 Stability of IL-12 in Trypsin.....	23
2.2.6 In-vitro Release.....	23
2.2.7 ELISA.....	24
2.2.8 Bioactivity Assay for IL-12 Releasates.....	24

2.2.9 Animal Studies	25
2.2.10 Immunofluorescent Sectioning and Imaging	26
2.2.11 Statistical Analysis	26
2.3 Results.....	27
2.3.1 Soluble Complex Coacervates Exhibit Coalescence	27
2.3.2 Complex Coacervates Protect and Enhance Bioactivity of IL-12.....	29
2.3.3 Single Injection of IL-12 Coacervate Inhibits Systemic Tumor Growth	32
2.3.4 Significant Lymphocyte Accumulation Observed in Tumor Environment.....	34
2.3.5 IL-12 Coacervate Treatment Increases Tumor PD-L1 Expression	38
2.4 Discussion	39
2.5 Conclusions	44
Chapter 3. A Biocompatible Betaine-functionalized Polycation for Coacervation	45
3.1 Introduction	46
3.2 Materials and Methods	48
3.2.1 Materials	48
3.2.2 B-PED Synthesis	49
3.2.3 Characterization of B-PED	49
3.2.4 Assessment of Cytotoxicity	50
3.2.5 Angiogenesis Assays	51
3.2.6 Antimicrobial Assays	52
3.3 Results and Discussion	52

3.3.1 Synthesis and Characterization of B-PED.....	52
3.3.2 Biocompatibility of B-PED	55
3.3.3 Effect of B-PED on Angiogenesis	58
3.3.4 Antimicrobial Property of B-PED.....	62
3.3.5 Complex Coacervate Behavior on B-PED.....	65
3.4 Conclusions	70
Chapter 4. Combined Delivery of IL-12 and α PD-1 Inhibitor via Single Injection of Anti-Angiogenic Hydrogel Improves Survival in Melanoma	71
4.1. Introduction.....	72
4.2 Materials and Methods	76
4.2.1 Materials	76
4.2.2 PBP and PEAD Synthesis.....	78
4.2.3 Material Characterization	80
4.2.4 IgG Coacervate Preparation	80
4.2.5 Cell Culture and Proliferation Assay	81
4.2.6 In-vitro and In-vivo Angiogenesis Assay	81
4.2.7 PBP Hydrogel Preparation.....	82
4.2.8 PBP Hydrogel Characterization and Optimization.....	83
4.2.9 Animal studies.....	84
4.2.10 Flow Cytometry	85
4.2.11 ELISA.....	87
4.2.12 Tissue Staining and Imaging	88
4.2.13 Image and Statistical Analysis	89
4.3. Results and Discussion	90
4.3.1 PBP Synthesis and Characterization	90
4.3.2 PBP Inhibits In-vitro and In-vivo Angiogenesis.....	93

4.3.3 Optimization of PBP-based Hydrogel.....	98
4.3.4 Hydrogel Delivery of IL-12 and α PD-1 Antibody Prolongs Survival in B16F10 Melanoma Model	105
4.3.5 PBP Treatment Inhibits B16F10 Intratumoral Angiogenesis and Induces Tumor Apoptosis	113
4.3.6 Innate and Adaptive Immune Response Plays a Role in Tumor Inhibition	118
4.5 Conclusions	129
Chapter 5. Conclusions and Future Directions	130
Chapter 6. References	136

LIST OF FIGURES

Figure 1. Cancer is a Leading Cause of Death in High HDI Areas.	2
Figure 2. Effective Cancer Immunity Cycle.....	6
Figure 3. Negative Regulation of T cells by Immune Checkpoints.	8
Figure 4. Heparin-based Complex Coacervate Behavior.	28
Figure 5. Coacervate Protects and Enhances IL-12 Bioactivity.....	30
Figure 6. Heparinase II-mediated Degradation of Heparin.	31
Figure 7. Dose Escalation Study of IL-12 Coacervates.	33
Figure 8. Contralateral Tumor Growth for Dose Escalation Study.....	34
Figure 9. IL-12 Delivery Significantly Inhibits Systemic Tumor Growth.	35
Figure 10. Tumor Growth Curves for Individual Mice.	36
Figure 11. IL-12 Coacervates Improve Intratumoral Innate and Adaptive Immune Response.	37
Figure 12. Quantification of Intratumoral CD4+FoxP3+ Treg Cells.	38
Figure 13. IL-12 Coacervates Increase Tumor PD-L1 Expression.	40
Figure 14. B-PED characterization.	53
Figure 15. B-PED Synthesis.....	54
Figure 16. Zeta Potential of B-PED.	55
Figure 17. B-PED biocompatibility.....	56
Figure 18. Toxicity of Betaine.	57
Figure 19. Effect of Betaine on <i>In-vitro</i> Angiogenesis.....	59
Figure 20. B-PED Effect on Angiogenesis.....	60
Figure 21. Antimicrobial Activity of B-PED.....	63
Figure 22. [B-PED] vs. Size.....	66
Figure 23. Complex Coacervation of B-PED and Heparin.....	67
Figure 24. B-PED Complex Coacervate Behavior in Varying [NaCl].	69
Figure 25. Antibody Does Not Load Into Complex Coacervates.	75
Figure 26. Fourier Transform Infrared Spectroscopy of mPEG-COOH.	90
Figure 27. PBP Synthesis and Characterization.....	92
Figure 28. Nucleic Acid-based Toxicity of [PBP].	95
Figure 29. PBP Restricts <i>In-vitro</i> and <i>In-vivo</i> Angiogenesis.	96

Figure 30. PBP Hydrogel Optimization.....	100
Figure 31. PBP Hydrogel Gelation Kinetics.....	103
Figure 32. PBP Titration with Varying Mass Ratios of Heparin.....	103
Figure 33. <i>In-vitro</i> Release Profile of IL-12 and IgG.	106
Figure 34. Controlled Delivery of IL-12/ α PD-1 Antibody <i>In-vivo</i>	107
Figure 35. Metastasis of B16F10 Melanoma to dLN.	111
Figure 36. Controlled Delivery of IL-12/ α PD-1 Antibody Inhibits Angiogenesis and Promotes Apoptosis/Necrosis of Tumor.	114
Figure 37. Controlled Delivery of IL-12/ α PD-1 Antibody Inhibits Tumor Lymphangiogenesis.	117
Figure 38. Number of Intratumoral LECs is Not Affected by Treatment.	119
Figure 39. Controlled Delivery of IL-12/ α PD-1 Antibody Increases Apoptotic/Necrotic Areas.....	120
Figure 40. Increased Apoptotic/Necrotic Areas by Treatment Continues into D10 Post-treatment.....	121
Figure 41. Controlled Delivery of IL-12/ α PD-1 Antibody Affects Early Immune Response Mediated by NK Cells.....	123
Figure 42. Controlled Delivery of IL-12/ α PD-1 Antibody Affects Adaptive Immune Response Mediated by CD8 α T Cells.....	125
Figure 43. Representative Gating Strategy.	127
Figure 44. Effect of Immune Cell Knock-down on Survival of Mice.	128

LIST OF TABLES

Table 1. Ranking the Prevalence of Melanoma.....	3
Table 2. Immunotherapy Treatment and Adverse events.....	10
Table 3. [NaCl] vs Coacervate Size and PDI.....	70

Chapter 1.

Introduction

Melanoma is the deadliest form of skin cancer and is rapidly increasing in its incidence. This chapter will examine the emergence of melanoma, current clinical practices including surgical resection, chemotherapy, and immunotherapy, their obstacles, controlled delivery platforms, and the proposed objectives of this work.

1.1 Melanoma on the Rise

The World Health Organization estimates approximately 40.5 million deaths each year due to non-communicable diseases, of which cancer accounts for over 22% of the fatalities [1]. While research and development undeniably continues to improve the survival index of certain cancers, the global mortality rate of cancer in highly-developed areas of the world now surpasses that of cardiovascular diseases as the leading cause of death (**Figure 1**) [2]. In particular, skin cancer constitutes nearly 80% of all diagnoses; approximately 5.5 million out of 7.1 million cancers diagnosed in 2017 were found to be of the skin [3]. The bulk of these skin cancers include relatively benign carcinomas such as those of basal cells and squamous cells and are generally easily cured. Melanoma, however, is a highly aggressive and metastatic skin cancer. Unfortunately, it's incidence has been on the rise in the United States since 1975 for both male and female populations, which is in stark contrast to the

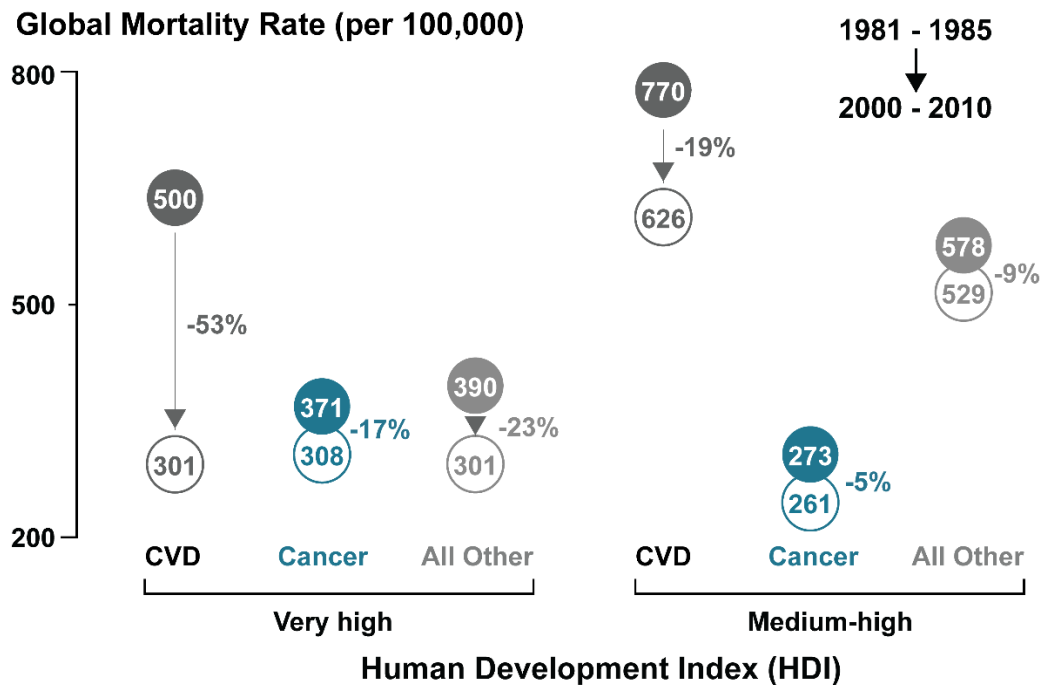


Figure 1. Cancer is a Leading Cause of Death in High HDI Areas. Cardiovascular disease (CVD)-related deaths predominated the early 1980's. Over time, however, the decline of CVD-related mortality led to the emergence of cancer as the leading cause of death in very high human development index (HDI) areas. Adapted with permission from [2].

decline of other cancers such as prostate, breast, and lung cancers [4]. Furthermore, cases of melanoma are widespread when compared to all other cancers. In particular, among males and females between 30-49 years old, melanoma ranks as the first and second-most prevalent cancer, respectively, thereby underscoring its pervasiveness in society (**Table 1**).

Table 1. Ranking the Prevalence of Melanoma.Melanoma prevalence demonstrates widespread influence. Data collected and analyzed from [4].

Age	Male	Female
30-39	1	2
40-49	1	2
50-59	2	2
60-69	2	3

1.2 Current Treatment Methods and Obstacles

Melanoma is staged according to a combination of various clinical indices such as the thickness of the primary tumor and the presence of lymph node and distance metastasis. While stage 0 melanoma is highly curable due to its confinement within the epidermal layer of skin, increasing stages of melanoma yield progressively worse 10 year survival rates with Stage 4 melanoma bottoming out at under 10% [5].

1.2.1 Surgical Resection and Chemotherapy

Surgery to remove the tumor mass, once viewed as unnecessary for late and advanced metastatic melanoma, continues to remain the mainstay in the clinic. Generally preceded by a skin and lymph node biopsy, surgery is particularly efficacious for early-stage melanomas yet still require wider excisions than the tumor mass to ensure all of the tumor is resected. The surgical resection of the primary tumor, however, may not offer the safest mode of treatment as melanoma can also develop near nerves and major blood vessels, all of which can lead to surgical complications. Additionally, while the

removal of the immunosuppressive environment present in tumors could confer treatment benefits, immune cells with active anti-tumor activities are also eliminated. Along these lines, excessive removal of lymph nodes during resection effectively reduces the patient's immune capacity – immune activation occurs in lymph nodes – and can lead to side effects such as lymphedema. Apart from surgery, chemotherapy was once a major mode of therapy. Dacarbazine, an alkylating agent to methylate DNA, is currently the only FDA-approved drug for melanoma and has seen decreased use since its approval in 1974; 5 year survival rates are under 2-6% with complete responses observed in less than 5% of patients [6]. The general ineffectiveness of dacarbazine – and other drugs including paclitaxel and tamoxifen – has been shown to stem from the inherent refractory nature of melanoma cells towards apoptosis [7]. Not surprisingly, combinations of dacarbazine with other chemotherapy drugs and with immunotherapeutic proteins such as interleukin 2 and interferon- α show limited improvement in response and survival at the cost of increased side effects [8].

1.2.2 Immunotherapy

For an anti-cancer immune response to be effective, a series of events need to be initiated beginning with neoantigen release from cancer cells via apoptosis. (**Figure 2**) [9]. Natural killer (NK) cells play a dominant role in inducing such apoptosis. Specifically, they generate a granzyme-B-mediated early response to cancer by recognizing the reduced expression of MHC class I molecules on tumor cells. Furthermore, the concurrent release of interferon-

gamma (IFN- γ) from activated NK cells contributes to further induction of adaptive anti-cancer responses [10]. Tumor antigens released from apoptotic cancer cells are then taken up by antigen presenting cells including dendritic cells, which present them to naïve T cells. Primed T cells then traffic their way to the tumor, recognize the antigen for which they were activated for, and mediate IFN- γ killing of cancer cells. The subsequent release of more neoantigens broadens the range of the adaptive immune response with each iteration of the cycle. Each step in this anti-cancer response involves the coordination of numerous factors, both of inhibitory and stimulatory nature. Subsequent patient responses to the aforementioned surgical resection and chemotherapy have shifted much of the clinical focus towards the use of immune-modulating proteins, with the aim of manipulating each step in the cancer immunity cycle in what is called immunotherapy.

Earlier immunotherapies approved by the FDA include interleukin2 (IL-2) and interferon-alpha (IFN- α). In particular, IL-2 is a cytokine that has been shown to increase T cell and NK cell activation and was initially approved for the treatment of metastatic renal cancer [11]. High-dose IL-2 treatment via intravenous injection was approved for melanoma afterwards in 1998, undeniably yielding an improved response rate of up to 19.7% compared to single agent treatment regimens using dacarbazine [12, 13]. Numerous subsequent studies on the utility of IL-2 *in-vivo*, however, demonstrated its redundancy as other immune-activating proteins such as interleukin-12 (IL-12)

or interleukin-15 (IL-15) were shown to compensate for the lack of IL-2 [14, 15]. More importantly, IL-2 plays opposing roles in the context of cancer, in which it

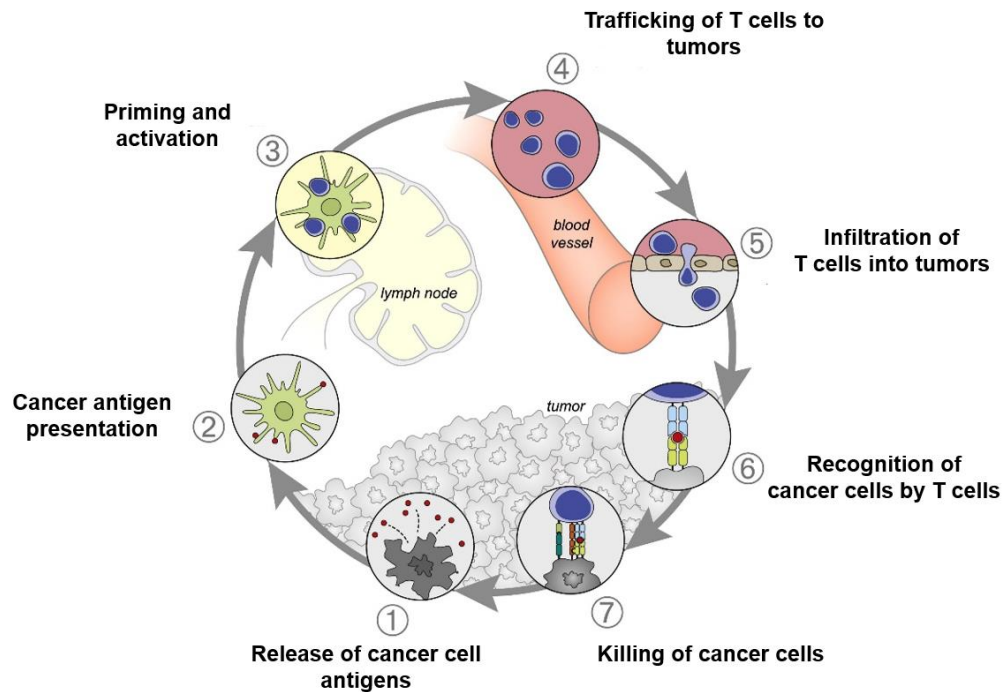


Figure 2. Effective Cancer Immunity Cycle. An efficient anti-cancer immune response that involves T cells is cyclic and in principle should provide progressively robust immunity with each iteration of the cycle. Adapted from [9].

is a non-redundant factor in the proliferation of cancer-promoting regulatory T cells (Treg cells) [16, 17]. Furthermore, high doses of IL-2 are required (e.g. 15 intravenous doses of up to 720,000 IU/kg over 5 days [18]), which potentially leads to severe side effects including multiorgan toxicity and capillary leak syndrome. Despite these downsides, the use of IL-2 is significant in that it represents one of the earliest forms of immunotherapy.

Recent advances made in the understanding of how T cells are activated and regulated have led to the emergence of checkpoint inhibitors, the use of

which is the preferred treatment in the current clinical landscape. Two major checkpoints involved in the negative regulation of anti-cancer T cell activity are the CTLA-4/CD86 and PD-1/PD-L1 pathways (**Figure 3**) [19]. CTLA-4 on T cells binds to both CD80 and CD86 on dendritic cells (DCs), and acts as a competitor for CD28, which together with CD80 and CD86 constitute the second signal required for T cell activation. With a higher affinity for CD80 and CD86 than CD28, CTLA-4 effectively increases the activation threshold for T cells and results in downregulation of the immune response. Thus, CTLA-4 antagonization via checkpoint inhibitors downregulates the inhibition of T cell activation by DCs. The use of CTLA-4 checkpoint inhibitors also affects Treg cells as CTLA-4 deficient-mice have been shown to impair Treg suppressive function *in-vivo* by preventing downregulation of CD80 and CD86 on DCs [20]. Despite these promises, the use of α CTLA-4 antibodies yields only a modest improvement in overall response (15.2%) compared to the use of dacarbazine (10.3%) [21]. The PD-1/PD-L1 interaction primarily occurs between T cells and tumor cells, though the expression of PD-1 and PD-L1 is not unique to T cells and tumor cells, respectively; PD-1 is also present on macrophages [22], DCs [23], and tumor cells [24] while PD-L1 is also present on various immune cell subsets [25, 26]. Nonetheless, the efficacy of checkpoint inhibitors against PD-1 have proven to be successful in the context of dacarbazine and α CTLA-4 antibodies, with response rates up to 40% [27].

It is important to note that current treatment regimens deliver immunotherapeutic proteins via bolus intravenous infusions. The general ineffectiveness of such bolus injections at lower doses necessitates a high-risk

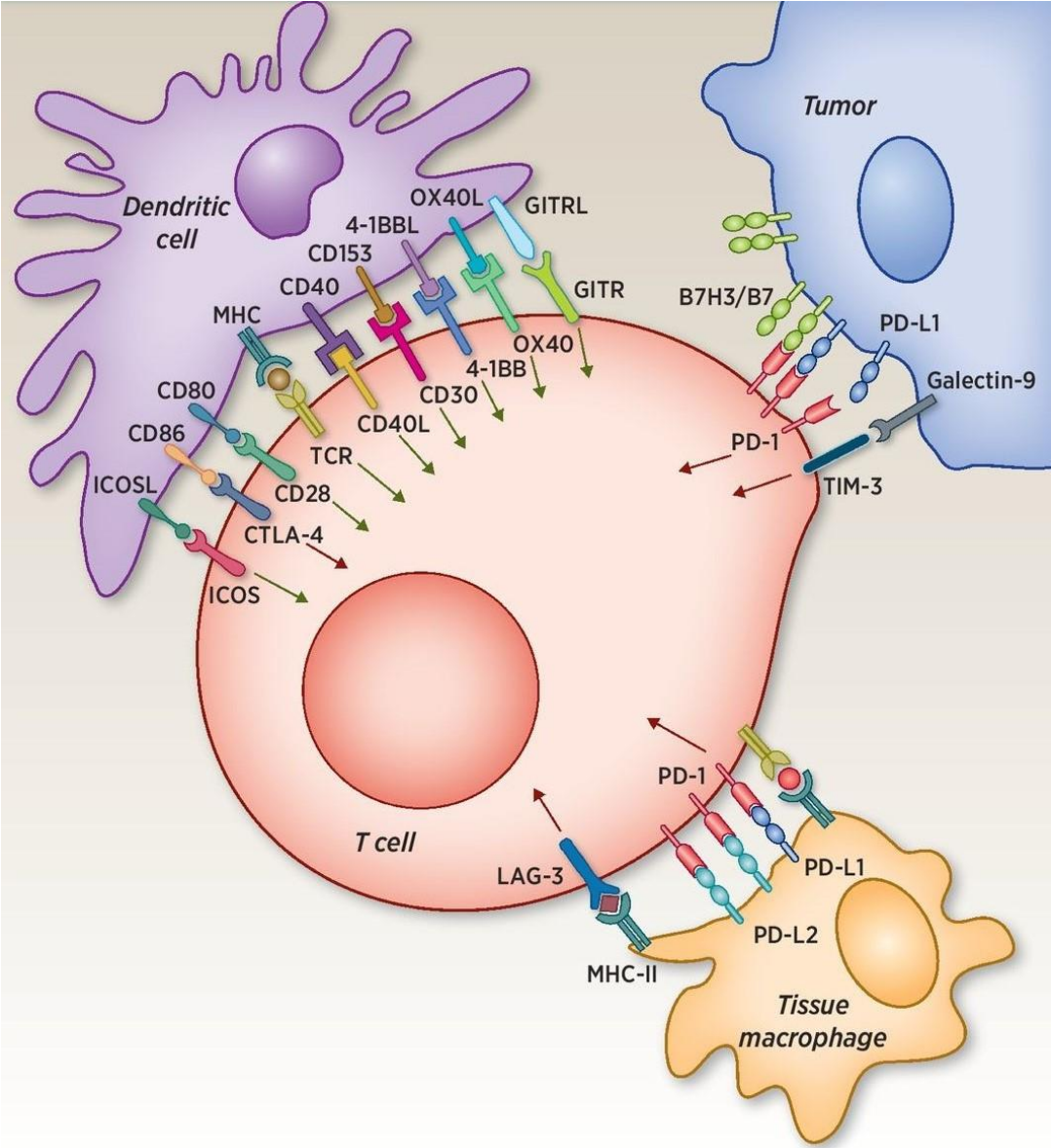


Figure 3. Negative Regulation of T cells by Immune Checkpoints.CTLA-4 and PD-1 are major checkpoints that negatively regulate T cell activation by DCs and their activity on cancer cells. Adapted from [19].

dose (**Table 2**). For instance, IL-2 requires an upwards of over 34 $\mu\text{g}/\text{kg}$ dose, with up to 15 doses (assuming a specific activity of 2.1×10^4 IU/ μg of hIL-2 [28]). Not surprisingly, a variety of severe adverse responses are observed such as hypotension [29], the primary result of capillary leak syndrome that results from the IL-2-induced cytokine storm. To mitigate the potential for such adverse events, IL-2 is only given only in specialized treatment centers where the patient's progress can be monitored over time. Checkpoint inhibitors also require high doses to ensure therapeutic efficacy at target sites after systemic clearance, non-specific binding, and extravasation to the target. While treatment with checkpoint inhibitors do not lead to as many patients with side effects as observed with those receiving IL-2 treatment, severe adverse responses that include nausea, diarrhea, fatigue, pruritus, colitis are observed in a non-substantial proportion of patients [30]. Aside from safety concerns of immunotherapy, its high cost results in an unsustainable economic model. For example, the combined use of $\alpha\text{CTLA-4}$ and $\alpha\text{PD-1}$ checkpoint inhibitors for a typical patient would be close to \$300,000 with a projected annual cost of \$173.9 billion to society; bi-weekly treatments for one year with only $\alpha\text{PD-1}$ antibody alone would generate an annual bill of over \$1,000,000 per patient [31].

1.3 Controlled Delivery Platforms

Immunotherapy has made considerable strides with regards to target discovery, validation, and optimization. However, generalization of the obstacles previously described for IL-2 and checkpoint inhibitors collectively point towards common challenges facing immunotherapy. Cytokines such as

Table 2. Immunotherapy Treatment and Adverse events. α CTLA-4 variants include ipilimumab and α PD-1 variants include nivolumab and pembrolizumab.

Drug	Treatment Dose	Treatment Regimen	\geq Grade 3 Adverse Response
IL-2	600,000-720,000 IU/kg	Two cycles, each consisting of once every 8 hours for 5 consecutive days; up to 15 doses per cycle	92.6% (hypotension) [29]
α CTLA-4 variants	3-10 mg/kg	Once every 2-3 weeks	27.3% (all events) [30]
α PD-1 variants	3-10 mg/kg	Once every 2-3 weeks	16.3% (all events) [30]

IL-2 suffer from an extremely short half-life (e.g. just over a few minutes [32]) and consequently require high doses to maintain therapeutic efficacy. While therapeutic intervention is successful in activating the immune response for IL-2 as well as other immunotherapies, a corresponding increase in cytokines such as IFN- γ and tumor necrosis factor alpha (TNF- α) results in hypotension and renal dysfunction among other potentially lethal toxicities [33]. On a similar note, immunotherapy in its current form can elicit autoimmunity due to the nature of removing immune inhibitory factors [34], underscoring the need to better control global doses. Indeed, locally-concentrated forms of immunotherapy have been shown to be as effective, if not more, than systemically-delivered treatments [35]. From these perspectives, the delivery of immunotherapeutics via controlled delivery platforms is highly attractive.

The primary goal of the controlled delivery of immunotherapeutics is to enable higher targeting efficiency while reducing off-target effects. Apart from the alleviation of single agent dose-related toxicities, the use of controlled

delivery could have ramifications in combination treatments. For example, combinations of checkpoint inhibitors such as α CTLA-4 and α PD-1 antibodies improve overall patient response yet result in increased toxicities; 53% of patients experience a synergistic severe adverse event (\geq Grade 3) compared to 27.3% and 16.3%, respectively [30, 36]. By utilizing a controlled delivery platform, such otherwise toxic combinations could be administered to a broader range of patients who otherwise may not have been healthy enough to receive the treatment in its current clinical form.

A number of modalities are being investigated as controlled delivery platforms, of which the use of FDA-approved poly(lactic-co-glycolic-acid) (PLGA) and its derivatives are most common. Particulate forms have been used to encapsulate various cytokines for cancers not limited to melanoma. For example, α CD40 and α CTLA-4 antibodies were encapsulated in poly(D,L lactic-co-hydroxymethylglycolic acid) (PLHMGA) and showed efficacy against colon cancer [37]; PLHMGA was used as a means to reduce acidification commonly observed in PLGA. In another example, IL-12 and granulocyte-macrophage-colony-stimulating factor (GM-CSF) were encapsulated into PLGA microparticles and demonstrated superior efficacy in a colon tumor model [38]. Materials other than PLGA derivatives such as Montanide ISA 51, a commercially-available mixture of mineral oils, have also been used to encapsulate and deliver α CTLA-4 antibodies to improve outcomes in colon cancer. Implantable scaffolds represent another platform to deliver immunotherapeutic proteins. For example, poly(lactide-co-glycolide) (PLG)

scaffolds were fabricated to prophylactically deliver a combination of GMCSF and tumor lysates to affect the immune response in a melanoma model [39, 40]. Finally, injectable materials constitute an alternative mode of controlled delivery. In a recent study, reactive oxygen species (ROS)-responsive PVA scaffolds were used to encapsulate gemcitabine and α PD-L1 antibody, in which α PD-1 antibody release inhibited melanoma recurrence in the context of surgical resection of the primary tumor [41].

Collectively, while these modalities demonstrate the utility and practicability of controlled delivery, many undergo a deleterious fabrication processes such as sonication-based double emulsification utilized in the fabrication of PLGA microparticles. Furthermore, PLGA degrades into acidic by-products, which accelerates degradation and loss of bioactivity of the payload. On a separate note, scaffolds require implantation and thus may not be a viable option for all patients. Finally, there are a limited number of studies that extensively examine the use of controlled delivery platforms to treat melanoma, which is notorious for its highly aggressive behavior, in a pre-clinical therapeutic setting (*i.e.* non-prophylactic).

For more information on techniques for the delivery of immunotherapeutic agents other than proteins (*e.g.* vaccines, engineered cells, and genes), we refer readers to recent reviews that discuss controlled delivery platforms for the treatment of cancers [42, 43].

1.4 Objectives

We have previously developed a heparin-based complex coacervation platform, which utilizes the natural affinity of heparin for a large number of proteins [44]; this affinity drives the high encapsulation efficiencies observed with our platform. The combination of protein:heparin complexes with a polycation results in the instantaneous formation of a polymer-rich soluble phase, from which proteins can be delivered in a controlled manner. By virtue of heparin complexation and subsequent sequestration into a polymer-rich phase, proteins are protected from potentially harsh environments, effectively extending their half-lives. We have reported on the efficacy of the coacervate platform on angiogenesis [45], wound healing [46], and myocardial regeneration [47, 48], but have not yet determined its application towards anti-cancer therapy. This dissertation first seeks to assess the feasibility of using complex coacervates to deliver IL-12 as a mode of therapy for melanoma. IL-12 is an immune activating cytokine not unlike IL-2. Initially discovered as a natural killer (NK) cell stimulatory factor, IL-12 plays important roles in both the innate and adaptive immune responses [49]. In the second aim of this dissertation, we will then attempt to improve upon the anti-cancer capacity of the delivery vehicle through deliberate design of a novel polycation. Finally, in the last aim, we will combine both the complex coacervate system with a novel anti-angiogenic shear-thinning hydrogel with properties derived from the polycation in the second aim. The platform will be used to encapsulate both IL-12 and α PD-1

antibody for the delivery of immunotherapeutic proteins in a preclinical melanoma model. The aims of this dissertation are as follow:

Aim 1. To explore the feasibility of coacervate-mediated IL-12 delivery to inhibit melanoma growth. We have previously demonstrated the use of a heparin-based coacervate system to deliver therapeutic proteins for a wide variety of applications [45-48]. The coacervate delivery system will be evaluated for its potential to mediate an anti-tumor response via the local delivery of IL-12 and will be compared to that of bolus IL-12 injections. The IL-12 releasate is expected to induce stronger innate and adaptive immune responses than bolus IL-12 injections, resulting in a significant reduction of melanoma growth in a preclinical murine B16F10 model.

Aim 2. To synthesize a novel polycation that can be used in anti-cancer applications. Glycine betaine is a naturally-occurring amino acid ubiquitously present in human plasma [50] with a vast range of benefits that include anti-cancer potential [51-53]. The betaine compound contains a cationic quaternary ammonium group, rendering it a potential replacement for arginine, which forms the basis for the cationic macromolecule used to form complex coacervates together with anionic heparin. The new cationic polymer is expected to be biocompatible with the potential to be used in anti-cancer applications.

Aim 3. To co-deliver IL-12 & α PD-1 antibody from a shear-thinning hydrogel to treat melanoma. The combination of cytokines and checkpoint inhibitors is emerging as a viable therapeutic option for various cancers. The

betaine-containing polycation characterized in the previous aim will be modified with poly(ethylene glycol) to accommodate for cyclodextrin-based physical crosslinks. The resulting shear-thinning hydrogel will provide a platform from which both heparin-binding and non-heparin-binding proteins can be delivered. The hydrogel will be assessed for its anti-angiogenic behavior as well as its capacity to deliver IL-12 and α PD-1 antibody in a preclinical syngeneic murine melanoma model.

Chapter 2.

Single Injection of Heparin-based IL-12 Complex Coacervate Inhibits

B16F10 Melanoma Tumor Progression

Melanoma is the deadliest type of skin cancer with the fastest increasing incidence rate among all solid tumors. Conventional modes of therapy such as chemotherapy yield a low response rate despite various adverse side effects. More recently, immunotherapy has emerged as a viable alternative. Comprised of immune-activating cytokines such as IL-2 and checkpoint inhibitors such as α PD-1 antibody, current treatment regimens utilize intravenous infusions. Unfortunately, such bolus injections require a high dose to mitigate the immunosuppressive tumor mechanisms, which can then lead to serious adverse effects and unsustainable economic costs. Consequently, injectable controlled delivery platforms for such immunotherapeutic factors is highly attractive. In particular, complex coacervation presents a biocompatible platform compared to other modes of controlled delivery. In this study, we encapsulate IL-12 in a heparin-based complex coacervation platform. The IL-12 complex coacervate system is tested on an aggressive pre-clinical B16F10 melanoma model and to the best of our knowledge, is the first application of complex coacervate-mediated delivery of proteins for anti-cancer therapeutics.

2.1 Introduction

Cancer continues to be a leading cause of death according to the World Health Organization [1] and now surpasses cardiovascular-related diseases as the leading cause of death in areas with high development [2]. In particular, melanoma is a highly aggressive and deadly skin cancer and its incidence continues to rise in stark contrast to the decline of other cancers such as prostate, breast, and lung cancers [3]. Surgical resection continues to remain the clinical mainstay. Conventional modes of chemotherapy such as the use of dacarbazine yield low response rates with 5 year survival rates between 2-6% [6]. This general ineffectiveness stems from the inherent refractory nature of melanoma cells towards apoptosis [7].

More recently, immunotherapy has emerged as a viable alternative. In particular, seminal advances made in the field of T cell immunology [54-56] have led to the emergence of checkpoint inhibitors, the use of which is now the preferred treatment in the current clinical landscape. CTLA-4 and PD-1/PD-L1 are two checkpoints commonly targeted to induce anti-cancer T cell activity, with improved patient response rates of 15.2% [21] and up to 40% [27], respectively. However, these early achievements have been tempered by the limited number of patients that respond to the therapy, and there is increasing evidence that checkpoint inhibitors alone are insufficient to elicit therapeutic efficacy [57-60]. Notably, given that the mechanism behind therapeutic efficacy involves T cells and other immune cells, their presence in the tumor then is a prerequisite for checkpoint inhibition.

In this context, combination treatments with immune-activating cytokines such as IL-2 may provide the groundwork for further improvement in patient response. Interestingly, early variants of immunotherapy – before the advent of checkpoint inhibitors – included IL-2, which was approved by the FDA for melanoma in 1998 [11]. Unfortunately, treatment regimens utilize high intravenous doses to mitigate immunosuppressive tumor mechanisms; assuming a specific activity of 2.1×10^4 IU/ μg of hIL-2 [28], over 34 $\mu\text{g}/\text{kg}$ is given per dose, with up to 15 doses per 5 day treatment cycles [18]. Not surprisingly, a variety of severe adverse responses (\geq grade 3) are observed due to the IL-2-induced cytokine storm [29]. In addition, numerous subsequent studies on the utility of IL-2 *in-vivo* demonstrated its redundancy as other immune-activating proteins such as IL-12 or IL-15 were shown to compensate for the lack of IL-2 [14, 15]. Furthermore, IL-2 was shown to play opposing roles in the context of cancer, in which it is a non-redundant factor in the proliferation of cancer-promoting Treg cells [16, 17].

Similar to IL-2, IL-12 is a cytokine that elicits IFN- γ production as a basis for its anti-tumor activity. Unlike IL-2, however, IL-12 has a longer half-life (12 hours [61] vs. minutes for IL-2 [32]). In addition, while IL-2 has been shown to induce the expansion of cancer-promoting CD4+CD25+Foxp3+ regulatory T cells (Treg) [62], IL-12 mediates the reversal of such Treg immunosuppression [63]. Despite these advantages, initial clinical trials utilizing IL-12 were stopped due to severe toxicity in a number of patients, subsequently leading to the emergence of gene-based delivery of IL-12 [64]. Advances have been made in

the field, yet are counterbalanced by poor transfection efficiencies that continue to limit its potential. Given that clinical trials using recombinant IL-12 were stopped due to systemic toxic effects, the local delivery of IL-12 via a controlled delivery vehicle should provide for a more efficient strategy. Additionally, the amount of IL-12 available at the tumor site has been shown to be critical in determining tumor regression [65], further underscoring the need to maximize the dose of IL-12 at the tumor site without increasing systemic concentrations.

From these perspectives, complex coacervation presents an attractive alternative that can overcome such complications. Complex coacervates are characterized by short-range [66] and long-range electrostatic interactions [67] that lead to a soluble polyelectrolyte-rich phase that is amenable to injections. Our lab has previously developed a heparin-based complex coacervation platform [44], which utilizes the natural affinity of heparin for a large number of proteins. The combination of protein-heparin complexes with cationic poly(ethylene argininy laspartate diglyceride) (PEAD) results in the instantaneous formation of a polymer-rich soluble phase from which proteins are delivered. The use of heparin confers excellent biocompatibility and biomimetic properties. Indeed, IL-12 bound to heparin [68] has been shown to increase its bioactivity by more than 6-fold compared to unbound naked IL-12 [69]. While we have reported on the efficacy of the coacervate platform on angiogenesis [45], wound healing [46], and myocardial regeneration [47, 48], we have yet to determine its application towards anti-cancer therapy. Furthermore, this work is the first to examine the concept of complex

coacervation-based delivery of recombinant proteins for anti-cancer applications. Herein, we present evidence of significantly improved responses using IL-12-loaded complex coacervates and aim to address a need in the localized delivery of immunotherapeutic proteins.

2.2 Materials and Methods

2.2.1 Materials

Ethylene glycol diglycidyl ether (EGDE) (Pfaltz & Bauer, Waterbury, CT), N-Boc-L-aspartic acid (Boc-Asp-OH), and N-Boc-L-arginine (Boc-Arg-OH) (Bachem Americas Inc.), tetra-*n*-butyl-ammonium bromide (TBAB, 98%+), trifluoroacetic acid (TFA, ≥99.5%), anhydrous dimethylformamide (DMF, ≥99.9%), *N,N'*-dicyclohexylcarbodiimide (DCC, ≥99%), and 4-(dimethylamino)pyridine (DMAP, ≥99%) (Alfa Aesar, Ward Hill, MA), *N*-hydroxysuccinimide (NHS, ≥98.0%) (Acros Organics, Geel, Belgium), ethyl ether and dichloromethane (Pharmco-Aaper), heparin sodium USP (Scientific Protein Labs, Waunakee, WI), DMEM-high glucose supplemented with GlutaMAX, RPMI 1640 supplemented with L-glutamine and phenol red, 2.5% trypsin with no phenol red and EDTA, 0.25% trypsin-EDTA, protease and phosphatase inhibitor mini tablets-EDTA free, Nunc MaxiSorp flat-bottom plates, goat anti-rat-Alexa Fluor 488, goat anti-rabbit-Alexa Fluor 647, BSA-Alexa Fluor 647, and Cytoseal 60 (Thermo Fisher Scientific, Waltham, MA), 96-well round bottom plates (Corning, Corning, NY), Eppendorf LoBind tubes (Eppendorf North America, Hauppauge, NY), B16F10 melanoma cells (ATCC, Manassas, VA), penicillin-streptomycin (Lonza, Basel, Switzerland), recombinant murine IL-12 p70 (Peprotech, Rocky Hill, NJ), mouse

IL-12 p70 antibody, mouse IL-12 biotinylated antibody, streptavidin-HRP, and substrate reagent pack (R&D Systems, Minneapolis, MN), mouse IFN- γ OptEIA ELISA kit, rat anti-mouse CD8 α (clone 53-6.7), rat anti-mouse CD4, and rat anti-mouse NKp46 (clone 29A1.4) (BD, San Jose, CA), bacteroides heparinase II (New England Biolabs, Rowley, MA), FoxP3 rabbit mAb (Cell Signaling Technology, Danvers, MA), and rabbit α PD-L1 (Abcam, Cambridge, MA) were all used as received.

2.2.2 Synthesis of PEAD

PEAD was synthesized as previously described with minor modifications [70]. Briefly, EGDE (1000 mg), Boc-Asp-OH (1338.8 mg), and TBAB (5 mg) were dissolved in 0.6 mL DMF. The mixture was reacted for 20 minutes at 120°C in a microwave reactor (Biotage, Uppsala, Sweden). The resulting intermediate polymer, poly(ethylene boc-aspartate diglyceride) was precipitated in ethyl ether overnight. The solvent was removed *via* rotary evaporation and dissolved in 20 mL DCM. Boc was removed by adding 5 mL of TFA dropwise ([TFA] = 2.5mM) and incubating for 2 hours at room temperature under stirring conditions. The solvent was subsequently removed with rotary evaporation and precipitated into ethyl ether. Multiple precipitation steps in ethyl ether were carried out to remove excess reagents, DMF, and TFA. The deprotected (PED) was then washed overnight in ethyl ether and dried under vacuum until further use. PEAD was prepared by combining PED (1000 mg), Boc-Arg-OH (1071.2 mg), NHS (449.4 mg), DCC (1047.4 mg), and DMAP (23.85 mg) in DMF and stirring at room temperature under N₂ for 24 hours. The resulting insoluble dicyclohexylurea by-

product was removed using centrifugation and filtration (0.22 μm). PEAD-boc was then precipitated into ethyl ether overnight. To remove the boc group, the solvent was removed via rotary evaporation, the resulting polymer was dissolved in 11 mL DCM, and 3 mL of TFA was added dropwise. The solution was stirred at room temperature for 2 hours. The solvent was subsequently removed via rotary evaporation and the deprotected final product was dissolved in 5 mL of methanol. At least three precipitation steps were carried out in ethyl ether, followed by two washes in ethanol. The final product was dissolved in deionized water and lyophilized for at least 72 hours before use.

2.2.3 Preparation of IL-12 Coacervates

10 mg/mL PEAD and heparin solutions were prepared in 0.9% saline and sterile filtered (0.22 μm). 5.5:1 mass ratios between PEAD:heparin were utilized based on their isoelectric charge as assessed via dynamic light scattering (data not shown). For stability and *in-vitro* release studies, 200 μL of complex coacervate was prepared, in which 1 μL of IL-12 was mixed with 33.3 μL of heparin. 166.7 μL of PEAD was then added to the IL-12-heparin complex to induce coacervation. For *in-vivo* studies, each mouse received 50 μL of treatment consisting of 25 μL protein and 25 μL coacervate. To prepare the samples, 6.4 μL of heparin solution was mixed with varying amounts of IL-12 in a total volume of 8.3 μL , after which 35.3 μL of PEAD was added. IL-12 coacervate samples were prepared immediately before injection and any aggregated coacervate phase was gently resuspended by flicking the tube.

2.2.4 Cryo-SEM

Cryo-SEM images were taken using an FEI Strata 400 STEM FIB.

2.2.5 Stability of IL-12 in Trypsin

Complex coacervates were loaded with 100 ng of murine IL-12 p70 for each sample (n=4). Samples were centrifuged after which the supernatant was collected for subsequent ELISA analysis. 100 μ L of 500 ng/mL trypsin was then added to the IL-12 coacervates or to 100 ng of IL-12 suspended in PBS and incubated for 0, 1, or 10 hours. At each time point, 100 μ L of 1X protease inhibitor solution was added and incubated for 5 minutes at room temperature. To break apart the complex coacervate, 50 μ L of heparinase cocktail solution (1 μ L of 4000 units/mL Bacteroides Heparinase II, 25 μ L Bacteroides Heparinase reaction buffer, and 24 μ L of 20X PBS) was added to each sample and further incubated for 1 hour at 37°C. Samples were subsequently frozen at -20°C until analysis via ELISA.

2.2.6 In-vitro Release

IL-12 loaded complex coacervates were prepared as described above. Each sample was loaded with 500 ng of murine IL-12 p70 (n=3). For the group loaded with both IL-12 and BSA, 0.1% BSA in saline was used to dilute IL-12. 0.9% saline without BSA was used for all other preparations. After initial formation of the complex coacervates, samples were immediately centrifuged to induce their coalescence. The supernatant was collected and analyzed via ELISA to indirectly assess loading efficiency. The coacervate pellet was gently resuspended in 0.1% BSA in saline for subsequent time points. At each time

point, samples were spun down and the supernatant was collected and frozen at -20°C until analysis via ELISA.

2.2.7 ELISA

ELISAs were carried out for IL-12 and IFN- γ . For IFN- γ , ELISA was performed according to the manufacturer's instructions. For IL-12, 100 μ L of 2 μ g/mL mouse IL-12 p70 antibody was added to 96 well Nunc MaxiSorp flat-bottom plates and incubated at 4°C overnight. After washing with wash buffer (PBS supplemented with 0.05% Tween 20) 4 times, wells were blocked with PBS supplemented with 1% BSA for 2 hours at room temperature. Wells were then washed 4 times and 100 μ L of sample was added to each well. After 2 hours incubation at room temperature, samples were washed with wash buffer 4 times, followed by incubation with 100 μ L of 0.2 μ g/mL biotinylated mouse IL-12 p70 antibody. After incubation at room temperature for 2 hours, samples were washed again with wash buffer 4 times. 100 μ L of streptavidin-HRP (1:200 v/v dilution) was added to each well and incubated at room temperature for 20 minutes. After 4 washes with wash buffer, samples were incubated with 100 μ L of substrate solution and incubated for 20 minutes in the dark. 50 μ L stop solution was added to stop the reaction, after which samples were read at 450 nm and 540 nm.

2.2.8 Bioactivity Assay for IL-12 Releasates

Splenocytes (5×10^5 cells/well) from naïve wild-type C57BL/6J mice were incubated with 10-fold dilutions (1000pg/ml to 0.1pg/ml) of either IL-12 releasate, IL-12 standard, or blank releasate in a 96-well round bottom plate in

200 μ L total volume of complete medium (RPMI supplemented with 10% FBS, 1X penicillin-streptomycin, 2 mM L-glutamine, and 50 μ M 2-mercaptoethanol). Cells were incubated for 72 hours at 37°C in a 5% CO₂ atmosphere. Culture supernatants were harvested and a mouse IFN- γ ELISA was performed according to the manufacturer's protocol to determine IL-12-induced IFN- γ production.

2.2.9 Animal Studies

6-8 week old female C57BL/6J mice (strain 000664) were purchased from Jackson Laboratory. After at least three days of acclimation, mice were shaved and inoculated with bilateral injections of 100,000-200,000 B16F10 cells per site. B16F10 cells were maintained and propagated in DMEM supplemented with 10% FBS and 1% penicillin-streptomycin. After 7-10 days post-inoculation, or when visible tumors reached a size of 25-50 mm², mice were randomized into groups, ear-punched, and subcutaneously injected with 50 μ L of the appropriate treatment. Treatment injections were only given to one primary site and include the following: IL-12-loaded complex coacervates (n=11), bolus IL-12 in saline (n=6), and blank complex coacervates (n=11). Tumor dimensions for both the primary and contralateral sites were measured every 2-3 days using a digital caliper. On days 5 and 12 post-treatment, mice were sacrificed to analyze tumor explants via immunofluorescence. Mice were euthanized when tumors reached a size larger than 400 mm². Other causes for euthanasia included ulceration and bleeding of the tumor, lethargy, and cachexia. Data was compiled from two independent experiments.

2.2.10 Immunofluorescent Sectioning and Imaging

Tumor explants were immediately fixed in 4% (w/v) PFA for 3 hours at 4 °C followed by an overnight incubation step in 30% (w/v) sucrose. Samples were then embedded in OCT (Tissue-Tek), frozen on dry ice, sectioned using a cryomicrotome at 10 µm thickness, and stored at -20°C until staining. Slides were air-dried at room temperature for 20 minutes and incubated in PBS to remove OCT. Samples requiring permeabilization were incubated with 0.2% Triton X-100 in PBS for 10 minutes at room temperature and subsequently washed in PBS. Samples were blocked with 10% goat serum and 0.1% Triton X-100 and incubated at room temperature for 1 hour, after which primary antibody diluted in staining buffer (2% goat serum and 0.1% Triton X-100) was added. After an overnight incubation step at 4°C, samples were washed in staining buffer, and incubated with secondary antibody diluted in staining buffer. Samples were incubated at room temperature in the dark for 1 hour and washed in staining buffer. DAPI counterstaining was performed, washed in PBS and deionized water, and mounted in Cytoseal 60. Immunofluorescence images were captured on an inverted microscope (Eclipse Ti, Nikon). Fluorescent images were quantified using ImageJ (NIH), in which the total fluorescent intensity was divided by the average intensity from 20 individual cells; at least 4 separate fields of view were analyzed during this step.

2.2.11 Statistical Analysis

All statistical analysis was performed using Prism Version 8.1.1 (Graphpad Software, San Diego, CA).

2.3 Results

2.3.1 Soluble Complex Coacervates Exhibit Coalescence

The complex coacervate platform used in this study takes advantage of the natural binding affinity of heparin for IL-12. IL-12-heparin complexes form further polymer- and protein-rich phases upon the addition of PEAD (**Figure 4A**). When initially clear solutions of heparin and PEAD are combined, a turbid solution forms instantaneously, indicating the formation of coacervates (**Figure 4B**). The complex coacervates are formulated in mass ratios of 5.5:1 = PEAD:heparin to yield the most number of isoelectrically charged droplets. To visualize the loading capacity of our heparin-based complex coacervate platform, BSA-647 (blue) is encapsulated as a model protein. After centrifugation to accelerate coacervate sedimentation, BSA-647 is visualized together with the coacervate pellet (**Figure 4B**), indicating its successful encapsulation. In the absence of centrifugation, coacervate droplets coalesce over time to form larger agglomerates (**Figure 4C**). Smaller coacervate droplets (yellow arrows) are observed surrounding larger droplets (yellow asterisks) as assessed by cryo-SEM.

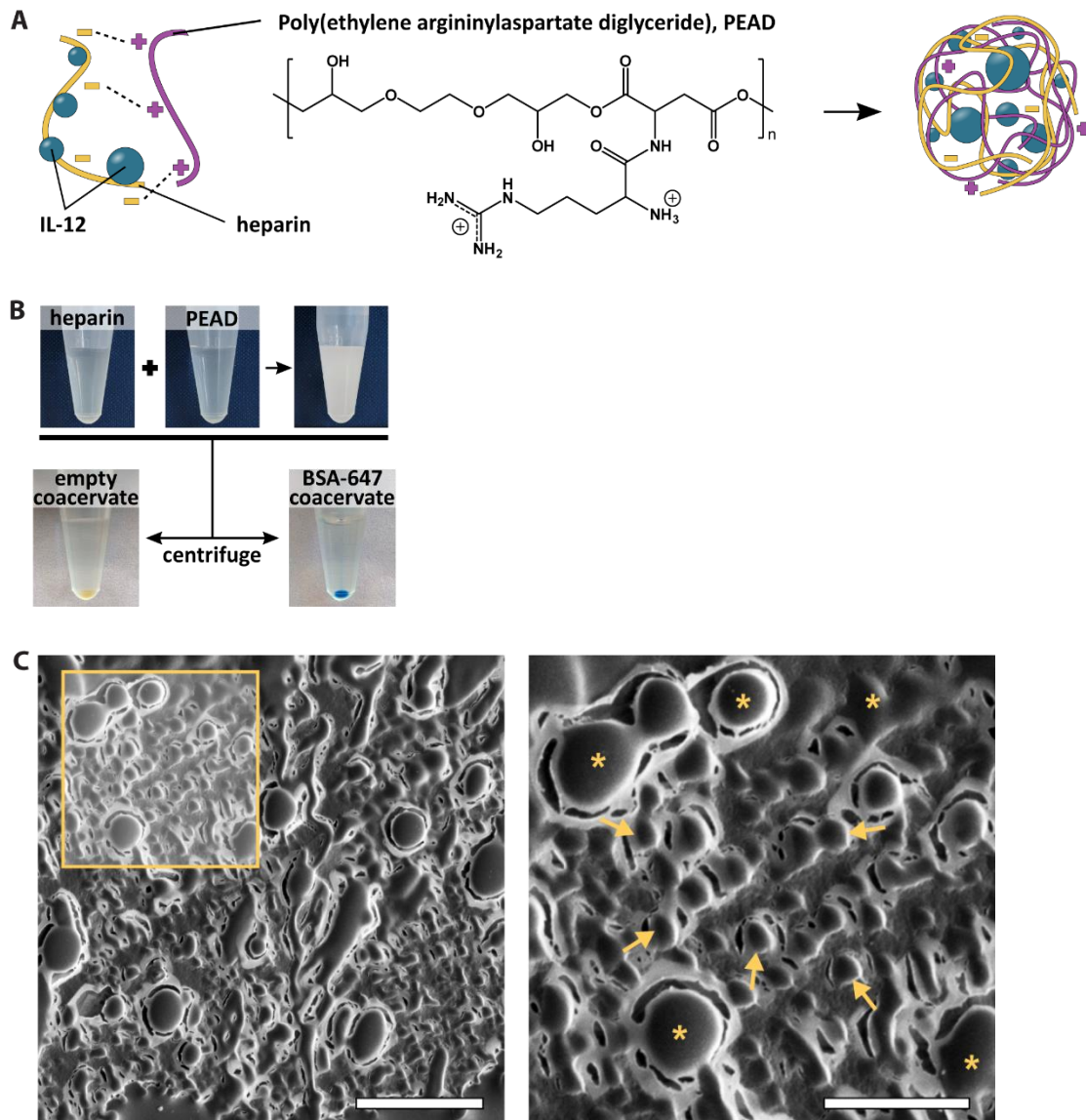


Figure 4. Heparin-based Complex Coacervate Behavior. **A.** Schematic detailing the complexation of IL-12 and heparin with PEAD. **B.** 10 mg/mL heparin and PEAD solutions in 0.9% saline instantaneously form a turbid solution upon mixing. BSA-647 (blue) is localized together with the empty coacervate. **C.** Cryo-SEM images show both small (yellow arrows) and large (yellow asterisk) complex coacervates (left scale bar: 10 μm ; right scale bar: 5 μm).

2.3.2 Complex Coacervates Protect and Enhance Bioactivity of IL-12

The tumor microenvironment presents a challenging environment for cytokines due to its hypoxic and acidic nature. The effect of IL-12 encapsulation was assessed on its bioactivity by incubating free IL-12 and IL-12 loaded into complex coacervates in the presence of trypsin, a broad-spectrum protease (**Figure 5A**). At set time points, coacervates were broken apart with a combination of 2X PBS and heparinase II; heparinase II degrades heparin in a time-dependent manner and shows complete degradation after 1 hour (**Figure 6**), allowing the complex coacervate to disassemble. At both 1 and 10 hours post-incubation at 37°C, a significantly improved protective effect was observed when IL-12 was encapsulated in coacervates. Specifically, $83.9 \pm 10.5\%$ and $46.0 \pm 5.2\%$ of initial IL-12 remained after 1 hour of incubation with trypsin. 10 hours later, only $2.1 \pm 0.6\%$ of the IL-12 was left when unprotected compared to $70.1 \pm 18.7\%$ when encapsulated. The release behavior of IL-12 from the complex coacervates was then assessed for two different formulations (**Figure 5B**). The first (black squares) included both BSA and IL-12 during the coacervate complexation step while the second (white squares) did not include BSA. Both formulations showed a near complete encapsulation efficiency of $>99.99\%$ as assessed by ELISA. A near 100% cumulative release was observed over 14 days when IL-12 is co-encapsulated with BSA, presumably due to the increased competition for heparin by both BSA [71] and IL-12. On the other hand, when only IL-12 is encapsulated, it is released in a slower fashion. Given the general quicker degradation rates *in-vivo*, we opted to go with the second formulation without BSA for all subsequent experiments. Finally, the

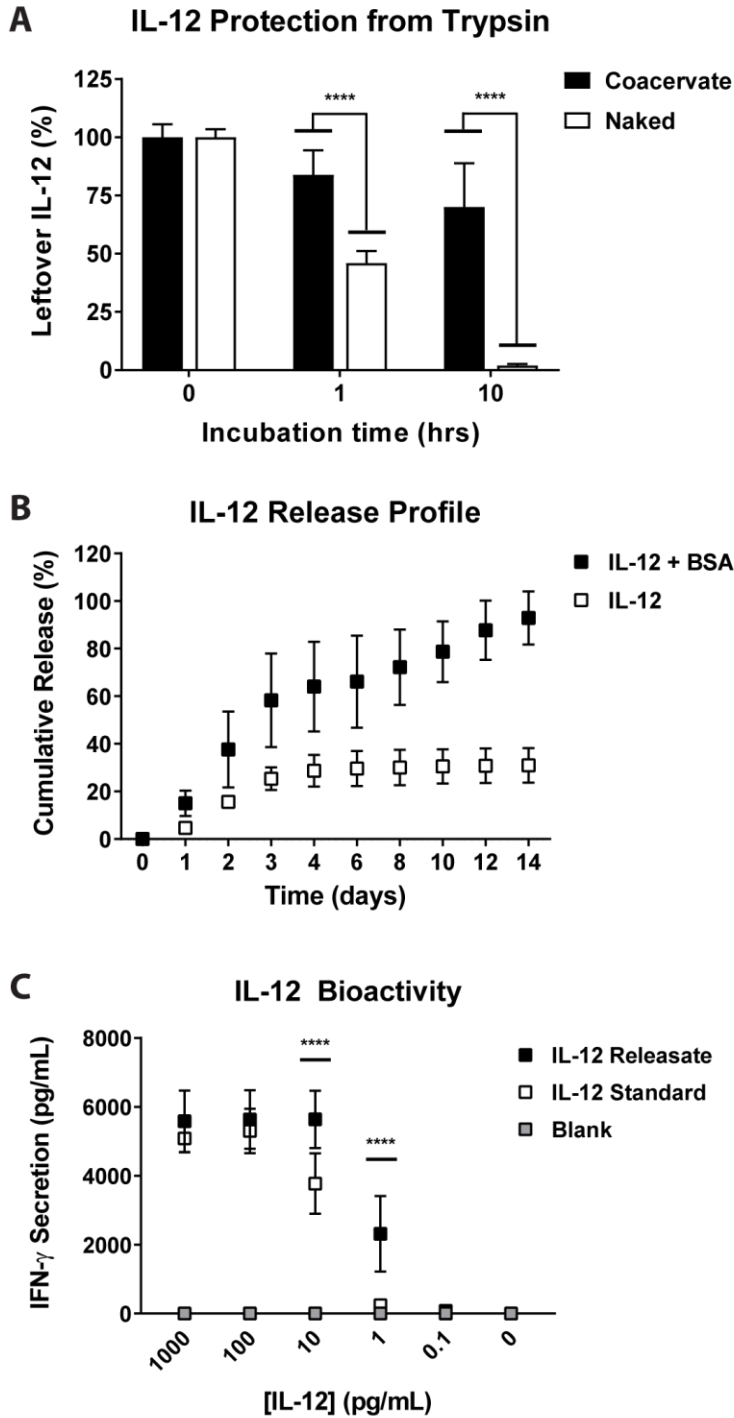


Figure 5. Coacervate Protects and Enhances IL-12 Bioactivity. **A.** 100ng of unprotected or encapsulated IL-12 was incubated with 50ng of trypsin at 37°C. IL-12 was quantified using ELISA (n=4, ****p<0.0001). **B.** IL-12 was encapsulated in the presence or absence of BSA and assessed for its release in 0.9% saline containing 0.1% BSA (n=3). **C.** C57BL/6J mouse splenocytes

were cultured with known concentrations of IL-12 releasate (day 2 samples) or stock IL-12. 72 hours later, supernatants were assessed for IFN- γ secretion using ELISA (n=3, ****p<0.0001).

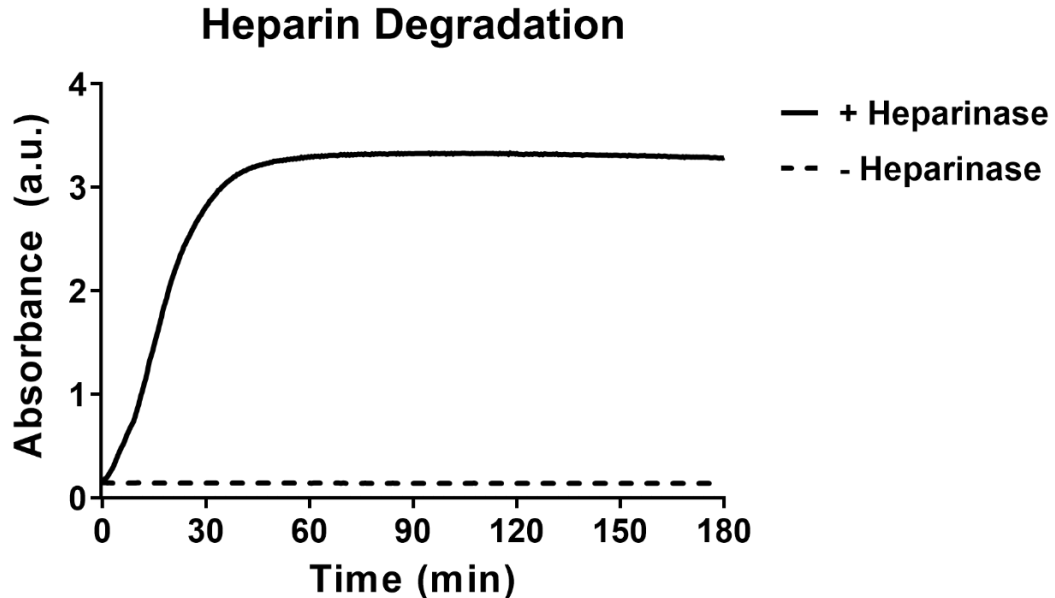


Figure 6. Heparinase II-mediated Degradation of Heparin. 33.3 μ L of 10 mg/mL heparin was incubated with 4 units of heparinase II for 3 hours at 37°C.

the bioactivity of the IL-12 released from the complex coacervates was examined using a splenocyte assay (**Figure 5C**). A range of IL-12 concentrations were prepared from IL-12 releasate (black squares) or stock IL-12 (white squares) and incubated with C57BL/6J splenocytes and assessed for their ability to induce IFN- γ secretion. A dose-responsive effect was observed for both experimental groups, in which lower [IL-12] yielded less IFN- γ secretion. In particular, the bioactivity of IL-12 releasate was 65.6% and 762.7% higher than that of stock IL-12 at 10 pg/mL and 1 pg/mL, respectively. This increase in

bioactivity indicates that IL-12 is most likely released as a complex with heparin as heparin-bound IL-12 has been shown to increase IL-12 bioactivity [69].

2.3.3 Single Injection of IL-12 Coacervate Inhibits Systemic Tumor Growth

The utility of the IL-12 complex coacervates was determined in a pre-clinical mouse melanoma model using syngeneic B16F10 melanoma cells. Age-matched C57BL/6J mice were inoculated with bilateral subcutaneous injections at each site, with treatment beginning approximately 7-10 days post-inoculation. To determine the appropriate dose, a dose escalation study was carried out using 1, 10, or 30 μg of IL-12 per complex coacervate treatment injection; injections were only given to one side. Individual tumor growth curves for the primary site indicate that higher amounts of IL-12 did not induce any systemic toxicities and resulted in progressively improved inhibition of tumor growth (**Figure 7A**); variation in tumor size among mice decreased with increasing IL-12 dose. Mice receiving the lowest dose of 1 μg exhibit lower survival rates as mice had to be euthanized due to tumor size. Mice treated with blank coacervates (white circles) show typical growth kinetics of B16-10 cells in a mouse. There does not seem to be a significant difference in the average growth of tumor (**Figure 7B**) for the different doses. Interestingly, a similar trend was observed in the untreated contralateral site, suggesting systemic immunity (**Figure 8**). In terms of survival, there is no significant difference across the different groups (**Figure 7C**). It should be noted, however, that a log-rank test for trend indicates a significant trend in the doses (** $p=0.003$). Given these results, we opted to use 10 μg per complex coacervate injection.

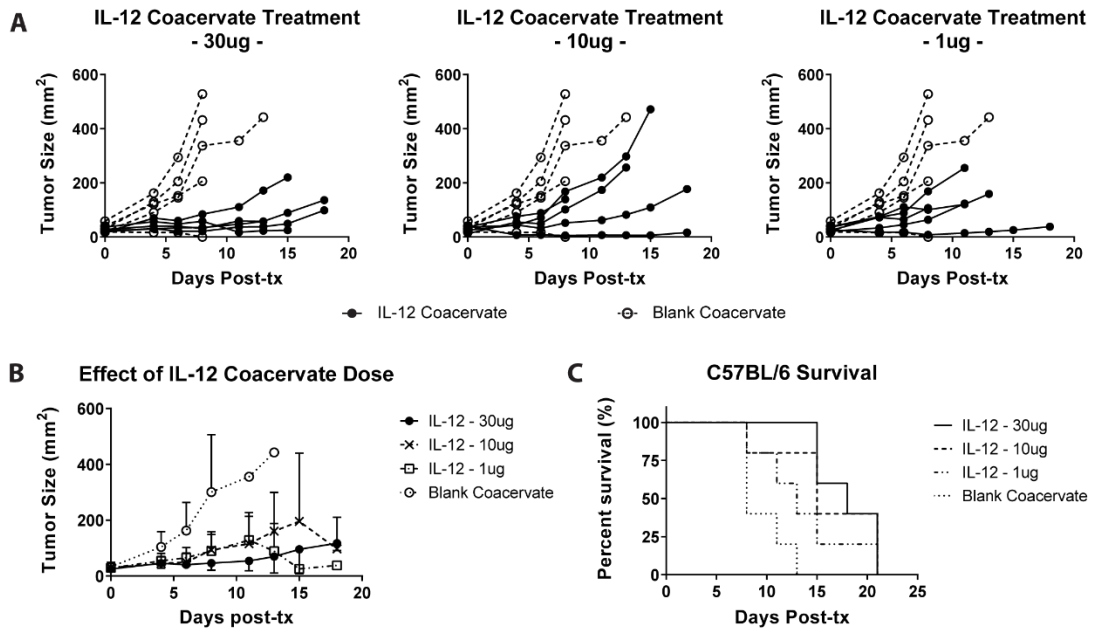


Figure 7. Dose Escalation Study of IL-12 Coacervates. **A.** 6-8 week old female C57BL/6J mice were inoculated with 100,000-200,000 B16F10 cells and subcutaneously treated with IL-12 coacervates with varying doses of IL-12. Tumor sizes were tracked until euthanasia or death. **B.** Average size of primary tumor is tracked over time and show no significant difference among IL-12-receiving groups. **C.** Kaplan-Meier survival curves of mice indicate a significance in trend as assessed by logrank test for trend (n=5, **p<0.003).

We then assessed the effect of administration by delivering IL-12 in bolus form or encapsulated in our complex coacervate platform. Average tumor growth curves at the primary site show a significant inhibition of growth when mice are treated with IL-12 coacervate as opposed to bolus forms of IL-12 (**Figure 9A**). Not surprisingly, bolus forms of IL-12 showed efficacy over blank complex coacervate treatment. Interestingly, this trend in significance was replicated at the contralateral site (**Figure 9B**), which likely suggests the presence of a systemic immune response. Individual growth plots of mice

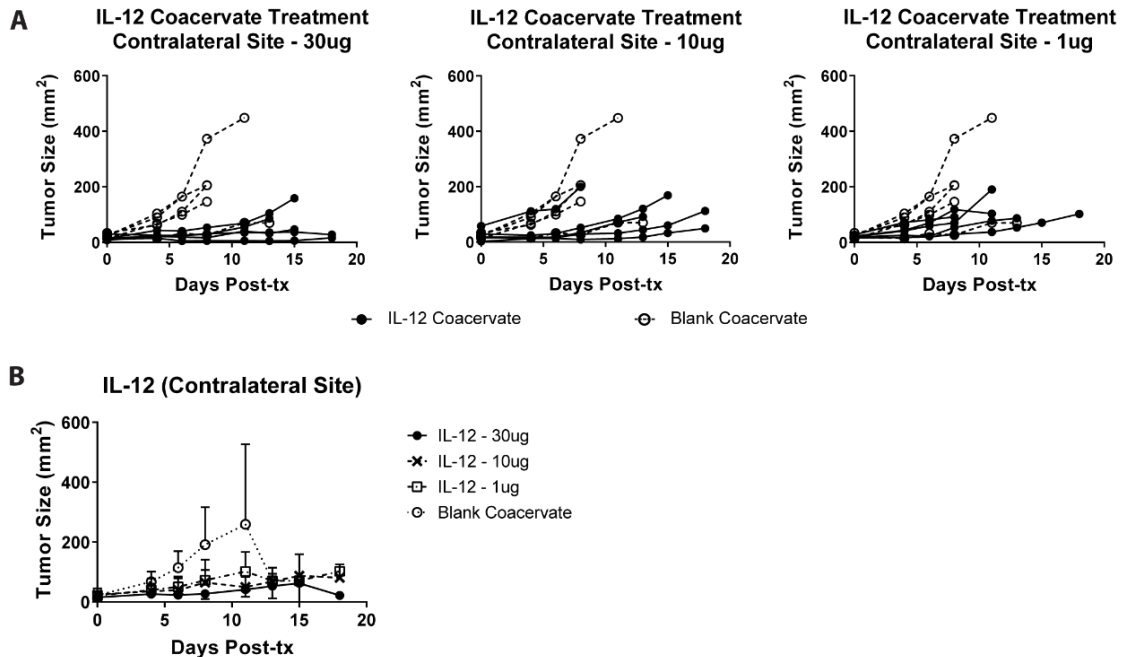


Figure 8. Contralateral Tumor Growth for Dose Escalation Study. **A.** The growth of the untreated contralateral tumor was tracked over time for mice receiving complex coacervates with varying doses of IL-12. **B.** Average size of contralateral tumor is tracked over time and show no significant difference among IL-12-receiving groups (n=5).

further corroborate the significance observed among different groups (**Figure 10**).

2.3.4 Significant Lymphocyte Accumulation Observed in Tumor Environment

To better understand the mechanism of inhibition of tumor growth, we probed the tumor microenvironment for immune cells at different time points. The early immune response was assessed by examining NKp46+ cell infiltration into the tumor at a relatively early timepoint of 5 days post-treatment (**Figure 11A**). Mice receiving the IL-12 coacervate treatments showed a significant increase in NK cell infiltration (yellow) compared to those receiving bolus forms

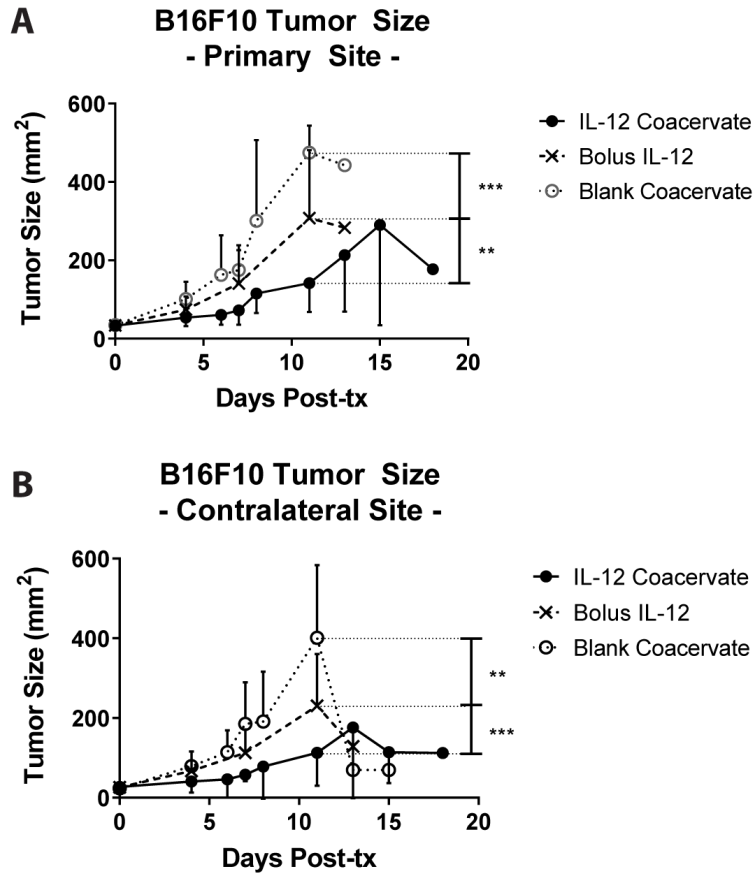


Figure 9. IL-12 Delivery Significantly Inhibits Systemic Tumor Growth. **A.** Mice were given a single injection of 10 μ g IL-12 in bolus form or encapsulated in complex coacervates. Tumor size was tracked over time. **B.** Average tumor growth curves were assessed for the untreated contralateral site as well (n=11 for IL-12 coacervate group, n=6 for bolus IL-12 group, n=11 for blank coacervate group, **p<0.01, ***p<0.001 as assessed using the Holm-Sidak method).

of IL-12 or blank coacervate. Quantification of the immunofluorescence images further corroborates this trend (**Figure 11C**). Given the role of IL-12 in enhancing T cell survival and proliferation [72], we then assessed the tumor microenvironment for the presence of CD8 α + T cells, which mediate antigen-specific killing of the target cell. 12 days post-treatment, we observed a massive

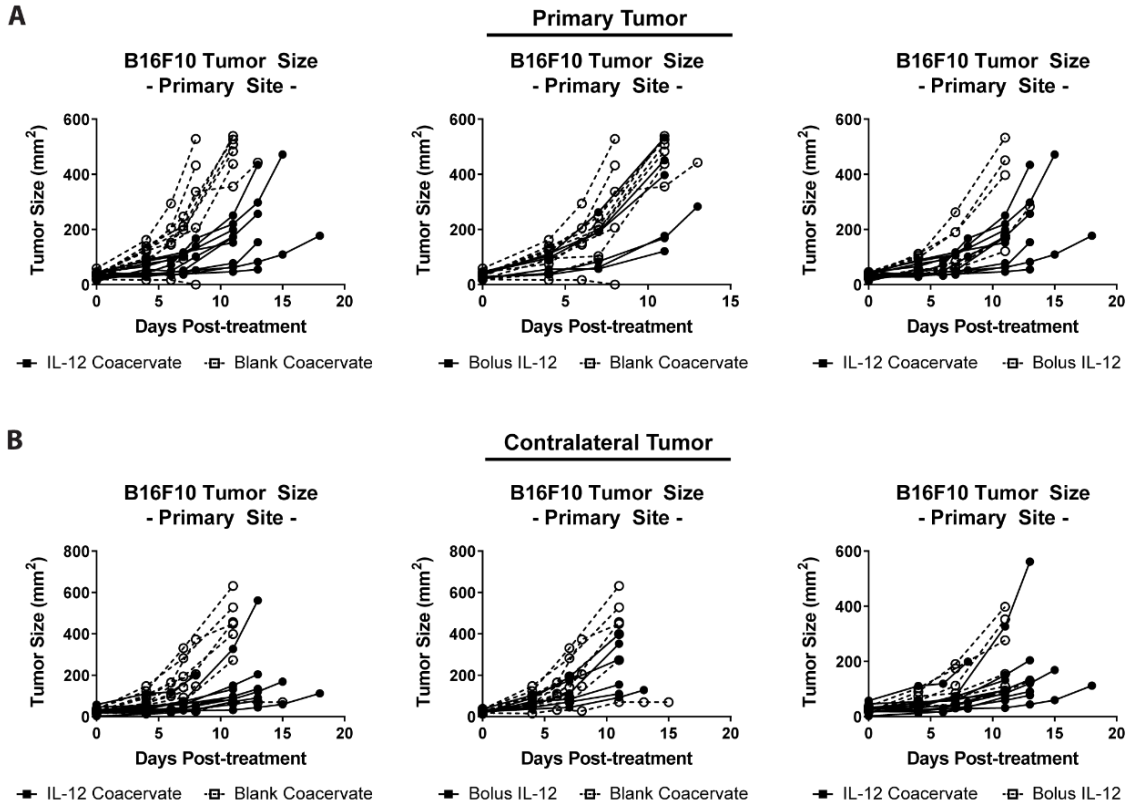


Figure 10. Tumor Growth Curves for Individual Mice. The growth of tumor was tracked over time for both the **A.** primary and **B.** contralateral sites.

intratumoral CD8 α ⁺ T cell presence in mice receiving IL-12 coacervate in contrast to those receiving bolus IL-12 or blank coacervates (**Figure 11B** top row and **11D**). Given that IL-12 has also been shown to mediate the reversal of Treg immunosuppression by decreasing Treg frequency [63], we then probed the tumor environment for CD4⁺ FoxP3⁺ Treg cells (**Figure 11B** bottom row and **Figure 12**). We were unable to observe any Treg cells in the mice receiving IL-12 coacervate. On the other hand, a relatively large number of Treg presence was detected in mice receiving the blank coacervate. Collectively, the intratumoral increase in CD8 α T cells and decrease in Treg cells in mice

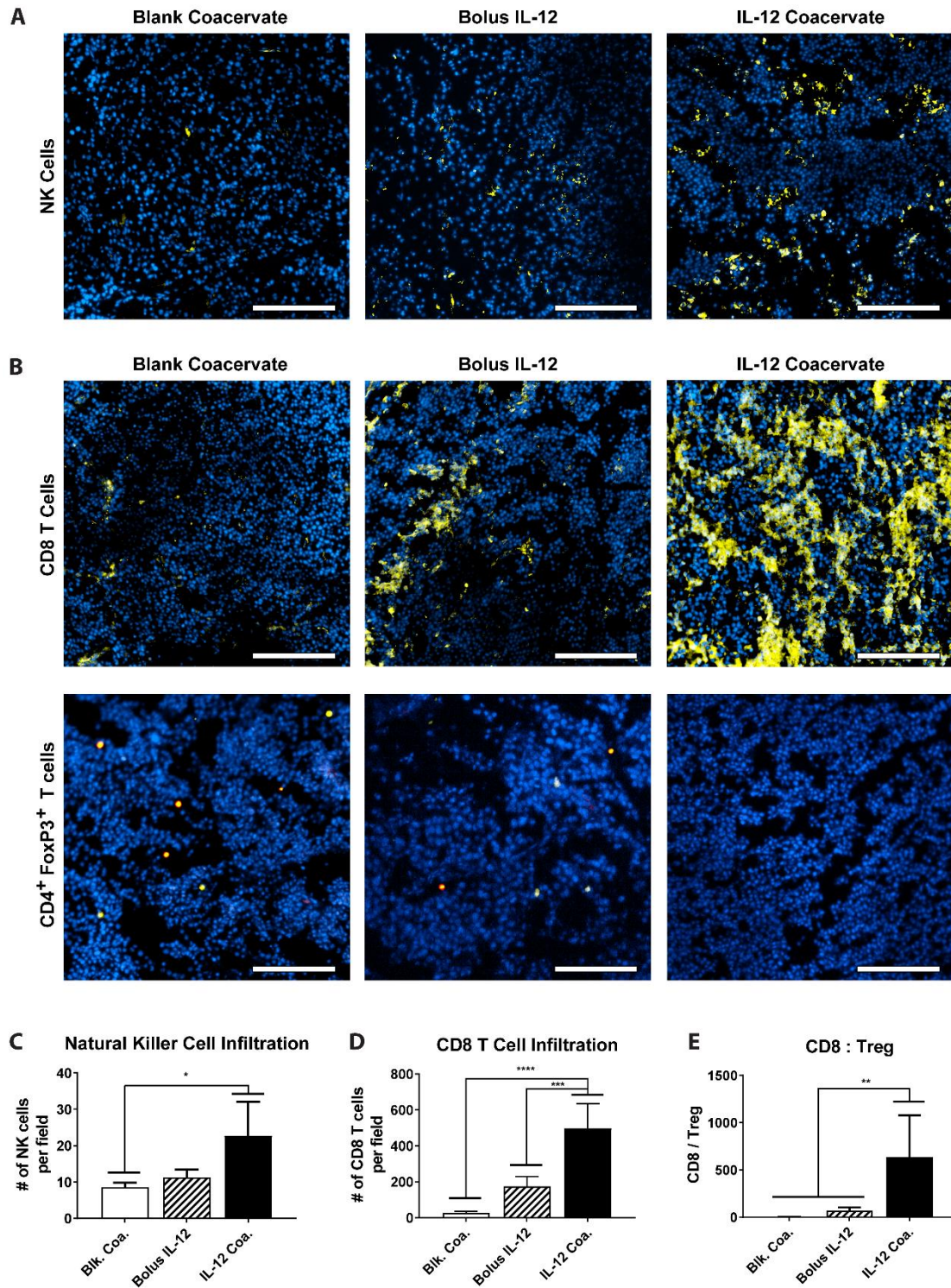


Figure 11. IL-12 Coacervates Improve Intratumoral Innate and Adaptive Immune Response. **A.** Mice receiving various treatments were euthanized 5 days post-treatment and assessed for the presence of NKp46+ cells in the

tumor (blue: nucleus, yellow: NKp46, scale bar: 200 μ m). **B.** Intratumoral presence of CD8 α + cells (top) and CD4+FoxP3+ cells (bottom) were assessed 12 days post-treatment (blue: nucleus, yellow: CD8 α , red: CD4, teal: FoxP3, scale bar: 200 μ m). The fluorescence signal is quantified from at least five different fields to represent average number of **C.** NKp46+ cells and **D.** CD8 α + cells (* p <0.05, *** p <0.001, **** p <0.0001). **E.** CD8 α :CD4+FoxP3+ is quantified for the different treatment groups (** p <0.01).

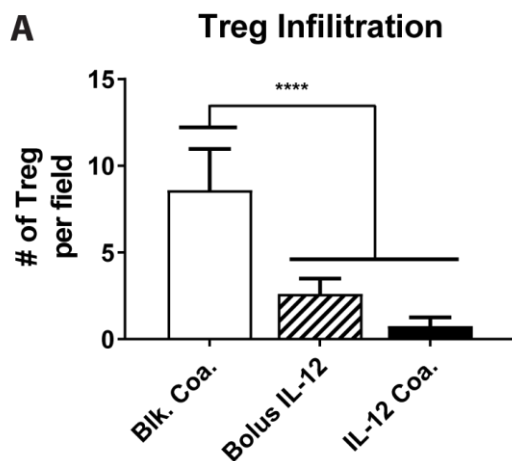


Figure 12. Quantification of Intratumoral CD4+FoxP3+ Treg Cells. Quantified values of CD8 α + are divided by the number of CD4+FoxP3+ Treg cells (**** p <0.0001).

receiving the IL-12 coacervate results in an increase in the CD8:Treg ratio and plays a role in inhibiting tumor growth.

2.3.5 IL-12 Coacervate Treatment Increases Tumor PD-L1 Expression

Finally, we examined the intratumoral expression of PD-L1, a ligand for PD-1 that is normally increased in the presence of IFN- γ . Mice receiving the IL-12 complex coacervates show a large and significant increase in PD-L1 expression (**Figure 13A**), thereby providing indirect evidence that IL-12

complex coacervates activate NK and/or CD8 T cells to secrete IFN- γ . Quantification of PD-L1 expression indicates a nearly 30-fold increase in PD-L1+ expression in mice treated with IL-12 coacervate over those treated with bolus IL-12 (**Figure 13B**). Given the immune-suppressive role of lymphocyte PD-1 binding to PD-L1 on tumor cells, the large increase in PD-L1 expression in mice receiving the

IL-12 coacervate effectively neutralizes the large increase in NKp46+ and CD8 α + cells observed. Therefore, despite the significant differences observed in tumor size, we were unable to see significant differences in survival. It should be noted that there was a significant survival effect in mice receiving IL-12 coacervate compared to those receiving blank coacervate ($p=0.0037$, log-rank test) while the difference between mice receiving bolus IL-12 and blank coacervate trended towards significance ($p=0.1358$, log-rank test) but was not statistically significant; there was also no significant difference in survival for mice receiving IL-12 coacervate and bolus IL-12 ($p=0.2392$, log-rank test).

2.4 Discussion

Skin cancer constitutes nearly 80% of all cancer diagnoses; approximately 5.5 million out of 7.1 million cancers diagnosed in 2017 were found to be of the skin [3]. While the bulk of these skin cancers include relatively benign carcinomas such as those of basal cells and squamous cells and are generally easily cured, melanoma, is a highly aggressive cancer. Unfortunately, cases of melanoma are widespread when compared to all other cancers. In particular, among males and females between 30-49 years old, melanoma ranks as the first and second-

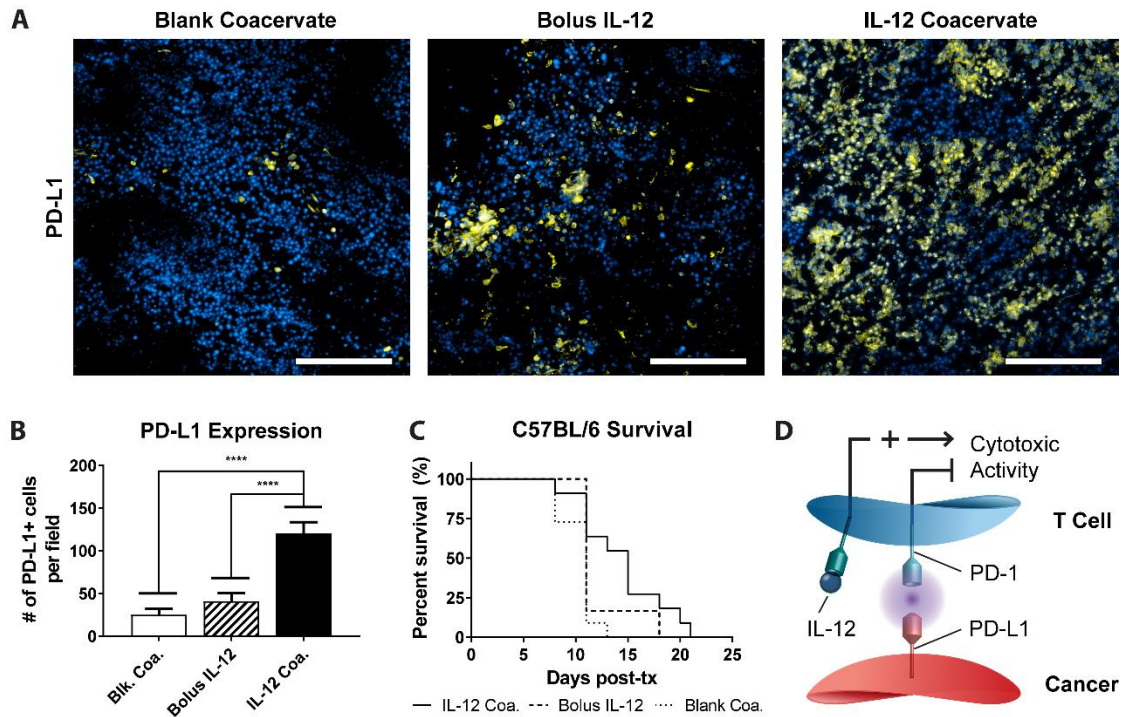


Figure 13. IL-12 Coacervates Increase Tumor PD-L1 Expression. **A.** Intratumoral expression of PD-L1+ cells was analyzed via immunofluorescence 12 days post-treatment (blue: nucleus, yellow: PD-L1, scale bar: 200 μ m). **B.** PD-L1+ fluorescence signal is quantified to represent the average number of PD-L1+ cells (**** $p < 0.0001$). **C.** Kaplan-Meier survival curves of mice indicate a non-significant difference in mice receiving IL-12 coacervate and bolus IL-12. A significant effect was observed between mice receiving IL-12 and blank coacervate ($n=11$ for IL-12 coacervate group, $n=6$ for bolus IL-12 group, $n=11$ for blank coacervate group). **D.** Schematic illustrating the need to inhibit the PD-1/PD-L1 checkpoint for effective IL-12-mediated treatment of melanoma.

-most prevalent cancer, respectively, thereby underscoring its pervasiveness in society [4].

IL-2 represents one of the earliest forms of immunotherapy to treat melanoma and cancer in general. Unfortunately, its high toxicity and relatively

low clinical response (e.g. 19.7%) tempered the enthusiasm behind its FDA approval in 1998 [12, 13]. Other cytokines including IL-12 showed promising results in pre-clinical studies. However, early clinical trials using systemically-delivered recombinant IL-12 were halted due to severe hematologic and organ toxicity in most of the enrolled patients and two deaths [64]. Subsequent studies determined that an initial priming dose of IL-12 before subsequent daily injections were necessary to mitigate a severe IFN- γ -mediated systemic response [65]. Unfortunately, while the initial priming of IL-12 has shown to prevent systemic toxicity, it also attenuates the IFN- γ response, effectively reducing the full immune response at the desired tumor site. Due to such toxicities, the use of recombinant cytokines as an immunotherapeutic treatment method for cancer diminished in favor of vaccine and gene therapy. While significant advances have been made in this area, subpar transfection efficiencies and the potential for undesired off-target genetic changes have limited applications. Furthermore, the advent of checkpoint inhibitors has led to an explosion of related studies. Unfortunately, checkpoint inhibitors are not without their issues as well, some of which include systemic toxicities and the limited type of patients it benefits. More notably, the use of checkpoint inhibitors requires priming of the tumor environment to include a large number of lymphocytes such as T cells [57-60].

From this perspective, the need for immunotherapeutic proteins that induce proliferation of effector cells is urgent and could lead to improved responses for a broader range of patients. Our study examines a previously

unexplored avenue of using complex coacervation to more effectively and safely deliver such a protein as we carefully propose a return to the use of recombinant proteins. Notable roles for IL-12 include, but are not limited to the following: 1) activation of NK cell activity, in which NK cells activated by IL-12 display an enhanced level of cytolytic activity against target cells [73, 74], 2) enhanced activation of CD8+ T cells [75], 3) DC-mediated increase in T helper 1 (Th1) responses [76], 4) upregulation of MHC I antigen presentation on tumor cells [77], and 5) anti-angiogenesis mediated by induced secretion of anti-angiogenic factors such as inducible protein-10 (CXCL10) [78].

Our heparin-based complex coacervation platform represents a departure from standard forms of controlled delivery, in which the following advantages are proposed over alternative modes of controlled delivery: 1) the low interfacial energy between the coacervate and non-coacervate phase[67] results in an emulsion (**Figure 4B and 4C**) unlikely to be taken up by cells, 2) the utilization of anionic heparin acts to stabilize and enhance the bioactivity of therapeutic proteins (**Figure 5C** [79]), 3) the affinity between heparin and proteins drives high encapsulation efficiencies (>99.99% for IL-12 in our system), and 4) the degradation of cationic poly(ethylene argininyaspartate diglyceride) does not generate a tumor-favorable acidic environment. Surprisingly, the use of complex coacervation has not yet been examined for its utility in delivering therapeutic proteins for anti-cancer applications.

Given the dynamic nature of complex coacervation, it is important to consider the potential of other proteins competing with IL-12 for heparin binding

spots, in which it is possible that pro-cancer proteins (*i.e.* FGF-2, VEGF) replace IL-12 within the coacervate platform. Our data indicates that encapsulation of IL-12 without BSA prevents its quick release unlike that co-encapsulated with BSA (**Figure 5B**). Given that both formulations were released in sink conditions of saline containing excess BSA, the lack of a quick release in the formulation without BSA suggests that IL-12 is not easily replaced. It should be noted, however, that other proteins with higher binding affinities exist and their effect on our platform have not been examined.

On a final note, NKp46+ cell infiltrate in the bolus group was surprisingly low (**Figure 11A**). It is possible that 5 days post-treatment may have been too late of a window to examine NK cell infiltration. Another likely explanation is that the enhanced bioactivity of IL-12-heparin complexes and prolonged delivery simply results in higher NK cell activation and proliferation. Also, NKp46 has been shown to be expressed on a small subset of NKT cells [80]; some of the NKp46+ cells in tumors of mice treated with IL-12 coacervate could be NKT cells. Along these lines, CD8 α is also expressed on DC subsets that play a role in cross-presentation [81, 82] and some of the CD8 α + cells we observed could activate T cells within the tumor microenvironment. Importantly, given the role of IL-12 towards CD8+ T cell proliferation and in enhancing T cell survival and proliferation, the large intratumoral presence of CD8 α T cells in mice treated with IL-12 coacervate (**Figure 11B**) indicates a prolonged delivery of bioactive IL-12. Questions of whether or not these CD8 α + infiltrates represent clonal expansion of antigen-specific T cells and whether or not these cells underwent

proliferation in the lymph node vs the tumor were not examined as the main goal of this study was to demonstrate a proof-of-concept for complex coacervate-mediated delivery of immunotherapeutic proteins. However, given the large increase in PD-L1 expression on tumor cells (**Figure 13A**), which is upregulated in the presence of IFN- γ , we expect the expansion of antigen-specific CD8 T cells to a certain extent. Finally, IL-12 has been shown to decrease Treg frequency and Foxp3 levels in Tregs [63], which could explain the decrease in CD4+FoxP3+ Tregs we observed in mice treated with IL-12 coacervate.

2.5 Conclusions

In this study, we demonstrate the use of a heparin-based complex coacervation platform to deliver IL-12 in a pre-clinical murine melanoma model. This study is the first to examine the utility of recombinant protein delivery via complex coacervates for anti-cancer applications. Our data herein demonstrates the protection of IL-12 within a potentially harsh tumor environment and an increase in the bioactivity of the released IL-12. We show that mice treated with IL-12 coacervates exhibit a significant inhibition of tumor growth compared to bolus forms of delivery, in which a systemic response was observed as assessed by a concurrent inhibition of tumor growth in untreated contralateral sites. Finally, we show that varying levels of intratumoral NKp46+, CD8 α +, and CD4+FoxP3+ cells collectively play a role in this inhibition. Future studies combining recombinant proteins such as IL-12 with checkpoint inhibitors could offer improved patient responses, in which complex coacervates would provide a novel means to the localized delivery of immunotherapeutic proteins.

Chapter 3.

A Biocompatible Betaine-functionalized Polycation for Coacervation

Note: This work was previously published as: Hwang M.P., Ding X., Gao J., Acharya A.P., Little S.R., and Wang Y. A Biocompatible Betaine-functionalized Polycation for Coacervation. Soft Matter 14:387-395 (2018). It is reproduced here with permission of the publisher.

The aqueous nature of complex coacervates provides a biologically-relevant context for various therapeutic applications. In this sense, biological applications demand a corresponding level of biocompatibility from the polyelectrolytes that participate in complex coacervation. Continued development with naturally-occurring polyelectrolytes such as heparin and chitosan underscore such aims. Herein, we design a synthetic polycation, in which betaine is conjugated to a biodegradable polyester backbone. Betaine is a naturally-occurring methylated amino acid that is ubiquitously present in human plasma. Inspired by its vast range of benefits – including but not limited to anti-inflammation, anti-cancer, anti-bacterial, anti-oxidant, protein stabilization, and cardiovascular health – we aim to impart additional functionality to a polycation for eventual use in a complex coacervate with heparin. We report on its *in-vitro* and *in-vivo* biocompatibility, *in-vitro* and *in-vivo* effect on angiogenesis, *in-vitro* effect on microbial growth, and ability to form complex coacervates with heparin.

3.1 Introduction

The self-assembly of materials can be characterized as a progression towards a global energy minimum. A central class of materials that undergo such transformations are complex coacervates. Driven by short-range [66] or long-range electrostatic interactions [67], complex coacervation is an associative phase separation phenomenon characterized by the aggregation of at least two polyelectrolytes into interpolymer complexes. Specifically, the release of counterions during the complexation of polyelectrolytes leads to a net gain in entropy [83, 84], resulting in a dynamic equilibrium of a polyelectrolyte-rich coacervate and polyelectrolyte-poor supernatant phase. The relative simplicity of combining polyelectrolytes has given rise to a broad range of materials for complex coacervation, with applications that range from protocells [85, 86] to microencapsulates of food or cosmetics [87].

In particular, the substantial water content of complex coacervates [88] has been capitalized on to facilitate the encapsulation of proteins [45, 89, 90], small molecules [91-93], and cells [94] for various biological applications. These biological confines consequently limit the range of tenable polyelectrolytes to those of biocompatible nature. Not surprisingly then, a large number of complex coacervates take inspiration from naturally-occurring polyanions such as heparin [46, 48] or hyaluronic acid [95, 96]. For example, heparin has been shown to bridge cationic sequences on proteins with their respective receptors [97-99], rendering effective receptor-ligand interactions. The use of cationic polyelectrolytes for complex coacervation, however, requires more attention.

While biological polysaccharides such as chitosan are regularly used [95, 100, 101], synthetic cationic polymers are equally employed [45, 48, 102-105], often for the capacity to formulate application-specific designs. Unfortunately, the scope of polycations for biological applications can be limited by their general toxicity to cells, necessitating biocompatible cationic polymers.

We have previously reported on an arginine-based polycation[70], poly(ethylene argininy laspartate diglyceride) (PEAD), which forms a biocompatible delivery vehicle upon complex coacervation with heparin. A number of derivative studies using PEAD have demonstrated an enhanced bioactivity of the encapsulated protein [45-48]. Here, we aim to confer functionality to the cationic polymer itself through deliberate design, by replacing the arginine side group on poly(ethylene aspartate diglyceride) (PED) with betaine. Betaine is ubiquitously present in human plasma, primarily due to dietary intake as well as some endogenous level of synthesis in the liver and kidney [50]. Primarily understood as an osmolyte to protect cells from environmental stress [106], betaine has numerous other chemical and physiological benefits, including but limited to: protein stabilization [107], methyl donation to maintain liver and heart health [108], supplement for the prevention of cancer [52], reduction in angiogenesis and inflammation [109], and anti-bacterial activity [110]. Given its numerous roles, we were motivated to assess its potential when grafted onto PED.

Herein, we report on a new polycation, poly(ethylene betainylaspartate diglyceride), or betaine-functionalized poly(ethylene aspartate diglyceride) (B-

PED). The quaternary ammonium group on betaine imparts a positive charge to the polymer. We assess the *in-vitro* and *in-vivo* biocompatibility of the B-PED and explore its effect on angiogenesis and microbial activity. Finally, we examine its interaction with heparin and demonstrate its potential use as a polycation for complex coacervation.

3.2 Materials and Methods

3.2.1 Materials

Betaine and deuterium oxide (Sigma-Aldrich, St. Louis, MO), ethylene glycol diglycidyl ether (EGDE) (Pfaltz & Bauer, Waterbury, CT), N-Boc-L-aspartic acid (Boc-Asp-OH) (Bachem, Torrance, CA), 4-(dimethylamino)pyridine (DMAP, $\geq 99\%$) (Alfa Aesar, Ward Hill, MA), anhydrous dimethylformamide (DMF), *N*-hydroxysuccinimide (NHS), *N,N*-dicyclohexylcarbodiimide (DCC), and tetra-*n*-butylammonium bromide (TBAB, 98%) (Acros Organics, Geel, Belgium), heparin sodium USP (Scientific Protein Labs, Waunakee, WI), fluorescein-conjugated heparin, timentin, DMEM, and Quant-iT PicoGreen dsDNA kit (Thermo Fisher Scientific, Waltham, MA), Cultrex basement membrane extract (R&D Systems, Minneapolis, MN), Matrigel high concentration (Corning, Corning, NY), endothelial cell growth medium and BulletKit (Lonza, Basel, Switzerland), dialysis tubing (Spectrum Labs, Rancho Dominguez, CA), CellTiter-Blue cell viability kit (Promega, Madison WI), RFP-expressing human umbilical vein endothelial cells (gift from Dr. Steven R. Little), mouse anti-rat CD68 antibody (Millipore, Billerica, MA), rabbit anti-rat α -SMA antibody and

mouse anti-rat CD31 antibody (Abcam, Cambridge, United Kingdom) were all used as received.

3.2.2 B-PED Synthesis

B-PED is synthesized according to conditions modified from those previously described [70]. Briefly, EGDE (1000 mg), Boc-Asp-OH (1338.8 mg), and TBAB (5 mg) were dissolved in 0.6 mL of DMF. The mixture was reacted at 120°C under N₂ for 20 minutes in a microwave reactor (Biotage, Uppsala, Sweden). The resulting intermediate polymer, poly(ethylene boc-aspartate diglyceride) (PED-boc) was solubilized in 2 mL DCM and precipitated into diethyl ether. Boc was removed via addition of 4:1 DCM:TFA ([TFA] = 2.5 mM). After 2 hours of stirring at room temperature, solvent was subsequently removed via a rotatory evaporator for 2 hours. Multiple precipitation steps in diethyl ether were used to remove excess reagents, DMF, and TFA. PED was then washed overnight in diethyl ether and dried under vacuum until further use. B-PED was prepared by combining PED (0.108 M of reactive sites), betaine (0.217 M), NHS (0.217 M), DCC (0.260 M), and DMAP (0.011 M) into DMF. The solution was stirred at 30 °C under N₂ for 48 hours. An insoluble dicyclohexylurea by-product was removed via centrifugation and filtration (0.22 µm). B-PED was then purified via multiple precipitation steps in diethyl ether, washed in ethanol, and dialyzed against deionized water for 18 hours.

3.2.3 Characterization of B-PED

¹H nuclear magnetic resonance spectroscopy (H-NMR) was performed on PED, B-PED, and betaine using deuterium oxide (D₂O) as a solvent (Biospin Avance

NMR, Bruker, Billerica, MA). Gel permeation chromatography (GPC) was used to assess the molecular weight of PED using DMF as the mobile and stationary phase (Viscotek VE2001); results were compared to polyethylene glycol calibration standards. Functional group assessment was carried out via Fourier transform infrared spectroscopy (FTIR) (Nicolet IR-100, Thermo, Waltham, MA).

3.2.4 Assessment of Cytotoxicity

In-vitro experiments were performed on NIH-3T3 cells (ATCC CRL-1658), and HUVECs (ATCC CRL-1730). NIH-3T3 cells and HUVECs were maintained in DMEM and endothelial basal media (EBM), respectively, and passaged using trypsin/EDTA upon confluence. Passage 4-6 cells were used for all experiments. For metabolic and proliferation assays, 7500 cells were seeded per 96 well and allowed to adhere overnight. Cells were then treated with varying concentrations of B-PED in the appropriate media (n=3). After 24 hours, cells were gently washed with DPBS three times and examined using CellTiter-Blue and PicoGreen kits, according to the manufacturer's instructions. CellTiter-Blue and PicoGreen readouts were read on a microplate reader (SynergyMX, Biotek, Winooski, VT). *In-vivo* cytotoxicity experiments were carried out on Sprague-Dawley rats. 100 μ L of saline or 10 mg/mL of B-PED in saline was subcutaneously injected into the dorsal area and explanted 1 week later (n=3). Tissues were fixed in 4% (w/v) PFA for 1 hour, followed by an overnight incubation step in 30% (w/v) sucrose. Samples were then embedded in OCT (Tissue-Tek), frozen on dry ice, and stored at -80 °C. OCT-embedded samples were sectioned at 10 μ m thickness and stained via H&E staining and

immunofluorescence (IF) staining. IF staining against CD68 was performed by cell permeabilization (0.2% triton-X 100), blocking with 5% (v/v) goat serum, incubation with mouse anti-rat CD68 antibody, and subsequent incubation with goat anti-mouse secondary antibody. H&E and IF images were captured on an inverted microscope (Eclipse Ti, Nikon).

3.2.5 Angiogenesis Assays

RFP-expressing HUVECs (Angio-Proteomie) were used for *in-vitro* angiogenic characterization. Briefly, basement membrane extract (reduced growth factor, Cultrex) was diluted to 10 mg/mL in sterile DPBS. 70 μ L of the diluted basement membrane extract was added to each 96 well and allowed to gel at 37 °C for approximately 1 hour. 15,000 cells were then added to each well; EBM was used in the negative control while growth factor-supplemented EBM (EGM) was used for all other groups (n=4). After 12 hours of incubation, cells were examined every hour to determine the optimal end-point. At 15 hours post-seeding, cells were treated with Hoechst (1 μ g/mL) for an additional 30 minutes, washed with DPBS, and imaged. To test the effect of B-PED on angiogenesis *in-vivo*, 1 mL of Matrigel (Corning) containing the appropriate treatment was injected into the caudal ventral area of Sprague-Dawley rats (negative: only Matrigel, positive: Matrigel + 1.5 μ g FGF-2, B-PED: Matrigel + 1.5 μ g FGF-2 + 10 mg B-PED). Matrigel plugs were extracted 10 days post-implantation and incubated at 37°C for 30 minutes in a solution of 4% paraformaldehyde (w/v) and 0.5% glutaraldehyde (w/v). Plugs were then treated with 1 mg/mL sodium

borohydride at 37°C for 4 hours. Samples were embedded in OCT and processed for IF staining as described above.

3.2.6 Antimicrobial Assays

Staphylococcus aureus were grown in 5 mL Tryptic Soy Broth (TSB) in a 15 mL falcon tube overnight at 37°C. The next day, 200 µL of the overnight culture was added to 20 mL TSB in a 50 mL falcon tube and grown for 2 hours until the optical density reached 0.1. 100 µL of the *Staphylococcus aureus* were then transferred to a 96 well plate, after which different concentrations of PED or B-PED were added (n=3, final concentration: 5, 2.5, 1.25, 0.625, 0.313, 0.156 mg/mL). The 96 well plate was then incubated in a shaker at 37°C for 5 hours; optical density measurements were carried out at 600 nm at 2, 3, and 5 hours post-treatment. Appropriate controls (positive control: 100 µg/mL timentin, negative control: TSB - no treatment) were utilized for this study.

3.3 Results and Discussion

3.3.1 Synthesis and Characterization of B-PED

B-PED synthesis is performed by grafting betaine onto PED, a previously-reported biodegradable ester [70]. Containing a primary amine group (**Figure 14A**), PED is amenable to conjugation with a variety of carboxylic acid derivatives. Despite the low solubility of betaine in DMF, excess betaine in the presence of a catalyst pushes the reaction forward, yielding an amber-colored

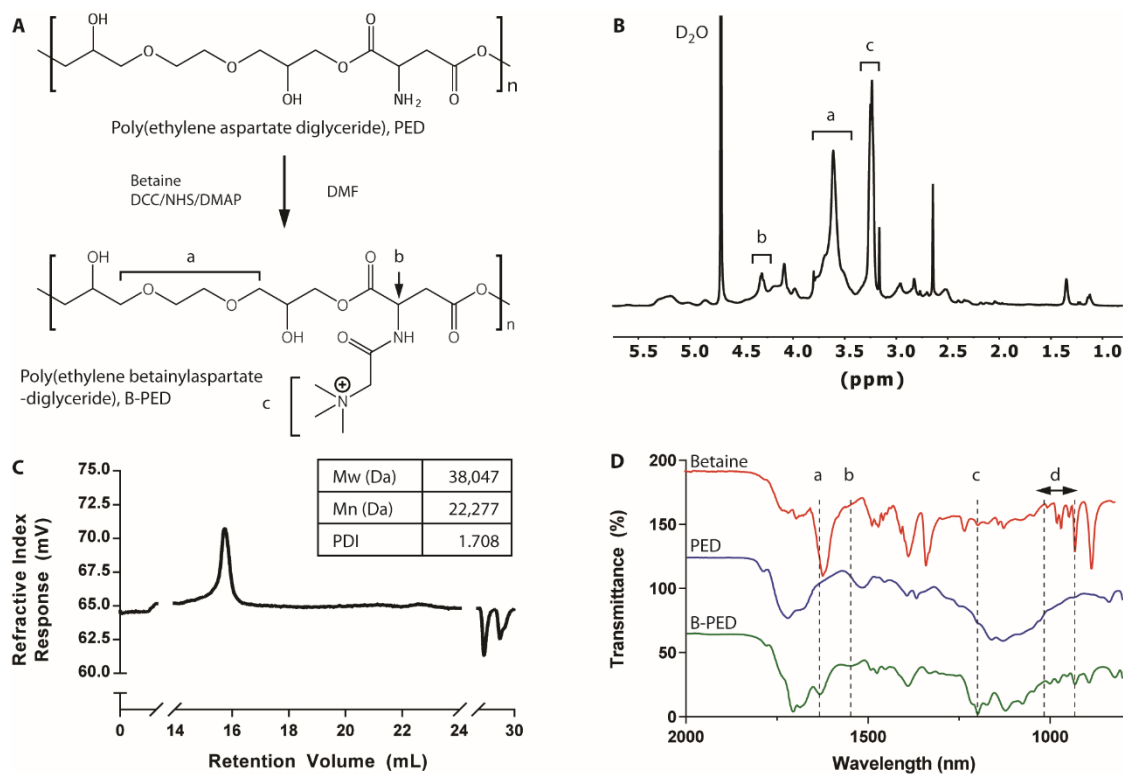


Figure 14. B-PED characterization. **A.** Betaine is grafted onto PED via an amide bond, yielding a polycation with a quaternary ammonium functional group. **B.** ¹H NMR spectrum of B-PED; (a) (ethylene glycol), (b) (α proton on aspartate), (c) (trimethyl amine) (solvent peak: δ 4.70). **C.** GPC of PED shows an M_w of 38 kDa; B-PED is estimated to have an M_w of 46 kDa. **D.** FTIR spectrum reveals successful betaine conjugation onto PED; (a and b) amide bond absorption; (c and d) absorption peaks from betaine.

product after 48 hours (**Figure 15**). The resulting B-PED contains a quaternary ammonium group, which confers a permanent cationic charge to the polymer. Purification via multiple precipitation steps and membrane dialysis removes all solvents and impurities, as indicated by the ¹H-NMR spectrum (**Figure 14B**). Protons in the ethylene glycol region of B-PED continue to produce a multiplet

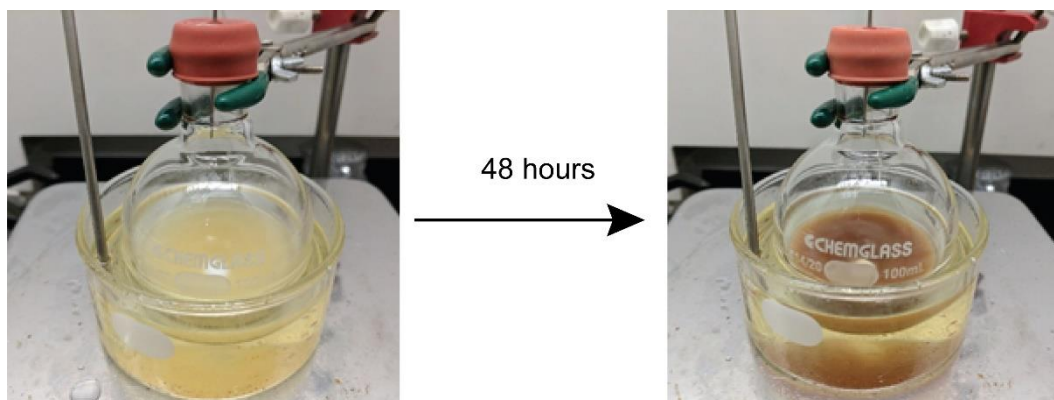


Figure 15. B-PED Synthesis.Conjugation of betaine onto PED yields a dark amber-colored product.

between δ 3.40 and δ 3.90 (**Figure 14B, a**). The conversion of the primary amine on aspartate to an amide bond results in a shift at 4.31 ppm, corresponding to the α proton of aspartate (**Figure 14B, b**). In addition, protons of the trimethyl amine generate a shift at 3.24 ppm (**Figure 14B, c**). Based on its NMR spectrum, B-PED has approximately 70% conjugation efficiency of betaine, yielding an extremely cationic polymer; zeta potential measurements of B-PED show a charge of 42.0 ± 2.3 mV (**Figure 16**). The molecular weight of B-PED was difficult to measure empirically due to the lack of a proper column for cationic polymers. Given the molecular weight of PED (**Figure 14C**) and the conjugation efficiency of betaine onto PED, we estimate an MW of approximately 46.46 kDa. FTIR spectroscopy of B-PED further corroborates the conjugation of betaine onto PED (**Figure 14D**). Clear differences are observed between PED and B-PED, in which absorptions at 1632 nm (“a”) and 1551 nm (“b”) correspond to amide I and II bonds, respectively. Furthermore, both betaine and B-PED show absorption at 1199 nm (“c”) and between 931 and 977

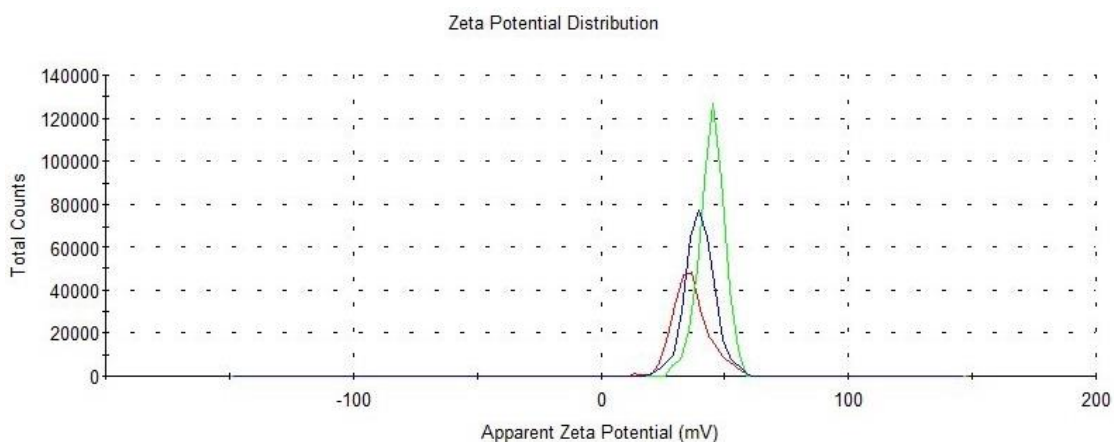


Figure 16. Zeta Potential of B-PED. B-PED has an average zeta potential of 42.0 ± 2.3 mV.

nm (“d”). Put together, these results demonstrate the successful synthesis of B-PED.

3.3.2 Biocompatibility of B-PED

Polycations such as poly(ethylenimine) and poly(L-lysine) generally exhibit poor biocompatibility, thereby limiting their widespread use. Given the relatively high conjugation efficiency of betaine onto PED, we examined the potential toxicity of B-PED on the metabolic activity and viability of NIH-3T3 fibroblasts and human umbilical vein endothelial cells (HUVEC). Both NIH-3T3 cells and HUVECs exhibit a corresponding increase in metabolic activity with [B-PED], peaking at 2.5 mg/mL (**Figure 17A**). At 10 mg/mL, both cell types show metabolic activity that is not significantly different from that of untreated samples, though it should be noted that NIH-3T3 cells are trending towards significance ($p=0.06$). An examination of DNA quantity shows a similar effect, in which a peak response is observed for NIH-3T3 cells at 1.25 mg/mL (**Figure**

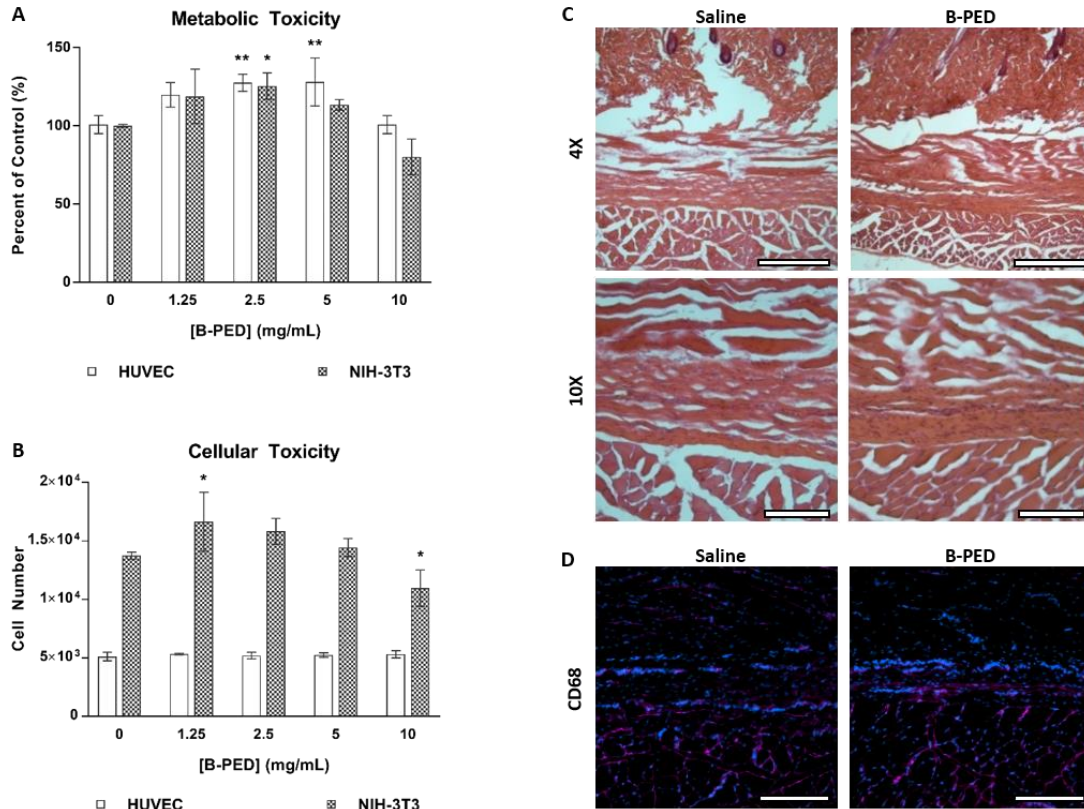


Figure 17. B-PED biocompatibility. **A.** The effect of [B-PED] on HUVEC and NIH-3T3 cells is assessed via a metabolic and (B) nucleic acid quantification assay ($n = 3$, mean \pm SD, * $p < 0.05$, ** $p < 0.01$ compared to control). **C.** 100 μL of physiological saline or 10 mg mL^{-1} B-PED is subcutaneously injected into Sprague-Dawley rats. Tissues are harvested 1 week post-injection and visualized via H&E staining (scale bar, top: 100 μm , bottom: 500 μm). **D.** CD68 immunofluorescence staining shows minimal macrophage infiltration for both saline- and B-PED-treated rats (red: CD68, blue: nuclei, scale bar: 200 μm).

17B). HUVECs, on the other hand, maintain a constant number of cells throughout, which may be more indicative of its longer doubling time. The increased level of metabolic and proliferative activity observed at low [B-PED]

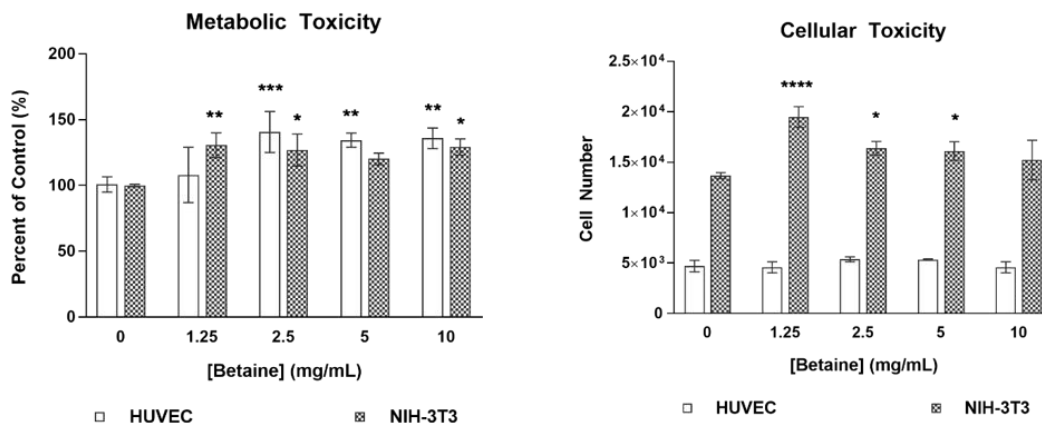


Figure 18. Toxicity of Betaine. Soluble betaine is added exogenously to cells and incubated for 24 hours. Cytotoxicity is assessed via CellTiter-Blue and PicoGreen (n=3, mean ± SD, *p<0.05, **p<0.01, ***p<0.0001 compared to control).

could be attributed to the protective effect of betaine on cells [111], though less likely given the lack of free betaine to act as an osmolyte. A more likely explanation is that a betaine-induced increase of intracellular calcium [112] leads to an upregulation of proliferative processes [113]. It should be noted that exogenously added betaine alone – concentrations of 1.25 mg/mL and above – results in an upregulation of metabolic activity for both cell types (**Figure 18**). Betaine-induced cellular toxicity shows a similar trend as cells treated with B-PED. On the other hand, treatment of NIH-3T3 cells with 10 mg/mL PED alone yields only 20% metabolic activity of untreated cells [114]. Put together, the slight toxicity of PED appears to be neutralized by the conjugation of betaine to its backbone.

The biocompatibility of B-PED was then examined *in-vivo*, in which 100 µL of saline or B-PED (10 mg/mL) was injected subcutaneously in rats. H&E

stains of tissues harvested 1 week post-injection show no significant difference in connective tissue and muscle morphology (**Figure 17C**). Furthermore, no appreciable inflammation is observed. Finally, macrophage infiltration for B-PED – assessed via CD68 immunofluorescence – is minimal and comparable to rats receiving saline injections (**Figure 17D**). Given the relative toxicity of poly(ethylenimine), in which cell viability is affected at concentrations as low as 0.01 mg/mL [115], these results collectively demonstrate B-PED as a biocompatible polycation.

3.3.3 Effect of B-PED on Angiogenesis

Betaine has been shown to exhibit anti-inflammatory and anti-angiogenic effects via suppression of NF- κ B and Akt signaling in- vitro [116]. Interestingly, we were unable to observe any anti-angiogenic effect of betaine on HUVEC tube formation (**Figure 19**). It should be noted that previous reports of betaine-induced anti-angiogenic behavior [116] utilized increasing doses of betaine up to 1 mM; the lowest [betaine] tested in this study is 1.25 mg/mL (10.7 μ M). Based on these comparisons, it appears that the anti-angiogenic effect of betaine is attenuated above a particular concentration. To assess how betaine-grafted polymer affects angiogenesis, we examined the effect of B-PED on HUVEC tube formation. B-PED concentrations up to 10 mg/mL were tested based on cell viability results; HUVECs exhibit no change in cell metabolism or viability at 10 mg/mL compared to baseline levels (**Figure 17A, B**). HUVECs

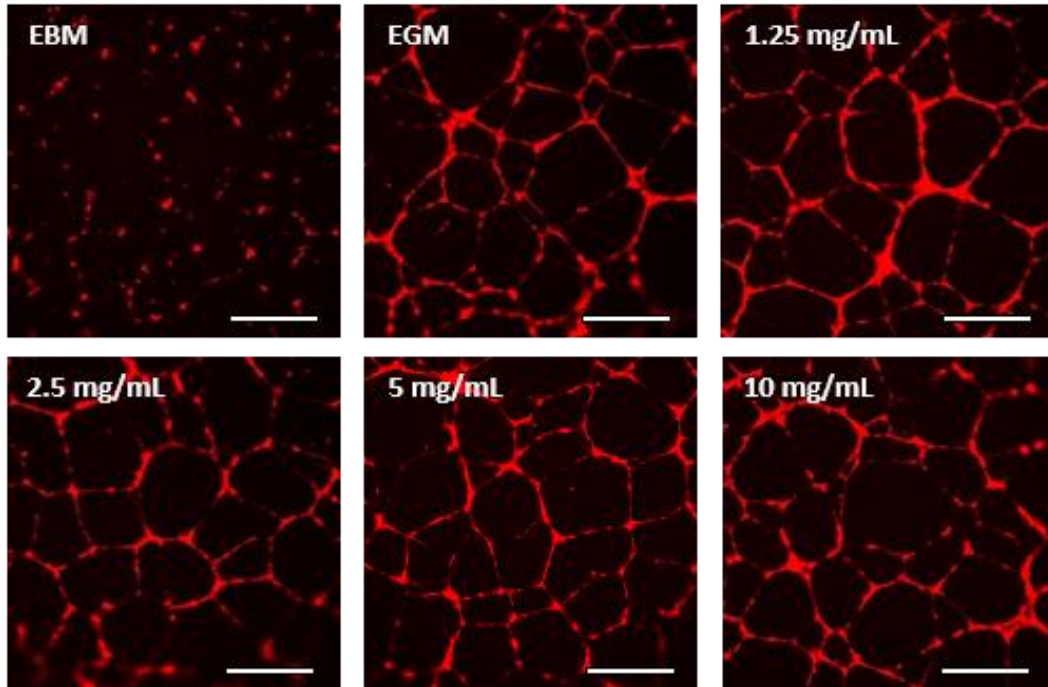


Figure 19. Effect of Betaine on *In-vitro* Angiogenesis. Exogenously added betaine has no effect on HUVEC tube formation (EBM: endothelial basal media, EGM: endothelial growth media). Cells are imaged 16 hours post-seeding (red: RFP, scale bar: 200 μ m).

cultured with basal medium (EBM) show an absence of tube formation while those cultured with growth factor-supplemented medium (EGM) develop well-connected tubes (**Figure 20A**). Increasing concentrations of B-PED lead to a progressive inhibition of tube formation, in which 10 mg/mL yields a similar anti-angiogenic effect as HUVECs in EBM. Quantification of the fluorescent images indicates a significantly lower number of network-forming-loops for cells treated with 2.5 and 5 mg/mL of B-PED than those treated with EGM or 1.25 mg/mL B-PED (**Figure 20B**). Treatment with 10 mg/mL of B-PED yields the smallest number of loops. While the number of junctions is also smallest for cells treated

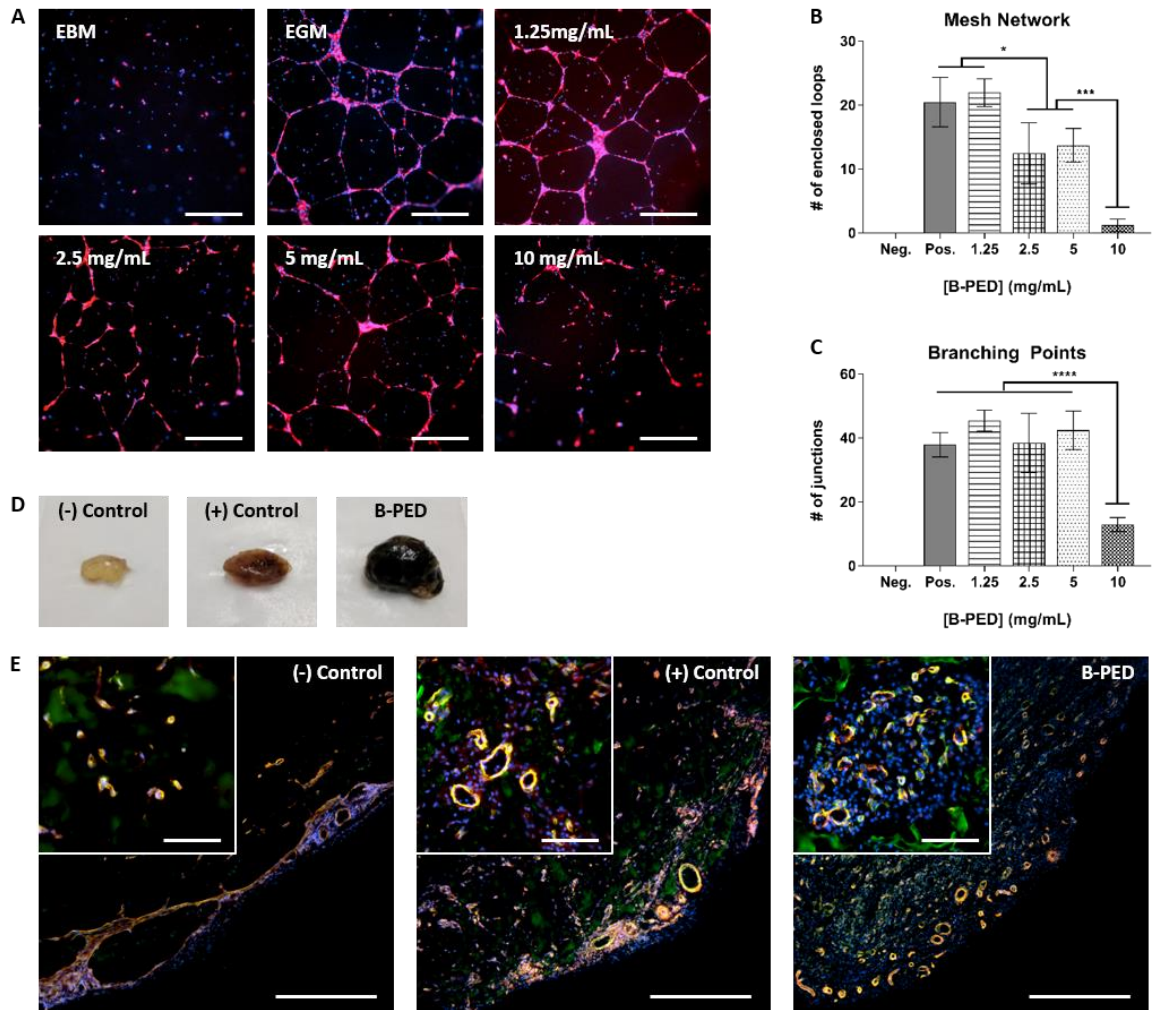


Figure 20. B-PED Effect on Angiogenesis. **A.** RFP-expressing HUVECs are cultured on basement membrane extract in the presence of varying [B-PED] (EBM: endothelial basal media, EGM: endothelial growth media). Cells are imaged 16 hours post-seeding (red: RFP, blue: nuclei, scale bar: 200 μ m). **B.** Number of enclosed loops forming a mesh network and **C.** number of junctions are quantified from immunofluorescence images (n = 4 wells, mean \pm SD, * p <0.05, *** p <0.001, **** p <0.0001). **D.** Matrigel plugs are injected subcutaneously into the caudal ventral area of Sprague-Dawley rats (negative: Matrigel, positive: Matrigel + 1.5 μ g FGF-2, B-PED: Matrigel + 1.5 μ g FGF-2 + 10 mg B-PED). Plugs are harvested 10 days post-implantation. **E.** Immunofluorescence staining of Matrigel plug sections show varying levels of angiogenesis (scale bar: 500 μ m, inset scale bar: 100 μ m).

with 10 mg/mL of B-PED, there is no statistical difference among lower concentrations of B-PED (**Figure 20C**). These *in-vitro* results demonstrate that betaine is also effective in suppressing angiogenesis when grafted onto a polymer.

Interestingly, *in-vivo* application of B-PED in a rat Matrigel plug assay results in an entirely different response. Gross visualization of representative Matrigel plugs collected 10 days post-implantation are markedly different from one another (**Figure 20D**), in which plugs without fibroblast growth factor 2 (FGF-2) are clear unlike those supplemented with FGF-2. In particular, the addition of B-PED (10 mg/mL) to FGF-2-supplemented Matrigel yield visibly larger and darker plugs. To better understand their cellular composition and blood vessel maturity, Matrigel plug explants were sectioned and assessed via double immunofluorescence staining against CD31 and α -SMA (**Figure 20E**). Both FGF-2-supplemented plugs with or without B-PED show mature blood vessels, in which pericytes (α -SMA: red) are co-localized with endothelial cells (CD31: green). However, Matrigel plugs containing B-PED exhibit higher vessel density than even the positive control, which may explain their darker color at a gross macroscopic level. Additionally, a large number of non-endothelial cellular infiltrates (DAPI: blue) are observed in plugs supplemented with B-PED, which could explain its relatively large size.

Betaine has been shown to stabilize proteins [107] and may have stabilized FGF-2 even in its grafted form. Given that monocyte/macrophage infiltration increases in the context of FGF-2-induced angiogenesis [117], the

CD31-/α-SMA- cellular infiltrates observed in plugs with B-PED could be macrophages. Furthermore, the pro-inflammatory environment promoted by macrophages has been reported to further activate FGF-2 and vascular endothelial growth factor (VEGF) secretion by endothelial cells [117]. In other words, although B-PED exhibits anti-angiogenic behavior *in-vitro*, its capacity to stabilize a large amount of FGF-2 (1.5 μg/plug/mouse) in a confined gel may have increased macrophage infiltrate and ultimately, angiogenesis, *in-vivo*. Finally, it should be noted that the average size of vessels in plugs containing B-PED are relatively small despite their high density. The inhibitory effect of betaine on cell migration [116] could have carried over to B-PED, but further studies elucidating the mechanism of betaine-induced anti-angiogenesis are needed to explain this discrepancy.

3.3.4 Antimicrobial Property of B-PED

The prevention and treatment of bacterial infections is of particular importance in the field of medicine, in which the emergence of bacterial resistance poses additional challenges. Glycopeptide antibiotics are a class of antimicrobial agents for gram-positive bacteria and bind to bacterial cell wall precursors that contain (D-Ala-D-Ala), thereby inhibiting their cell wall synthesis [118]. Recently, vancomycin, a widely-used antibiotic, was systematically modified to include additional modes of antimicrobial activity independent of (D-Ala-D-Ala) binding [110]. Of particular interest was the inclusion of a quaternary ammonium group, which was found to induce cell wall permeability. Given that betaine contains the same functional group, we assessed the effect of B-PED

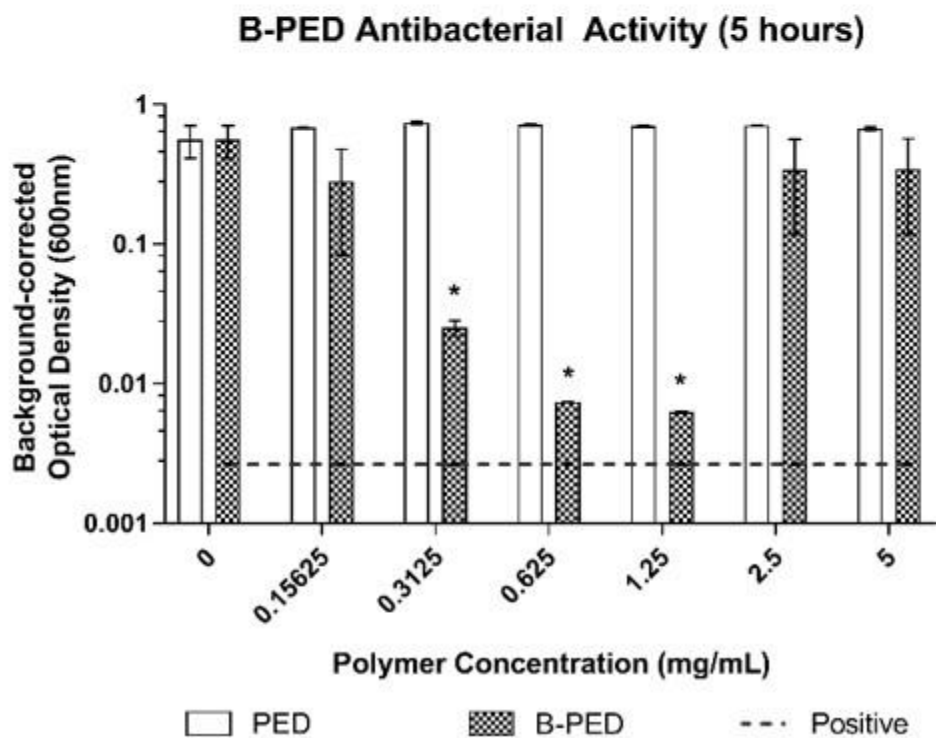
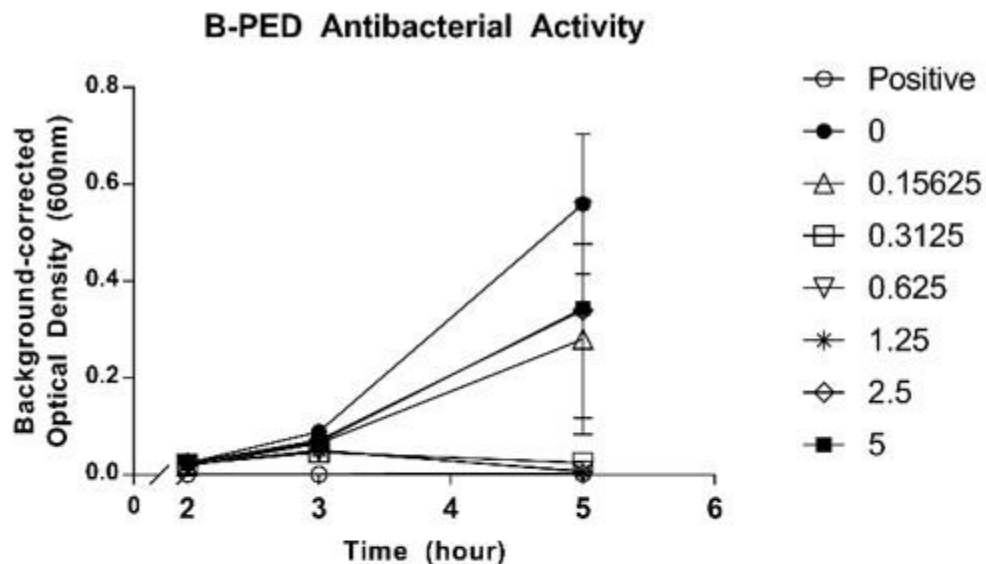


Figure 21. Antimicrobial Activity of B-PED. **A.** *Staphylococcus aureus* are cultured in the presence of varying [B-PED] and measured for absorbance to assess bacterial growth (positive: timentin, $n = 3$, mean \pm SEM). **B.** Antibacterial activity of PED is compared to B-PED 5 hours post-seeding (dashed line: positive control, $n = 3$, mean \pm SEM, * $p < 0.05$ compared to negative control).

on the growth of *Staphylococcus aureus*, a gram-positive bacteria predominant in skin infections and pneumonia.

The time-kill kinetics of B-PED at various concentrations demonstrate maximal anti-bacterial activity at 5 hours post-treatment (**Figure 21A**). On the other hand, bacteria treated with timentin (positive control) show a response as early as 3 hours. Upon closer inspection at 5 hours post-treatment, we observe a unimodal dose response, in which B-PED shows an optimal concentration range for anti-bacterial activity (**Figure 21B**). While lower and higher concentrations of B-PED appear to be ineffective in stemming *Staphylococcus aureus* growth, B-PED concentrations of 0.3125, 0.625, and 1.25 mg/mL show significantly lower levels of absorbance compared to that of untreated samples. As a control, *Staphylococcus aureus* were also incubated with PED, the backbone for B-PED. Increasing concentrations of PED have no effect on bacteria growth, thereby demonstrating that the anti-bacterial potency of B-PED is derived from the betaine side chain. It should be noted that the antimicrobial efficacy of B-PED exceeds or is comparable to other quaternary ammonium compound-based formulations. For instance, a cationic amphiphilic polycarbonate comprised of tetramethyl ammonium side groups shows activity against *Staphylococcus aureus* with a minimum inhibitory concentration (MIC) of 6.5 μM [119]. Similarly, the MIC₉₀ of cetyltrimethylammonium bromide (CTAB), a commercially-available antiseptic, is 0.128 mg/mL [120], or approximately 351 μM . B- PED shows an MIC of approximately 13.45 μM (0.625 mg/mL). On a side note, given that the mode of action of the quaternary

ammonium group is contact-mediated membrane permeabilization, the lack of anti-bacterial activity observed at higher B-PED concentrations may be due to polymer steric hindrance. Indeed, the molecular organization of cations within polycation aggregates has been shown to affect anti-bacterial activity, in which the size of aggregates and the number of active molecules that make up the aggregate play a determining role [121]. While we did not see [B-PED]-dependent aggregation (**Figure 22**), it is possible that the quaternary ammonium positive charge on B-PED is less accessible at higher [B-PED].

3.3.5 Complex Coacervate Behavior on B-PED

The conjugation of betaine onto PED yields a permanent positive charge per repeating unit via its quaternary ammonium functional group. Upon the addition of heparin, B-PED immediately self assembles into a complex coacervate, yielding a turbid solution (**Figure 23A**, top left). The low interfacial energy between the coacervate and coexisting supernatant phase [67] enables the coalescence of individual coacervate droplets into larger droplets over time (**Figure 23B**, bottom row). In the setting of a larger volume, an initially turbid solution of coacervate results in its sedimentation 24 hours post-mixing (**Figure 23A**, top right), which is easily resuspended by agitation.

The surface charge of B-PED and heparin coacervates is dependent on their relative ratio (**Figure 23B**). As expected, a low B-PED:heparin mass ratio results in a negative zeta potential (-38.9 ± 0.5 mV). An increase in the B-PED:heparin ratio progressively increases the zeta potential, ultimately reaching an isoelectric point at approximately 6.5:1. At higher mass ratios, the

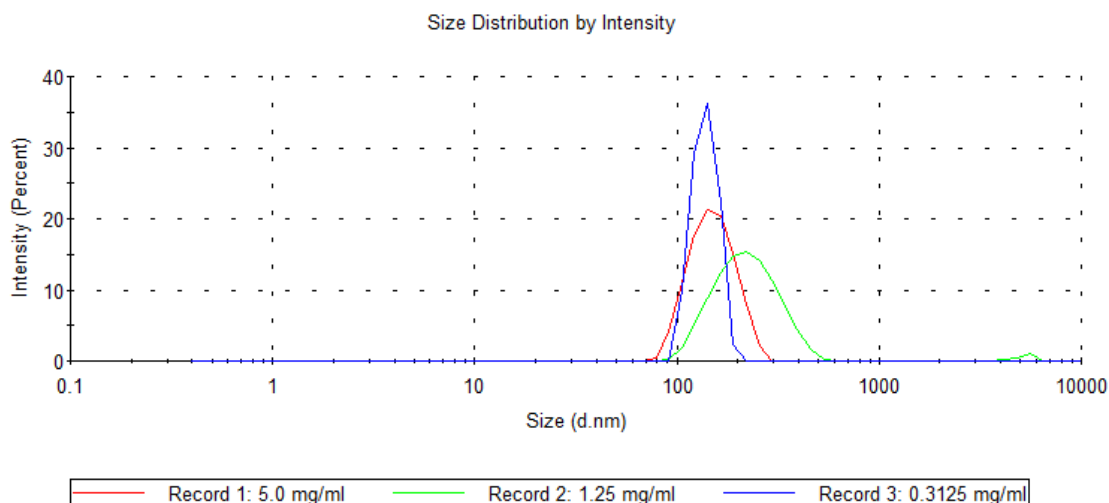


Figure 22. [B-PED] vs. Size. Different [B-PED] used in anti-bacterial experiments show no self-assembly or aggregation events.

excess B-PED acts to form positively-charged coacervates; the charge of B-PED alone is 42.0 ± 2.3 mV (**Figure 16**).

Finally, the effect of a competing salt on coacervation was assessed via DLS measurements (**Figure 23C**). In deionized water without NaCl (0% w/v), B-PED/heparin coacervates yield an average hydrodynamic diameter of 1477.7 ± 321.0 nm. The diameter slightly decreases to 1098.5 ± 343.8 nm in the presence of 0.9% saline. Further addition of NaCl to 1.8% w/v results in a non-uniform population of coacervates, with a primary peak diameter of 250.1 ± 24.9 nm. Apart from hydrodynamic diameter, the polydispersity index (PDI) of B-PED/heparin coacervates is relatively monodisperse for both 0% and 0.9% NaCl (**Table 2**). On the other hand, the PDI of coacervates prepared in 1.8% NaCl is much higher and reflective of the salt-induced decrease in interfacial energy between phases.

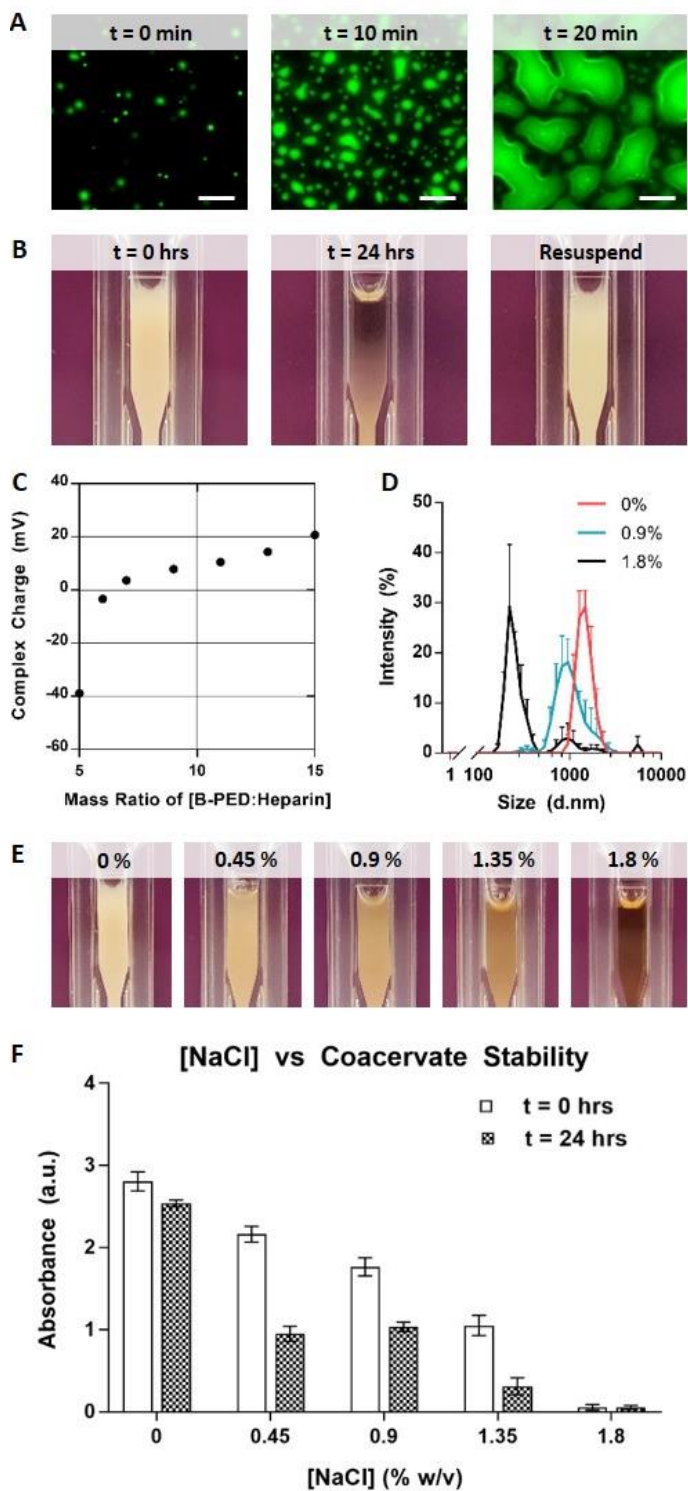


Figure 23. Complex Coacervation of B-PED and Heparin. **A.** Fluorescein-labeled heparin is used to visualize complex coacervation behavior at a microscopic level (scale bar: 20 μm). **B.** Macroscopic observation shows the

immediate formation of an off-white turbid solution, followed by a separation between the supernatant and coacervate phases within 24 hours; pipetting the solution resuspends the complex coacervate. **C.** Zeta potential measurements indicate a net neutral charge of B-PED/heparin complex coacervates is achieved at a mass ratio of 6.5 : 1 (B-PED :Heparin) (n = 3, mean \pm SD). **D.** Increasing [NaCl] decreases the hydrodynamic diameter of B-PED and heparin coacervates (n = 3, mean \pm SD). **E.** A visible reduction in turbidity is observed for increasing [NaCl] conditions (t = 0 h). **F.** The absorbance of various solutions is measured ($\lambda = 420$ nm) at t = 0 hours and 24 hours (after resuspension) (n = 3, mean \pm SD).

Macroscopic observation of B-PED/heparin coacervate solutions in different [NaCl] (0, 0.45, 0.9, 1.35, and 1.8% w/v) further corroborate the DLS data, in which increasing ionic strength progressively inhibits coacervate formation (**Figure 23E**). After 24 hours, all groups show a clear supernatant phase, in which sedimented coacervate phase is visible for [NaCl] of 0, 0.45, and 0.9% (**Figure 24**); resuspension of the B-PED/heparin coacervate yields a turbid solution again. Though [NaCl] of 1.35% initially yields a turbid solution, the solution remains clear after 24 hours, even after re-agitation. Taken together, the critical salt resistance of the B-PED/heparin coacervates is between 0.9% and 1.35%. It should be noted that any coacervate-based therapy would be performed in physiological saline ([NaCl] = 0.9%) within 10 minutes of preparation. Furthermore, subcutaneous or intramuscular injections are traditionally used, in which the supernatant phase would quickly disperse to leave behind the coacervate phase.

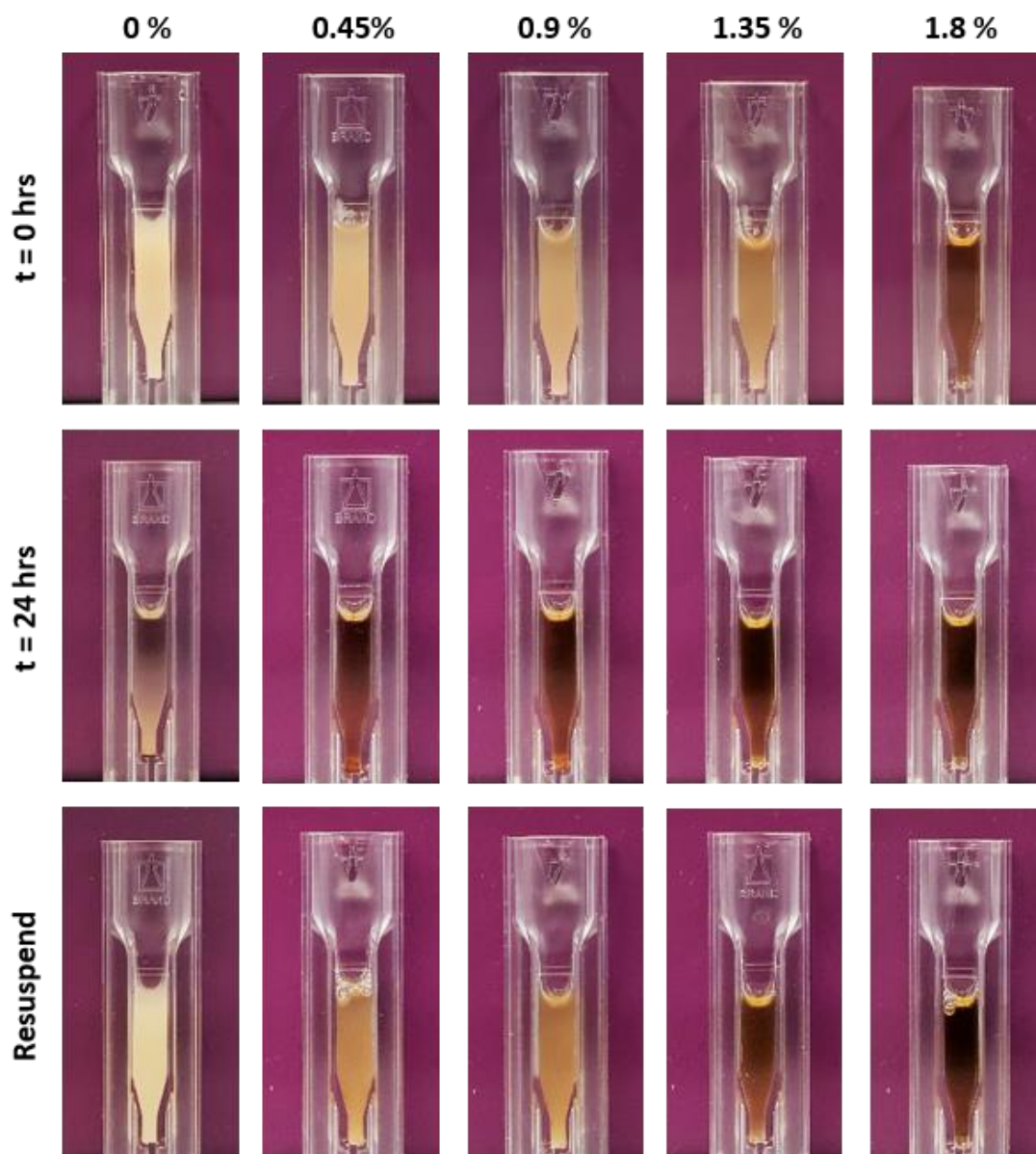


Figure 24. B-PED Complex Coacervate Behavior in Varying [NaCl].

Table 3. [NaCl] vs Coacervate Size and PDI

[NaCl] (% w/v)	Average Diameter (nm)	Average PDI
0.0	1477.7	0.166
0.9	1098.5	0.241
1.8	250.1	0.883

3.4 Conclusions

We designed a betaine-functionalized polycation, B-PED, to capitalize on the various properties of betaine. Despite the high betaine content and corresponding cationic charge of B-PED, excellent *in-vitro* and *in-vivo* biocompatibility was observed. Depending on the type of cell examined, B-PED also appeared to act as a proliferation agent at certain concentrations. In addition, B-PED elicited a dose-responsive decrease in angiogenesis *in-vitro*. Interestingly, the presence of B-PED increased angiogenesis *in-vivo* as assessed by a rat Matrigel plug assay. The *in-vivo* environment is far more complicated than the controlled cell culture environment; further mechanistic studies are required to explain the opposite effects. B-PED also exhibits an excellent unimodal antimicrobial response against *Staphylococcus aureus*. Finally, the strong positive charge of B-PED facilitates its complexation with heparin to form a stable coacervate. Given the anti-bacterial and pro-angiogenic activity of B-PED in the presence of FGF-2, we envision the potential utilization of B-PED/heparin coacervates for applications such as wound healing of the skin and open bone fracture.

Chapter 4.

Combined Delivery of IL-12 and α PD-1 Inhibitor via Single Injection of Anti-Angiogenic Hydrogel Improves Survival in Melanoma

Melanoma is refractory towards chemotherapy-based apoptosis and current clinical treatments are therefore dependent on the efficacy of checkpoint inhibitors such as α CTLA-4 or α PD-1 antibodies. While their use has improved overall patient response, the clinical benefit of utilizing checkpoint inhibitors alone is only observed in a subset of patients due to a prerequisite that the tumor is primed with immunogenicity prior to treatment. In this context, combining checkpoint inhibitors with an immune-activating cytokine is desirable. Herein, we examine for the first time the combination of recombinant IL-12, a potent immune-activator, and α PD-1 antibody in a preclinical murine melanoma model. To address potential issues of systemic toxicity and dose-associated costs, we demonstrate IL-12 and α PD-1 antibody delivery via a single injection of a polyrotaxane-based shear-thinning hydrogel. In addition, with cues from the anti-angiogenic nature of IL-12, we aim to further imbue anti-angiogenic properties to the delivery vehicle via the use of glycine betaine, which has demonstrated effects to this end. We demonstrate that IL-12 and α PD-1 antibody delivery leads to an intratumoral decrease in angiogenesis, increase in apoptotic/necrotic area, and increase in both innate and adaptive immune cells that collectively lead to significantly improved survival rates.

4.1. Introduction

Melanoma, a highly aggressive and deadly skin cancer, is rapidly increasing in its incidence rate despite increased public awareness and advances made in research. Conventional modes of treatment such as chemotherapy have proven to be ineffective in melanoma due to their inherent refractory nature towards apoptosis [7], leading to an average survival rate of less than one year [6]. While IL-2 showed early promise as a cytokine-based immunotherapy, leading to its FDA approval for melanoma in 1998 [11], its high toxicity and ambivalent roles towards cancer (*e.g.* redundancy with other immune-activating proteins such as IL-12 [15] and non-redundant factor in the proliferation of cancer-promoting regulatory T cells [16]) are attributed to its lackluster response rates [29].

In this context, the advent of checkpoint inhibitors for melanoma (*e.g.* α CTLA-4 and α PD-1 antibody) has led to vastly improved response rates and a concurrent explosion in the number of related studies. Unfortunately, they have demonstrated efficacy in only a subset of patients, in which recent studies have underscored the importance of priming the tumor environment to include a large number of lymphocytes, effectively rendering it “hot” [57, 59, 60]. In addition, the need for numerous injections have shed light on concerns over its high costs; the combined use of α CTLA-4 and α PD-1 checkpoint inhibitors for a typical patient would be close to \$300,000 while bi-weekly treatments for one year with α PD-1 antibody alone would generate an annual bill of over \$1,000,000 per

patient [31]. Furthermore, combination therapies with other checkpoint inhibitors have yielded better results yet at the cost of significant toxicities [30].

A decrease in systemic concentrations of therapy with an increase in its local concentration has always been a major need in any clinical setting, with recent studies in the field of immunotherapy underscoring this importance [122, 123]. With advances made in controlled delivery technology, combination therapies are now possible, in which the use of potent recombinant proteins needs to be reconsidered. Indeed, the use of α PD-1 antibody alone – controlled delivery or not – has not demonstrated significant benefit in tumor growth or survival [24, 124]. Furthermore, a recent study underscored the need for IL-12 for demonstrated PD-1 efficacy [125].

IL-12, unlike FDA-approved IL-2, convincingly activates the immune system by inducing IFN- γ secretion from numerous cell types [49, 76] while decreasing the proliferation of regulatory T cells [63]. In addition, IL-12 has been shown to exhibit anti-angiogenic behavior by inhibiting VEGF and MMP-9 levels [126, 127]. Unfortunately, early clinical trials with IL-12 were halted due to systemic toxicity-related deaths, ultimately leading way to vaccine and gene therapies. While significant advances have been made in this area, subpar transfection efficiencies and public apprehension due to the potential for undesired off-target genetic changes have limited its applications. In these regards, the combination of IL-12 and a checkpoint inhibitor for PD-1/PD-L1 has only been investigated for the treatment of cancer in a limited capacity [128, 129]. Importantly, the combined use of recombinant IL-12 and anti-PD-1

antibody – systemically or locally – has not yet been examined for its utility in melanoma.

In Chapter 2, we demonstrated the efficacy of a heparin-based complex coacervation platform to deliver IL-12 in B16F10 tumor-bearing mice, leading to significant improvements in tumor growth inhibition but not in survival. To determine the feasibility of α PD-1 antibody-loaded complex coacervates for co-delivery with IL-12, we examined whether or not antibodies could be loaded into coacervates (**Figure 25**). Unfortunately, IgG shows limited encapsulation efficiencies due to its small number of or lack of heparin-binding sites (31.06% in 0.9% saline and 0% in PBS) (**Figure 25C**). Therefore, to deliver α PD-1 antibody, we designed a polyrotaxane-based shear-thinning hydrogel amenable to injectable treatments. An additional consideration during the design of the controlled delivery vehicle for IL-12 and α PD-1 antibody was the anti-angiogenic property of IL-12. As a means to further increase anti-angiogenesis, we incorporated glycine betaine (betaine) into the hydrogel to imbue additional anti-cancer activity to the treatment; we have demonstrated the anti-angiogenic nature of a biocompatible betaine-grafted polyester in Chapter 3.

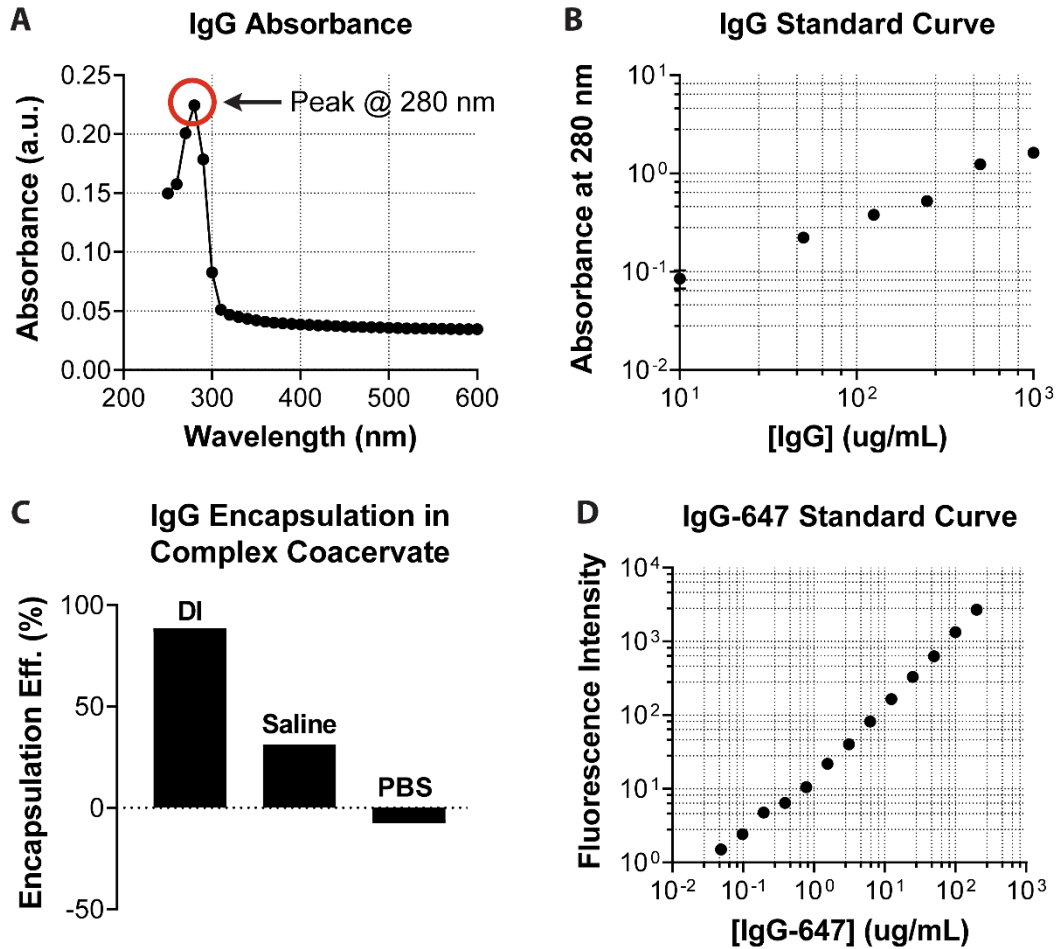


Figure 25. Antibody Does Not Load Into Complex Coacervates. **A.** The peak absorbance for IgG, a model protein for α PD-1 antibody, is at 280 nm. **B.** An IgG standard curve is prepared using absorbance values at 280 nm. **C.** 100 μ g IgG is loaded into complex coacervates prepared in various aqueous conditions and analyzed for encapsulation efficiency. **D.** IgG conjugated with Alexa Fluor 647 is used to generate a standard curve for subsequent release profiles of IgG; [IgG-647] is determined to be 16.55 μ M with a degree of labeling of 3.53

4.2 Materials and Methods

4.2.1 Materials

Ethylene glycol diglycidyl ether (EGDE) (Pfaltz & Bauer, Waterbury, CT), N-Boc-L-aspartic acid (Boc-Asp-OH), and N-Boc-L-arginine (Boc-Arg-OH) (Bachem Americas Inc.), tetra-*n*-butyl-ammonium bromide (TBAB, 98%+), trifluoroacetic acid (TFA, ≥99.5%), anhydrous dimethylformamide (DMF, ≥99.9%), *N,N'*-dicyclohexylcarbodiimide (DCC, ≥99%), and 4-(dimethylamino)pyridine (DMAP, ≥99%) (Alfa Aesar, Ward Hill, MA), *N*-hydroxysuccinimide (NHS, ≥98.0%) (Acros Organics, Geel, Belgium), betaine, deuterium oxide, poly(ethylene glycol) methyl ether, succinic anhydride, dibutyltin (IV) oxide, α -cyclodextrin, luer slip tip polypropylene syringe, and IgG from mouse serum (Sigma Aldrich, St. Louis, MO), ethyl ether and dichloromethane (Pharmco-Aaper), heparin sodium USP (Scientific Protein Labs, Waunakee, WI), bovine pancreas DNase I (Millipore, Billerica, MA), DMEM-high glucose supplemented with GlutaMAX, RPMI 1640 supplemented with L-glutamine and phenol red, 0.25% trypsin-EDTA, protease and phosphatase inhibitor mini tablets-EDTA free, collagenase IV, Nunc MaxiSorp flat-bottom plates, goat anti-rabbit-Alexa Fluor 594, goat anti-rabbit-Alexa Fluor 647, goat anti-rat-Alexa Fluor 594, goat anti-rat-Alexa Fluor 647, goat anti-mouse-Alexa Fluor 647, BSA-Alexa Fluor 647, Cytoseal 60, Alexa Fluor 647 protein labeling kit, rat IgG2a ELISA kit, Alexa Fluor 488 phalloidin, fixable viability dye eFluor 520, MiniCollect serum and plasma tubes, UltraComp eBeads compensation beads, ArC amine reactive compensation beads, RBC lysis buffer, Foxp3/transcription factor fixation/permeabilization

concentrate and diluent, permeabilization buffer, IC fixation buffer, OmniPur EDTA solution, RIPA lysis and extraction buffer, and Quant-iT PicoGreen dsDNA kit (Thermo Fisher Scientific, Waltham, MA), RPMI 1640 with L-glutamine and 25 mM HEPES, 96-well V-bottom plates, and Matrigel high concentration (Corning, Corning, NY), dialysis membrane tubing (Spectrum, New Brunswick, NJ), 30 μ m MACS SmartStrainers and CD45 TIL microbeads (Miltenyi Biotech, San Diego, CA), Eppendorf LoBind tubes (Eppendorf North America, Hauppauge, NY), MiniCollect Z serum separator tubes (Greiner Bio-One, Monroe, North Carolina), B16F10 melanoma cells (CRL-6475), RAW 264.7 cells (TIB-71), HUVEC cells (CRL-1730), and NIH-3T3 cells (CRL-1658) (ATCC, Manassas, VA), RFP-expressing HUVEC cells (gift from Dr. Steven R. Little), penicillin-streptomycin (Lonza, Basel, Switzerland), FGF-2 (Peprotech, Rocky Hill, NJ), recombinant murine IL-12 p70 (Peprotech, Rocky Hill, NJ), mouse IL-12 p70 antibody, mouse IL-12 biotinylated antibody, streptavidin-HRP, substrate reagent pack, Cultrex basement membrane extract (R&D Systems, Minneapolis, MN), aqueous paraformaldehyde (Electron Microscopy Sciences, Hatfield, PA), allergy syringe, PrecisionGlide hypodermic needles (25G), mouse IFN- γ OptEIA ELISA kit, rat anti-mouse CD8 α (clone 53-6.7), rat anti-mouse NKp46 (clone 29A1.4), and rat anti-mouse CD4 (clone RM4-5) (BD, San Jose, CA), rabbit anti-mouse FoxP3 antibody and YAP XP rabbit antibody (Cell Signaling Technology, Danvers, MA), rabbit anti-LYVE1 antibody, mouse anti-rat CD31 antibody, rabbit anti-rat α SMA antibody, rat anti-mouse CD31 antibody, and rabbit anti-mouse CD3 (Abcam, Cambridge, MA), rat PE anti-CD4

antibody, rat PE/Cy7 anti-CD4 antibody, rat PE anti-CD3 antibody, rat Alexa Fluor 647 anti-NK1.1 antibody, rat Alexa Fluor 647 anti-CD8 α antibody, rat Pe/Cy7 antiCD25 antibody, rat Alexa Fluor 647 anti-FoxP3 antibody, rat PE/Cy7 anti-IFN- γ antibody, rat anti-CD16/32 antibody, and cell activation cocktail (Biolegend, San Diego, CA), anti-mouse NK1.1 (clone PK136), anti-mouse CD8 α (clone BE0061), and anti-CD4 (clone GK1.5) (BioXcell, West Lebanon, NH) were all used as received.

4.2.2 PBP and PEAD Synthesis

The backbone of PBP, poly(ethylene aspartate diglyceride) (PED) was prepared via a polycondensation reaction as previously reported [70]. Briefly, EGDE (1000 mg), Boc-Asp-OH (1338.8 mg), and TBAB (5 mg) were dissolved in 0.6 mL of DMF. The mixture was reacted at 120°C under N₂ for 20 minutes in a microwave reactor (Biotage, Uppsala, Sweden). The resulting intermediate polymer, poly(ethylene boc-aspartate diglyceride) (PED-boc) was solubilized in 2 mL DCM and precipitated into diethyl ether. Boc was removed via addition of 5:1 DCM:TFA (v/v) ([TFA] = 2.5 mM). After 2 hours of stirring at room temperature, the solvent was subsequently removed via rotatory evaporation for 2 hours. Multiple precipitation steps in diethyl ether were used to remove excess reagents, including DMF and TFA. PED was then washed overnight in diethyl ether and dried under vacuum at room temperature until further use. PBP was then synthesized by grafting glycine betaine (betaine) and carboxylic acid-functionalized poly(ethylene glycol) methyl ether (mPEG-COOH) sequentially. Betaine-functionalized PED was first prepared as previously described [130].

PED (500 mg), betaine (381.4 mg), NHS (374.4 mg), DCC (806.1 mg), and DMAP (10.0 mg) were solubilized in DMF and reacted at 30°C for 24 hours under N₂. The betaine-conjugated PED (B-PED) was centrifuged twice to remove insoluble by-product. B-PED was then combined with mPEG-COOH (1659.6 mg), DCC (80.6 mg), NHS (37.5 mg), and DMAP (10.0 mg), and reacted at 30°C for another 24 hours. The product was then centrifuged, precipitated in ethyl ether, and washed overnight, and repeated once more for a total of two precipitations. The final product was dried overnight under vacuum at room temperature and dialyzed for 24 hours against DI water using a 7K snakeskin dialysis membrane. The product was lyophilized for at least 3 days before use. mPEG-COOH was synthesized as previously reported [131]. Briefly, poly(ethylene glycol) methyl ether (mPEG, 12.5 g), succinic anhydride (0.3 g), and dibutyltin oxide (1.37 mg) were combined in a round bottom flask. The mixture was reacted together at 180°C for 24 hours under N₂ and cooled to room temperature. The product was dissolved in 100 mL of DCM and the insoluble unreacted succinic anhydride was removed via centrifugation. The solution was concentrated via rotary evaporation and the resulting viscous solution was precipitated into ethyl ether and washed for 3 hours. The precipitate was collected by centrifugation, dissolved in DCM, precipitated in ethyl ether, and washed again for 3 hours. The precipitate was collected by centrifugation, decanted, and dried overnight under vacuum at room temperature. The product was dialyzed against DI water using a 1K MWCO dialysis membrane and lyophilized for at least 3 days before use.

4.2.3 Material Characterization

Conjugation of succinic anhydride to mPEG was verified via Fourier transform infrared spectroscopy (FTIR); mPEG-COOH was compared to mPEG. The M_w of PBP was analyzed via gel permeation chromatography (GPC, PG07) by PSS Polymer Standards Service (Mainz, Germany). 3 mg/mL of PBP was prepared in an aqueous solution of 0.1M NaCl and 0.1% (v/v) TFA, and filtered through a PTFE membrane prior to analysis with a PSS NovemeMax column (10 μ m, 2 \times 1000 angstroms) at 35°C. Calculation of the average molecular weights and molecular weight distribution was carried out using a slice-by-slice method based on a Pullulan calibration. ^1H nuclear magnetic resonance spectroscopy (^1H -NMR) was performed on PBP using deuterium oxide (D_2O) as a solvent (INOVA 600, Agilent, Santa Clara, CA). Results were analysed using TopSpin (Bruker, Billerica, MA). Dynamic light scattering (DLS) measurements were made by preparing 10 mg/mL sample solutions in deionized water. All solutions were filtered (0.2 μ m) and loaded in a polystyrene cuvette for measurements (Malvern Zetasizer Nano SZ90).

4.2.4 IgG Coacervate Preparation

Antibody loading into heparin-based complex coacervates was tested by loading 100 μ g IgG into 100 μ L coacervate. Coacervates were composed of heparin and PEAD, in which PEAD with higher conjugation efficiencies of arginine was used [132]. Briefly, 5 mg/mL PEAD and heparin solutions were prepared in DI water, 0.9% saline, or 1X PBS and filtered (0.22 μ m). IgG and heparin were first combined, then supplemented with PEAD to induce

coacervation; 3.6:1 = PEAD:heparin (mass ratio) was used. To test loading, IgG coacervates were centrifuged, after which the supernatant was analyzed via absorbance measurements at 280 nm. IgG conjugation to Alexa Fluor 647 was prepared according to the manufacturer's instructions. Briefly, 2 mg/mL IgG was incubated with reactive dye and eluted through a resin to purify IgG-647 from unbound IgG and AF-647.

4.2.5 Cell Culture and Proliferation Assay

NIH-3T3, RAW264.7, and B16F10 cell were cultured in DMEM, supplemented with 10% FBS and 1% penicillin-streptomycin. HUVECs were cultured in endothelial basal media (EBM). NIH-3T3, B16F10, and HUVECs were passaged using trypsin/EDTA prior to reaching confluence. RAW264.7 cells were passaged via gentle mechanical scrapping with a rubber policeman. Passage 3-5 were used for all experiments. For nucleic acid-based proliferation assays, 7500 cells were seeded per 96 well and allowed to adhere overnight. Cells (n=3) were then treated with varying [PBP] in the appropriate media and incubated for 24 hours before washing gently in PBS. Cells were lysed using cold lysis buffer and centrifuged to remove debris. Supernatents were analyzed using a PicoGreen assay according to the manufacturer's instructions and read out using a spectrometer (SpectraMax M3, Molecular Devices, San Jose, USA).

4.2.6 In-vitro and In-vivo Angiogenesis Assay

RFP-expressing HUVECs (Angio-Proteomie) were used to assess *in-vitro* angiogenesis. Briefly, basement membrane extract (reduced growth factor, Cultrex) was diluted to 10 mg/mL in sterile PBS. 70 μ L of the diluted basement

membrane extract was added to each 96 well and allowed to gel at 37 °C for approximately 1 hour. 15,000 cells were then added to each well; EBM was used in the negative control while growth factor-supplemented EBM (EGM) was used for all other groups (n=4). At 15 hours post-seeding, cells were treated with Hoechst (1 µg/mL) for an additional 30 minutes, washed with DPBS, and imaged. To test the effect of B-PED on angiogenesis *in-vivo*, a Matrigel plug assay was carried out in Sprague-Dawley rats. 1 mL of Matrigel (Corning) containing the appropriate treatment was injected into the caudal ventral area of rats (negative: only Matrigel, positive: Matrigel + 1.5 µg FGF-2, PBP: Matrigel + 1.5 µg FGF-2 + 30 mg B-PED). Matrigel plugs were extracted 10 days post-implantation and incubated at 37°C for 30 minutes in a solution of 4% paraformaldehyde (w/v) and 0.5% glutaraldehyde (w/v). Plugs were then treated with 1 mg/mL sodium borohydride at 37°C for 4 hours. Samples were embedded in OCT, sectioned at 10 µm thickness, and processed for immunofluorescence staining.

4.2.7 PBP Hydrogel Preparation

PBP hydrogels were prepared via a two-step process, in which PBP hydrogel is combined with PEAD cocervates in a 85:15 (v/v) ratio. For a 100 µL hydrogel with *in-vivo* applications, heparin (1 µL of 20 mg/mL), protein (3 µL), and PBP (11 µL of 272.7 mg/mL) were mixed together for 1 minute, followed by the addition of αCD (53.5 µL of variable [αCD] mg/mL) for another 5 minutes. Finally, antibody (16.67 µL) was added in and mixed for another 1 minute before the addition of protein-loaded cocervates prepared beforehand (15 µL);

coacervates were prepared as detailed above. After 1 more minute of mixing, PBP hydrogel/coacervate composite mixtures exhibited an opaque off-white color, yet was not fully gelled. The pre-gel formulation was then transferred to a sterile polypropylene syringe (*in-vivo* applications) or a 1.5 mL Eppendorf tube (*in-vitro* applications). All stock concentrations of components, except protein and antibody, were filtered (0.2 μm). [αCD] of 70, 80, and 90 mg/mL were tested.

4.2.8 PBP Hydrogel Characterization and Optimization

To examine PBP hydrogel crosslinking other than via gross visualization, the absorbance of PBP hydrogel was measured every minute for 90 minutes at 37°C; hydrogels were immediately transferred to 96 well plates before gelation and measured for absorbance at 450 nm ($n=3$). Samples visualized via airSEM were prepared immediately before analysis, transferred to a glass slide prior to complete gelation, and imaged within 2 hours of preparation; airSEM (B-nano) was performed using 30 kV beam energy, 2000 pA probe current, and a BSE detector. Samples visualized via SEM were prepared, transferred to a coverslip, lyophilized, transferred to stubs, and imaged; SEM (Keck) was performed at 3.00 kV with an aperture size of 30.00 μm . DLS measurements used to assess the effect of heparin on PBP were prepared by combining 10 mg/mL filtered PBP with varying amounts of filtered heparin. To assess degradation of the hydrogel *in-vitro*, 500 μL of gel without any protein was prepared and topped with 500 μL of 0.9% saline containing 0.1% BSA ($n=3$). Samples were incubated at 37°C and at set time points, they were decanted and lyophilized or replenished with fresh buffer. Determination of IL-12 release from the PBP and

coacervate composite platform was assessed in a similar manner; 500 ng of IL-12 was loaded into PBP hydrogels, topped with 500 μ L of 0.9% saline with 0.1% BSA, and incubated at 37°C. At each time point, samples were centrifuged and their supernatant was collected for analysis via ELISA. α PD-1 antibody release was modeled by examining IgG release, in which the fluorescence intensity of IgG-647 in the supernatant was measured over time; 100 μ g of total IgG-647 was loaded into each sample. To examine the rheological property of PBP hydrogel, oscillatory time sweep measurements were carried out at 37°C in the presence of a water solvent trap to minimize evaporation for the duration of the experiment. Samples were prepared, immediately loaded onto a 20 mm diameter parallel plate, and analyzed for both storage and loss modulus under a controlled strain of 1% and a frequency of 1 rad/s.

4.2.9 Animal studies

6-8 week old female C57BL/6J mice (strain 000664) were purchased from Jackson Laboratory. After at least three days of acclimation, mice were shaved and inoculated with bilateral injections of 200,000 B16F10 cells per site. B16F10 cells were maintained and propagated in DMEM supplemented with 10% FBS and 1% penicillin-streptomycin. After 9 days post-inoculation tumors became visible with a size of 25-50 mm², at which point mice were randomized into groups, ear-punched, and subcutaneously injected with 100 μ L of appropriate treatment. Treatment injections were only given to one primary site and include the following: 1) IL-12-loaded complex coacervates + IL-12/ α PD-1 antibody-loaded PBP hydrogel (n=12), 2) IL-12 + α PD-1 antibody in 0.9% saline (n=8),

3) complex coacervates + PBP hydrogel (n=8), and 4) 0.9% saline (n=5). Injections were given subcutaneously using a 25G needle. Tumor dimensions for both the primary and contralateral sites were measured every 2 days using a digital caliper. On days 1, 4, and 7, blood was collected from the lateral saphenous vein and removed of red blood cells and clotting factors to collect serum. Serum was stored at -20°C until analysis. On days 4 and 10 post-treatment, mice were euthanized, after which tumors and inguinal tumor-draining lymph nodes (dLN) were harvested. Organs used for flow cytometry were stored in RPMI 1640 supplemented with 10% FBS and 1% penicillin-streptomycin until cells were isolated. Organs used for immunofluorescence were fixed in 4% paraformaldehyde (1 hour for dLNs and 3 hours for tumors) at 4°C. For immune cell knockdown studies, mice were given intraperitoneal (IP) injections containing 200 µg of anti-CD4 (n=4), anti-CD8 (n=4), anti-NK1.1 antibody (n=4), or 0.9% saline (n=4) one day prior to subcutaneous treatment with the controlled delivery vehicle containing IL-12 and αPD-1 antibody. IP injections of corresponding antibodies were given twice a week at 100 µg/injection. For all experiments, mice were euthanized when tumors reached a size larger than 400 mm². Other causes for euthanasia included ulceration and bleeding of the tumor, lethargy, and cachexia. Data was compiled from two independent experiments.

4.2.10 Flow Cytometry

Spleen and dLNs were harvested and mechanically mashed on a 70 µm nylon mesh cell strainer pre-wet with FACs buffer (sterile filtered PBS supplemented

with 2% FBS, 1% penicillin-streptomycin, 5 mM EDTA, and 0.1% sodium azide). Tumors were weighed, minced, and incubated in dissociation buffer (sterile filtered RPMI 1640 supplemented with 1% penicillin-streptomycin, 5 mM CaCl₂, 1 mg/mL collagenase IV, and 10 mMU/mL DNase I) at 37°C for 45 minutes prior to mechanical isolation of cells. Cell suspensions were centrifuged, decanted, gently resuspended in RBC lysis buffer, incubated at room temperature for 2 minutes, and diluted in FACs buffer. Cells were centrifuged, resuspended in isolation buffer (sterile filtered PBS supplemented with 1% penicillin-streptomycin, 0.5% BSA, and 2 mM EDTA), and counted. For tumor-derived cells, samples were incubated further with CD45 microbeads at 4°C for 15 minutes, and magnetically separated. Viability dye was added to all cells. For cells requiring intracellular cytokine staining, samples were incubated with activation cocktail containing phorbol 12-myristate-13-acetate, ionomycin, and Brefeldin A, and incubated at 37°C for 5 hours. Cells were then washed in isolation buffer before incubation with viability dye. Samples were incubated with viability dye at 4°C for 30 minutes before dilution in FACs buffer. After centrifugation, cells were resuspended in FACs buffer and transferred to V-bottom 96 well plates. Samples were treated with CD16/32 antibody and incubated at 4°C for 10 minutes before addition of corresponding antibodies. Cells were incubated at 4°C for 1 hour, washed twice using FACs buffer, resuspended in fixation buffer, incubated at 4°C for 1 hour, and washed in permeabilization buffer twice before addition of antibodies for intracellular staining. After 30 minutes at room temperature, samples were washed twice in

FACs buffer and stored at 4°C until analysis via flow cytometry (BD Accuri C6). PE anti-mouse CD3 (#100205), PE/Cy7 anti-mouse CD4 (#100421), PE anti-mouse CD4 (#100407), Alexa Fluor 647 anti-mouse CD8 α (#100727), Alexa Fluor 647 anti-mouse NK1.1 (#108719), and PE/Cy7 anti-mouse CD25 (#101915) were used to stain surface cell markers while PE/Cy7 anti-mouse IFN- γ (#505825) and Alexa Fluor anti-mouse FoxP3 (#126407) were used to stain intracellular markers.

4.2.11 ELISA

Tumor digest solutions as prepared above were combined with protease inhibitor and RIPA lysis buffer and incubated on ice for 10 minutes. Samples were homogenized and centrifuged to remove cellular debris. These lysates, serum collected from mice, and *in-vitro* releasates were analyzed for IL-12 via an ELISA. Briefly, 100 μ L of 2 μ g/mL mouse IL-12 p70 antibody was added to 96 well Nunc MaxiSorp flat-bottom plates and incubated at 4°C overnight. After washing with wash buffer (PBS supplemented with 0.05% Tween 20) 4 times, wells were blocked with PBS supplemented with 1% BSA for 2 hours at room temperature. Wells were then washed 4 times and 100 μ L of sample was added to each well. After 2 hours incubation at room temperature, samples were washed with wash buffer 4 times, followed by incubation with 100 μ L of 0.2 μ g/mL biotinylated mouse IL-12 p70 antibody. After incubation at room temperature for 2 hours, samples were washed again with wash buffer 4 times. 100 μ L of streptavidin-HRP (1:200 v/v dilution) was added to each well and incubated at room temperature for 20 minutes. After 4 washes with wash buffer,

samples were incubated with 100 μ L of substrate solution and incubated for 20 minutes in the dark. 50 μ L stop solution was added to stop the reaction, after which samples were read at 450 nm and 540 nm. Serum samples collected from mice were also analyzed for [IFN- γ] and [α PD-1 antibody] by using a mouse IFN- γ OptEIA ELISA kit and a rat IgG2a ELISA kit, respectively, according to the manufacturer's instructions.

4.2.12 Tissue Staining and Imaging

Organs were fixed in 4% paraformaldehyde at 4°C for 1 or 3 hours for dLNs and tumors, respectively. Samples were washed in PBS and incubated in 30% (w/v) sucrose solution overnight at 4°C. Samples were then embedded in OCT, frozen on dry ice, sectioned at 10 μ m thickness, and stored at -20°C until ready for staining. To stain samples for immunofluorescence, slides were air-dried at room temperature for 20 minutes and incubated in PBS to remove OCT. Samples requiring permeabilization were incubated with 0.2% Triton X-100 in PBS for 10 minutes at room temperature and subsequently washed in PBS. Samples were blocked with 10% goat serum and 0.1% Triton X-100 and incubated at room temperature for 1 hour, after which primary antibody diluted in staining buffer (2% goat serum and 0.1% Triton X-100) was added. After an overnight incubation step at 4°C, samples were washed in staining buffer, and incubated with secondary antibody diluted in staining buffer. Samples were incubated at room temperature in the dark for 1 hour and washed in staining buffer. DAPI counterstaining was performed, washed in PBS and deionized water, and mounted in Cytoseal 60. Rat anti-mouse NKp46, rat anti-mouse

CD8 α , rat anti-mouse CD4, rabbit anti-mouse FoxP3, rat anti-mouse CD31, rabbit anti-mouse LYVE-1, rabbit anti-mouse YAP XP, mouse anti-rat CD31 antibody, rabbit anti-rat α SMA antibody, Alexa Fluor 488 phalloidin, goat anti-rabbit-Alexa Fluor 594, goat anti-rabbit-Alexa Fluor 647, goat anti-rat-Alexa Fluor 594, goat anti-rat-Alexa Fluor 647, and goat anti-mouse-Alexa Fluor 647 were used for immunofluorescence staining. To stain samples for hematoxylin and eosin (H&E), samples were sent to the Histology Lab at the Animal Health Diagnostic Center at Cornell University. H&E and immunofluorescence images were captured on an inverted microscope (Eclipse Ti2, Nikon).

4.2.13 Image and Statistical Analysis

All results were analyzed by one-way ANOVA with post hoc Tukey correction for multiple comparisons. Data from *in-vitro* PBP toxicity assays (n=4), quantification of *in-vitro* tube formation assay (n=4), PBP hydrogel pore size (collected from at least 5 separate fields of images), *in-vitro* release curves (n=4), PBP hydrogel degradation (n=3), PBP hydrogel rheological measurements (n=3), animal studies (G1: n=12; G2: n=8; G3: n=8; G4: n=5), survival studies (n=4 for all groups), serum protein concentrations (n=6 for D1 and D4; n=4 for D7), intratumoral concentrations of IL-12 (n=3), quantification of collapsed blood vessels (collected from 3 separate image fields), quantification of apoptotic/necrotic areas (collected from 3-6 separate image fields), number of LECs (n=3), and all data from flow cytometry experiments (n=2) represent mean \pm standard deviation. Image quantification was carried out using ImageJ software.

4.3. Results and Discussion

4.3.1 PBP Synthesis and Characterization

PBP synthesis is performed by grafting glycine betaine (betaine) and methoxy carboxylic acid-functionalized poly(ethylene glycol) (mPEG-COOH) sequentially onto PED, a previously-reported biodegradable ester. The higher solubility of PEG in DMF than glycine betaine prevents their simultaneous conjugation as the preferential conjugation of PEG spatially impedes betaine access to primary amine sites. mPEG-COOH is prepared separately via a ring opening reaction with succinic anhydride and the successful conjugation is assessed via Fourier transform infrared spectroscopy, in which peaks corresponding to the carbonyl stretch and C-H stretch verify the presence of a carboxylic acid (**Figure 26**). The conjugation of betaine onto PED yields a dark amber colored product as previously described [130]. Urea by-product is

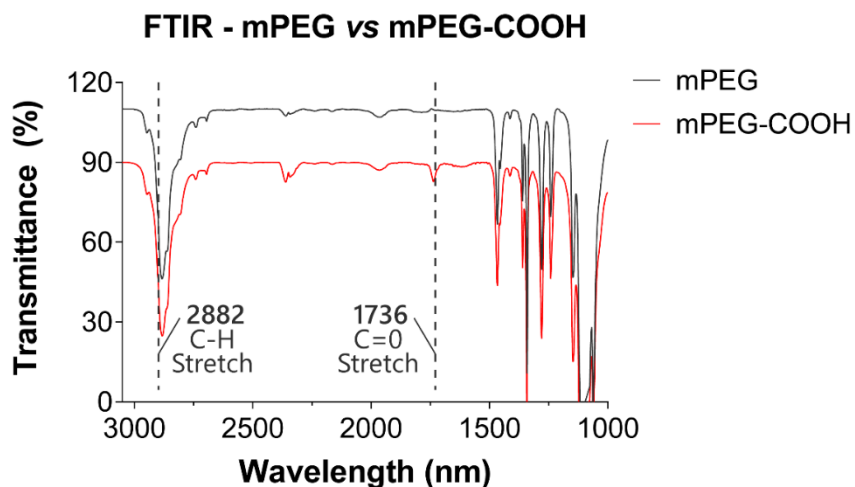


Figure 26. Fourier Transform Infrared Spectroscopy of mPEG-COOH.Characteristic carbonyl (ca. 1736 nm) and C-H stretch peaks (ca. 2882 nm) correspond to the successful conjugation of succinic anhydride to the end of methoxy PEG.

removed by centrifugation prior to the addition of mPEG-COOH with fresh NHS/DCC conjugation reagents. The resulting betaine- and mPEG-functionalized PED (PBP) contains both a quaternary ammonium group, which confers a positive charge to PBP, and a PEG linker. The PEG is functionalized as a means to create a physically crosslinked hydrogel via complexation with α -cyclodextrin (α CD) [133]. PBP is purified via multiple precipitation steps and membrane dialysis to ensure removal of solvents and impurities, as indicated by the $^1\text{H-NMR}$ spectrum (**Figure 27A**). A broad peak between *ca.* δ 4.84 and *ca.* δ 5.47 corresponds to the hydroxy protons on the backbone of PED (“a”). Protons corresponding to the ethylene glycol of mPEG shows up as a sharp peak between *ca.* δ 3.40 and *ca.* δ 3.90 (“b”) while those from the methoxy generate a shift as a singlet at *ca.* δ 3.39 (“c”). On the other hand, the trimethyl amine on betaine generates a shift at 3.31 ppm (“d”) and a peak at *ca.* δ 3.27 corresponds to the α proton of betaine (“e”). Based on this spectrum, the actual PEG conjugation efficiency is determined via the ratio in integral area between H_a to H_c while that of betaine is determined via the ratio in integral area between H_a and H_{d+e} . PBP has approximately 25.8% mPEG and 14.2% betaine conjugation efficiency, yielding a cationic PEG-functionalized polyester; zeta potential (ζ) measurements indicate an average charge of 10.93 ± 0.23 mV (**Figure 27D**). The M_w of PBP is 12,600 Da as assessed via GPC in an aqueous eluent with 0.1M NaCl + 0.1% (v/v) trifluoroacetic acid (**Figure 27C**). This Pullulan equivalent mass greatly underestimates the absolute value of PBP as the M_w of PED is 38,047 Da [130]. The brush polymer structure conferred by the

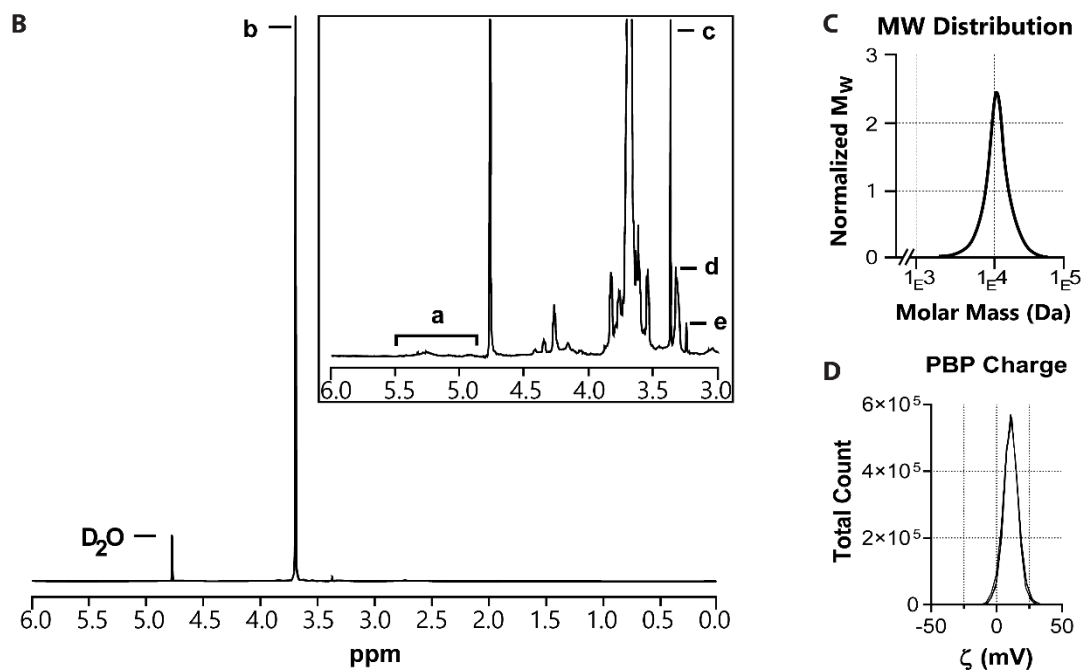
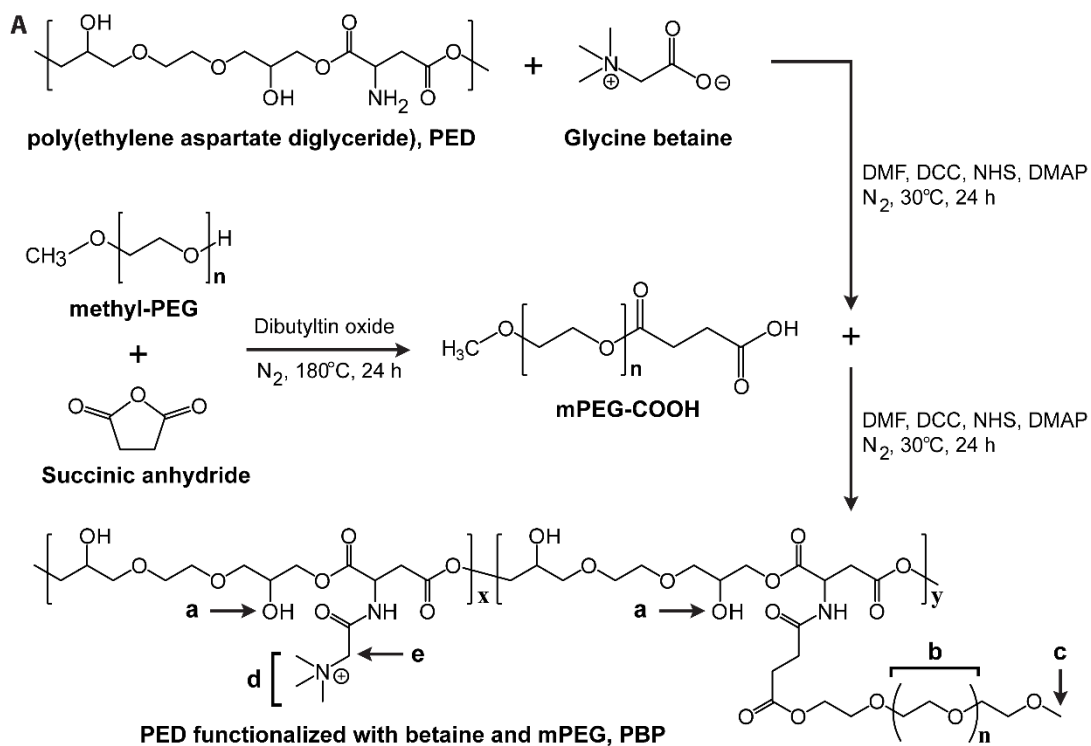


Figure 27. PBP Synthesis and Characterization. **A.** PED is grafted sequentially with betaine and mPEG-COOH to yield PED functionalized with betaine and mPEG (PBP). **B.** ¹H-NMR spectrum of PBP; (a) hydroxy group, (b) ethylene glycol, (c) methoxy group, (d) trimethyl amine, and (e) α proton on

betaine grafted onto PED (solvent peak: δ 4.70). **C.** GPC of PBP shows a M_w of 12,600 Da based on a Pullulan calibration. **D.** Dynamic light scattering (DLS) measurements are made ($n=3$).

relatively long PEG chains (average $M_n = 5000$ Da) are the likely to confound the M_w and M_n values; the PDI of PBP is relatively small at 1.33. The conjugation efficiency of PEG is over the theoretical limit of 20%, in which the overestimation is most likely due to the overlap of proton signals by the ethylene glycol on the PED backbone. Collectively, these results indicate the successful synthesis of PBP, which is used to create a physically-crosslinked hydrogel.

4.3.2 PBP Inhibits *In-vitro* and *In-vivo* Angiogenesis

The PBP polycation is then assessed for its biocompatibility on various cells via nucleic acid quantification (**Figure 28**). PBP is well tolerated up to high doses in a dose-responsive manner. In particular, it elicits significant cytotoxicity on NIH-3T3 fibroblasts ($50.44 \pm 15.51\%$ of untreated cells) and human umbilical vein endothelial cells (HUVECs) ($63.42 \pm 12.82\%$ of untreated cells) only at the highest concentration tested (45 mg/mL). Interestingly, PBP elicits a unimodal proliferation response of RAW264.7 macrophages, with a significant increase observed at 15 mg/mL ($146.59 \pm 21.02\%$ of untreated cells). PBP did not show any significant changes in the viability of B16F10 melanoma cells. It should be noted that in the context of an anti-cancer application, betaine has been shown to inhibit NF κ B [116, 134], which together with HIF1 α is activated in cancers for its growth and resistance to chemotherapy [135]. We were unable to observe these results *in-vitro* from a proliferation standpoint. However,

previous reports on the effect of betaine on NFκB [116, 134] utilized much lower doses; it is possible that there is a dose response in which these effects are observed. Collectively, given these results, we decided to use PBP at a concentration of 30 mg/mL for all subsequent experiments.

We previously demonstrated the anti-angiogenic nature of betaine-conjugated PED [130] and set out to assess the effect of PBP on both *in-vitro* and *in-vivo* angiogenesis. Concentrations of up to 30 mg/mL PBP were incubated with RFP-expressing HUVECs and assessed for tube formation 15 hours later (**Figure 29A**). When compared to the positive control (endothelial growth media – EGM), increasing concentrations of PBP led to a progressive inhibition of tube formation, in which 30 mg/mL PBP treatment elicited a similar anti-angiogenic response to what was observed in the negative control (endothelial basal media – EBM). Quantification of the fluorescent images for junctions and network-forming loops corroborates our observations, in which anti-angiogenic effects are observed starting at [PBP] of 15 mg/mL (**Figure 29B**).

In-vivo application of PBP in a rat Matrigel plug assay further exemplifies the anti-angiogenic nature of PBP. Gross visualization of representative FGF-2-supplemented plugs (*cf.* negative control does not have FGF-2) 10 days post-implantation indicates that 30 mg/mL PBP prevents angiogenesis *in-vivo* (**Figure 29C**); rats receiving FGF-2 without PBP have a darker red plug compared to the other groups. A closer look at the cellular composition of the plugs was then assessed via immunofluorescence against CD31 (green) and α-SMA (red) (**Figure 29D**). Not surprisingly, Matrigel plugs without FGF-2

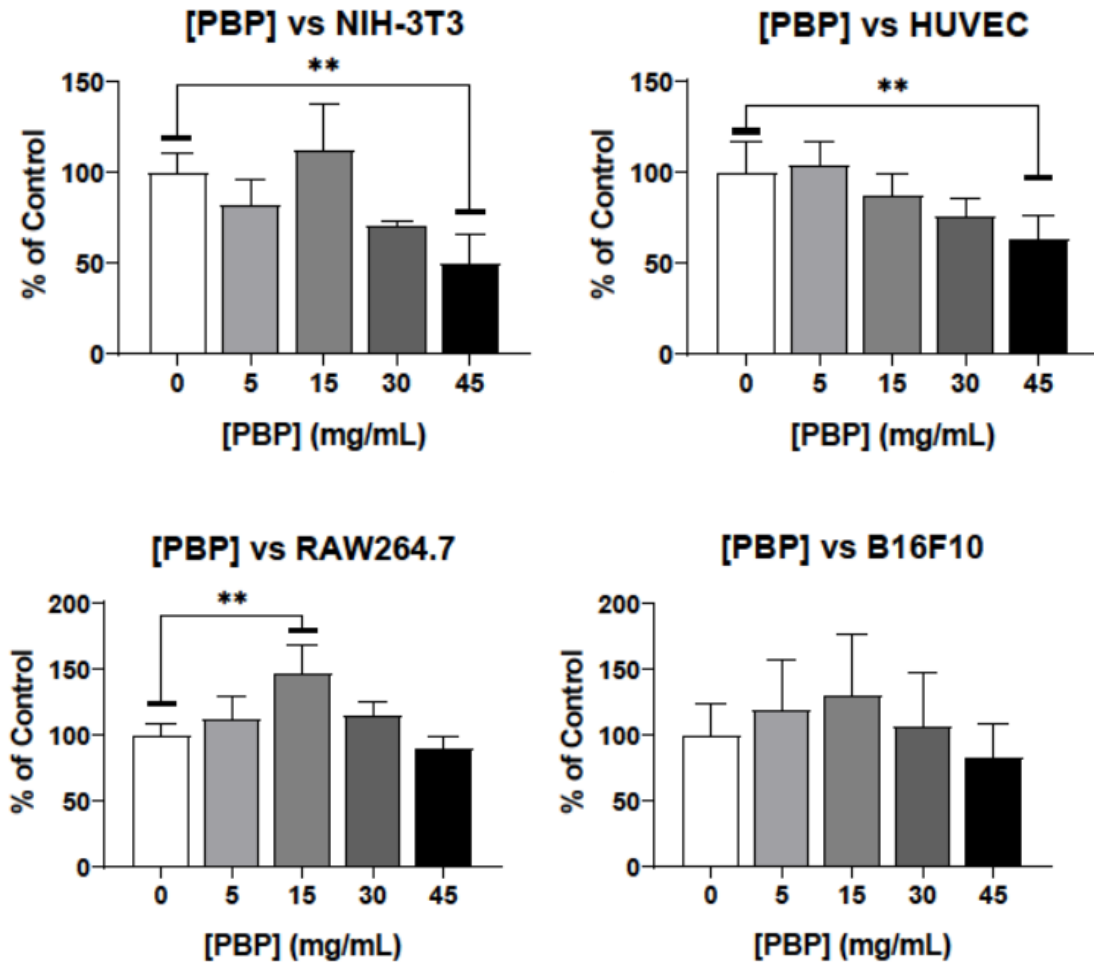
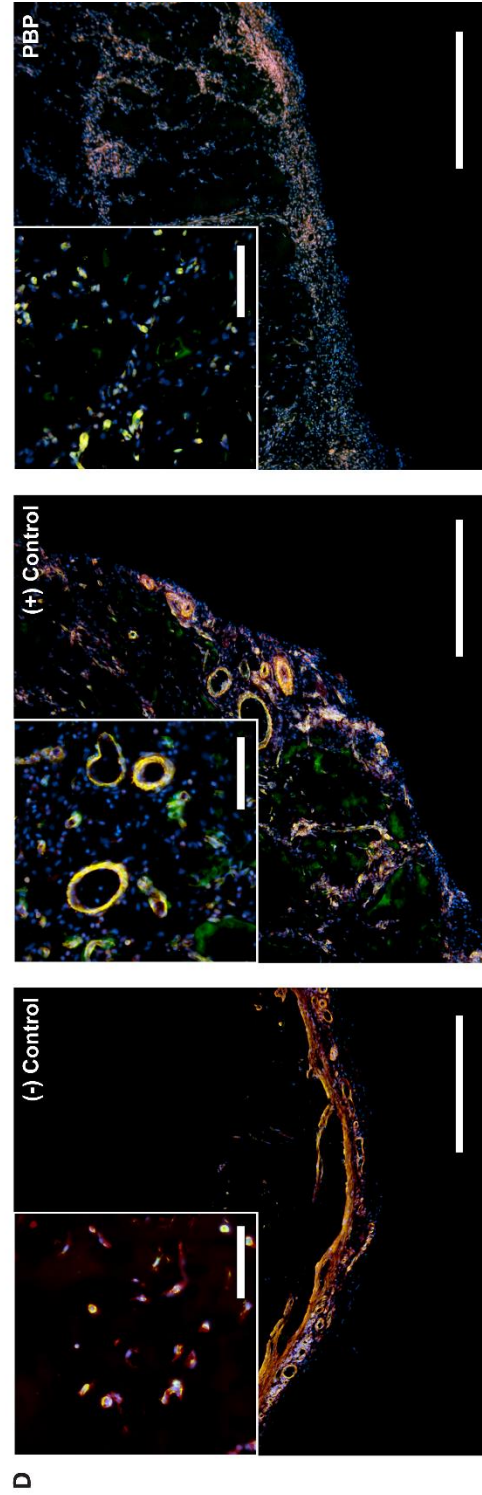
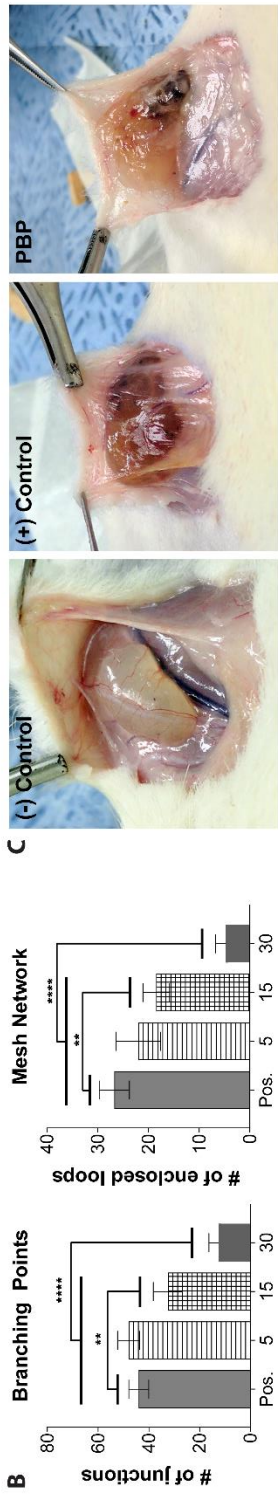
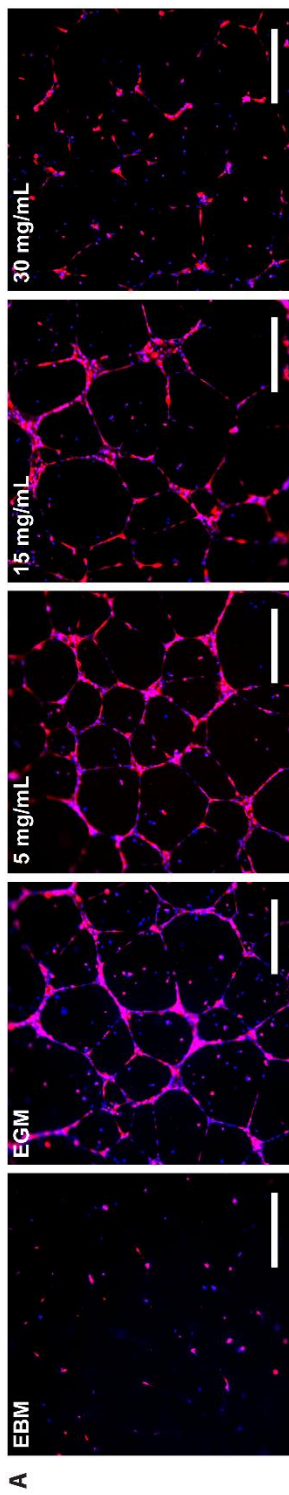


Figure 28. Nucleic Acid-based Toxicity of [PBP]. Varying concentrations of PBP are incubated with NIH-3T3, HUVEC, RAW 264.7, and B16F10 for 24 hours and analyzed via a PicoGreen DNA quantification kit (n=4, mean \pm SD, ordinary one-way ANOVA with post-hoc Tukey correction for multiple comparisons, **p<0.01)

(negative control) show minimal angiogenesis, with any blood vessel formation observed being limited to the periphery. On the other hand, Matrigel plugs with the FGF-2 (positive control) show robust levels of angiogenesis, both at the peripheral and center. Upon the addition of PBP, however, a massive decrease in angiogenesis is observed, in which numerous CD31+ cells are present in the

Figure 29. PBP Restricts *In-vitro* and *In-vivo* Angiogenesis.**A.** Representative images of RFP-expressing HUVECs cultured on basement membrane extract in the presence of varying [PBP] for 16 hours (EBM: endothelial basal media, EGM: endothelial growth media, red: RFP, blue: nuclei, scale bar: 200 μ m). **B.** Number of branching junctions and completely enclosed loops are quantified from immunofluorescence images (n=4 wells, mean \pm SD, ordinary one-way ANOVA with post-hoc Tukey correction for multiple comparisons, **p<0.01, ****p<0.0001). **C.** Matrigel plugs are injected subcutaneously into the caudal ventral area of Sprague-Dawley rats and harvested 10 days post-implantation (negative: Matrigel, positive: Matrigel + 1.5 μ g FGF-2, B-PED: Matrigel + 1.5 μ g FGF-2 + 30 mg PBP). **D.** Representative immunofluorescence images of Matrigel plug sections against CD31 and α SMA demonstrate effect of PBP on *in-vivo* angiogenesis (green: CD31, red: α SMA, blue: nuclei, scale bar: 500 μ m, inset scale bar: 100 μ m).



gel. Interestingly, any CD31+ α -SMA+ cells show an inability to form tubular structures. The inhibitory nature of betaine on cell migration [116] is one potential reason behind this phenomenon but further studies elucidating the mechanism are required. Finally, it should be noted that such anti-angiogenic assays could not be carried out on the final PBP hydrogel platform as a Matrigel plug assay requires an injection, in which the spatial segregation and gelation of a shear-thinning PBP hydrogel would be difficult to control. Given that our proposed PBP hydrogel is a physically-crosslinked hydrogel, dissociation *in-vivo* into PBP polymers is expected to elicit similar anti-angiogenic effects.

4.3.3 Optimization of PBP-based Hydrogel

To determine optimal PBP-based hydrogel formation, we assessed the effect of various α CD concentrations. α CD is used with PEG to spontaneously form pseudopolyrotaxanes [133, 136], which has been shown to be stable despite the lack of covalent bonds due to the high activation energy needed [137] to withdraw the α CD ring from the PEG axis. A previous report by our group using a similar polymer in the presence of heparin indicates an α CD dose-responsive change in rheological properties of the resulting hydrogel [131]. An initial test using 80 mg/mL α CD (α CD₈₀) with 30 mg/mL PBP indicates the successful formation of a hydrogel within 10 minutes of mixing (**Figure 30A**). The effect of [α CD] below and above the tested 80 mg/mL was visualized at a macroscopic level, in which we observed an increase in the opacity of PBP hydrogel with increasing [α CD] (**Figure 30B**, inset and **Figure 31**). All [α CD] tested eventually yielded a white solid after sufficient time, which may be more

a result of an increase in $[\alpha\text{CD}]$ artificially induced due to solvent evaporation. We then examined the effect of $[\alpha\text{CD}]$ on its ability to induce variable pore sizes in the resulting PBP hydrogel. To visualize the pore sizes of PBP hydrogels in its native state, airSEM was utilized. Large pore sizes dominate the PBP hydrogel when prepared with the $[\alpha\text{CD}]_{70}$. At $[\alpha\text{CD}]_{80}$ and $[\alpha\text{CD}]_{90}$, regularly-spaced pores of smaller size were observed. Quantification of the airSEM images shows a large distribution of pore sizes with a diameter of $73.95 \pm 54.68 \mu\text{m}$ for $[\alpha\text{CD}]_{70}$, significantly larger than those of $[\alpha\text{CD}]_{80}$ and $[\alpha\text{CD}]_{90}$ (**Figure 30C**). Furthermore, while the diameter for $[\alpha\text{CD}]_{80}$ ($3.45 \pm 4.32 \mu\text{m}$) and $[\alpha\text{CD}]_{90}$ ($5.89 \pm 6.34 \mu\text{m}$) are not significantly different, they are trending towards significance ($p=0.0627$).

The addition of heparin to a polyrotaxane based on an arginine-based polyester with αCD has been shown to improve the modulus of the resulting hydrogel due to the formation of secondary ionic crosslinks between heparin and cationic sites on arginine [131]. In the context of immunotherapeutic protein delivery, heparin has been shown to increase the bioactivity of IL-12 [69]. It is important to note, however, that excess heparin unbound to protein would competitively bind to betaine sites on PBP, resulting in a relatively quick release of heparin-IL-12 complexes. To prevent such a burst release, we titrated PBP with varying amounts of heparin and assessed the zeta potential of the resulting complex via DLS (**Figure 30D** and **Figure 32**). A mass ratio of 10% heparin as used in the previous study shows a charge of $-11.27 \pm 0.38 \text{ mV}$. Indeed, when we examine the release behavior of IL-12 from a PBP hydrogel prepared with

Figure 30. PBP Hydrogel Optimization.**A.** Gross macroscopic visualization of PBP supplemented with 80 mg/mL α CD demonstrates successful formation of opaque hydrogel after approximately 10 minutes post-mixing. **B.** PBP is supplemented with varying [α CD]. Inset image refers to droplet of resulting hydrogel 10 minutes post-mixing. Representative airSEM images of PBP hydrogels immediately after formation are shown (scale bar: 10 μ m). **C.** Pore sizes are quantified from at least 5 separate airSEM images (ordinary one-way ANOVA with post-hoc Tukey correction for multiple comparisons, **** $p < 0.0001$). **D.** PBP (10 mg/mL) is titrated with varying mass ratios of heparin and analyzed via DLS. **E.** IL-12 (500 ng) is encapsulated into PBP hydrogels formulated with two different heparin:PBP ratios and incubated at 37°C in 0.9% saline supplemented with 0.1% BSA. Supernatants are collected and analyzed via ELISA (n=4). **F.** PBP hydrogels with 1:150 = heparin:PBP (mass ratio) are prepared and incubated at 37°C in 0.9% saline supplemented with 0.1% BSA. Samples are collected at each time-point and lyophilized prior to weighing; remaining mass is assessed as % of initial mass (n=3). **G.** Oscillatory time sweep measurements of various PBP hydrogels are assessed at 37°C under a controlled strain of 1% and a frequency of 1 rad/s (n=3). **H.** Representative SEM images of PBP hydrogel with optimized concentrations of heparin show pore sizes on par with those assessed via airSEM (yellow asterisk). A close-up of the hydrogel indicates the presence of dense fibril-looking areas (yellow squares on right) (left scale bar: 10 μ m, right scale bar: 5 μ m).

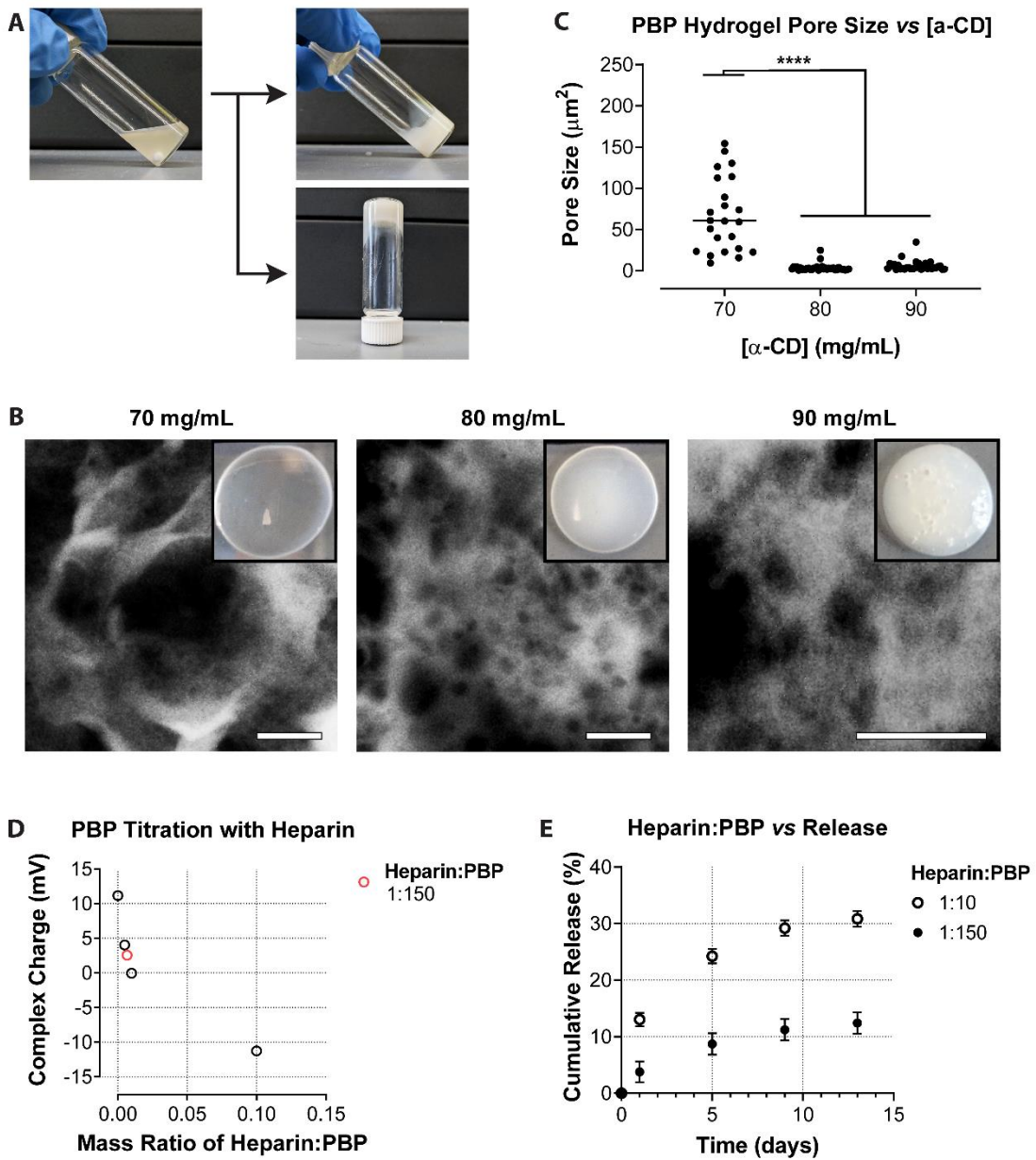
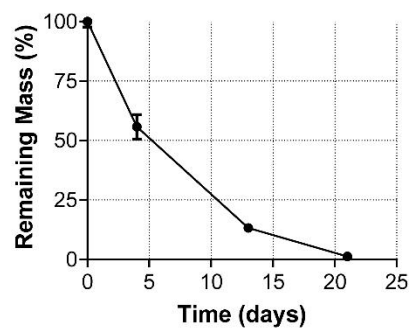
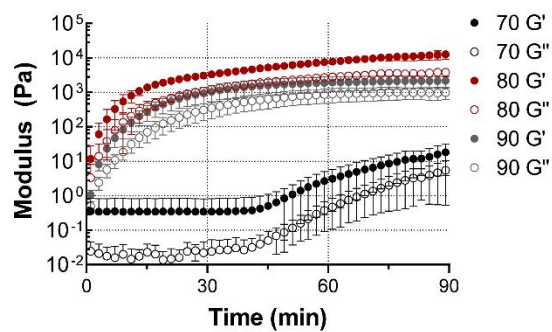


Figure 30 continued

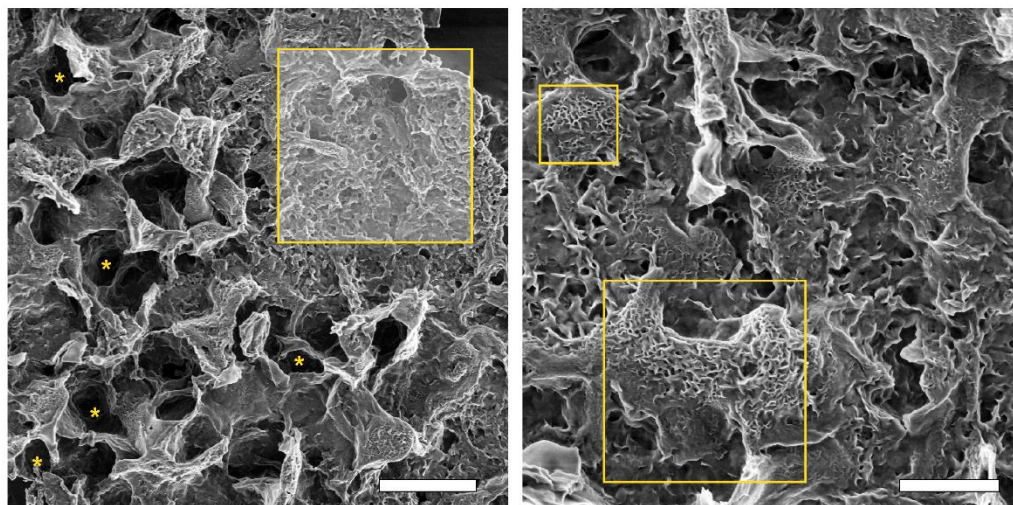
F PBP Hydrogel Degradation



G [α CD] vs PBP Hydrogel Gelation



H



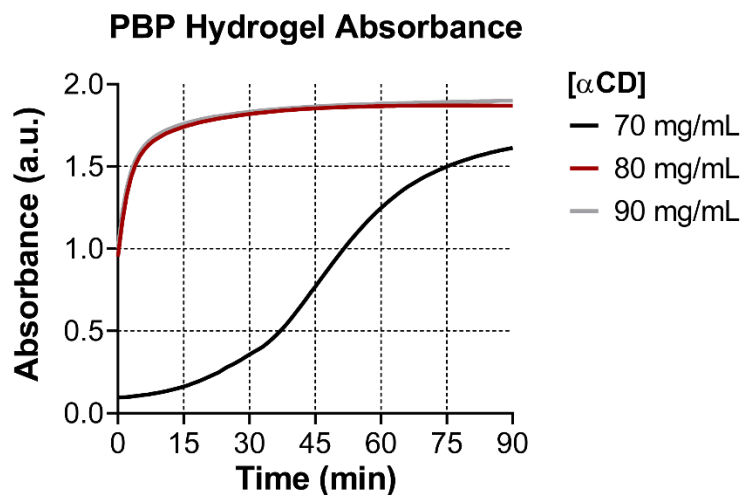


Figure 31. PBP Hydrogel Gelation Kinetics. PBP hydrogels of various $[\alpha\text{CD}]$ are prepared in 96 well plates and examined for changes in opacity at 37°C over time. Absorbance readings are made every minute at 450 nm.

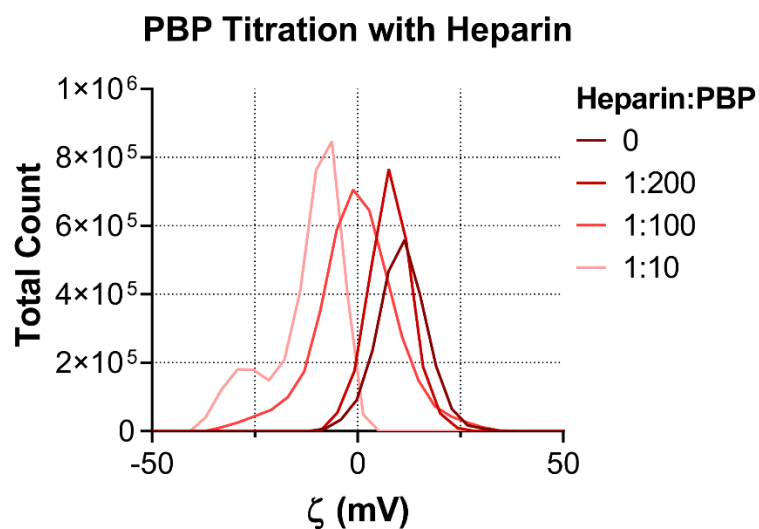


Figure 32. PBP Titration with Varying Mass Ratios of Heparin. Heparin:PBP (mass ratio) complexes were prepared in deionized water and analyzed for their zeta potential.

10% heparin (mass ratio compared to PBP), we see a quicker release over the course of 2 weeks (**Figure 30E**). Using this approach, we determined that a

mass ratio of 1:150 = heparin:PBP would yield slightly positively-charged complexes (2.55 ± 0.07 mV), which would ensure an excess of PBP. The corresponding release of IL-12 from PBP hydrogels prepared with this ratio of heparin indeed shows a slower release over the same time frame. The degradation of the PBP hydrogel in sink conditions exhibits a first-order decrease, with most of the gel dissipating by 20 days (**Figure 30F**).

Finally, rheological changes to the gel at 37°C are examined over 90 minutes (**Figure 30G**). The storage modulus (G') increased from *ca.* 0.35 ± 0.49 Pa to *ca.* 18.09 ± 14.16 Pa in the $[\alpha\text{CD}]_{70}$ group. On the other hand, for $[\alpha\text{CD}]_{80}$ and $[\alpha\text{CD}]_{90}$, G' increased from *ca.* 11.76 ± 15.98 to *ca.* $12,572.26 \pm 3649.42$ Pa and from *ca.* 1.06 ± 0.49 Pa to *ca.* 2151.76 ± 718.96 , respectively. The weak property of PBP hydrogel with $[\alpha\text{CD}]_{70}$ is likely attributed to the large pore sizes we observed (**Figure 30B**). Also, when comparing the other two groups, $[\alpha\text{CD}]_{80}$ not only exhibited higher G' values but a relatively smaller loss modulus (G'') of *ca.* 3780.20 ± 903.20 Pa (approximately 30% of max G'); $[\alpha\text{CD}]_{90}$ showed a G'' of *ca.* 981.06 ± 363.46 Pa (approximately 46% of max G'). The addition of excess αCD likely increases the rate at which physical crosslinks between αCD and PEG form, to the point where the resulting decrease in interpolymer chain freedom inhibits the formation of further crosslinks. Collectively taken together, we decided to utilize $[\text{PBP}] = 30$ mg/mL, $[\alpha\text{CD}] = 80$ mg/mL, and $[\text{heparin}] = 0.2$ mg/mL for all subsequent studies. An SEM image of the PBP hydrogel shows pore sizes (yellow asterisk in left figure) in agreement with those of airSEM (**Figure 30H**). Furthermore, a close up of the hydrogel indicates the presence

of dense fibril-looking areas (yellow squares in right figure), which could represent local domains of heparin bound to cationic sites of polymer as postulated by a previous study [131].

4.3.4 Hydrogel Delivery of IL-12 and α PD-1 Antibody Prolongs Survival in B16F10 Melanoma Model

As mentioned earlier, we desired to see the effect of early levels of α PD-1 antibody treatment on the efficacy of treatment. Furthermore, IgG does not load into heparin-based complex coacervates due to the lack of heparin-binding sites (**Figure 25**). While loading the α PD-1 antibody into the PBP hydrogel would achieve early but sustained release, we also desired to deliver a burst of IL-12 to prime the immune system followed by a steady release. To this end, we added 30% of total IL-12 together with α PD-1 antibody in the PBP hydrogel. The remaining 70% of IL-12 was encapsulated into complex coacervates, the efficacy of which was previously demonstrated (Chapter 2). The release profile of α PD-1 antibody was modeled using IgG conjugated with Alexa Fluor 647 while the release of IL-12 was assessed using ELISA (**Figure 33**). A near zero-order release is observed for IgG over the first 10 days, eventually slowing down and reaching 100% release after 25 days. IL-12 shows a small burst release on the first day, and then exhibits a slower release throughout the duration of the study. The release was carried out in sink conditions, which is in contrast to a subcutaneous environment with less water content. On the other hand, the *in-vivo* environment is conducive for quicker degradation of the hydrogel. Together, we expect the actual release *in-vivo* to be somewhere between the two extremes.

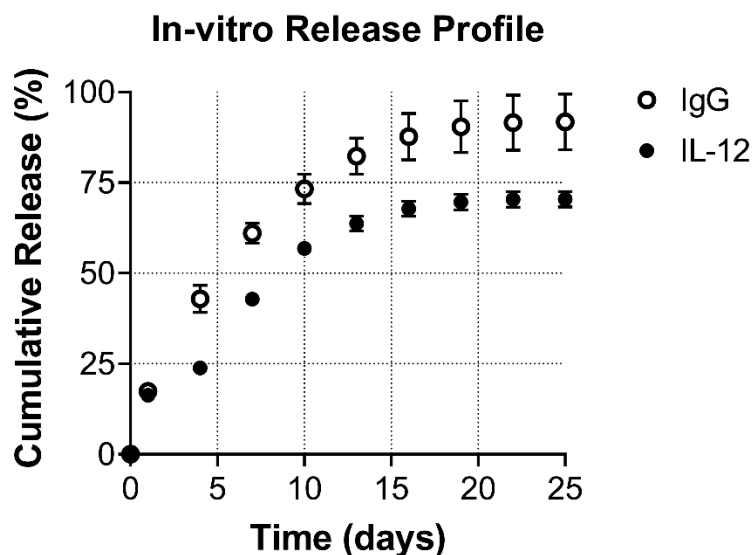
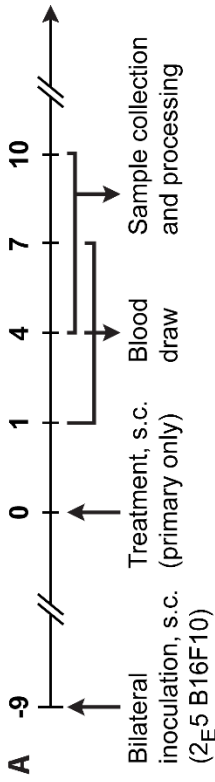


Figure 33. *In-vitro* Release Profile of IL-12 and IgG. 500 ng of IL-12 and 100 μ g of IgG are loaded into composite hydrogels of PBP and coacervate. Release was carried out in 0.9% saline with 0.1% BSA at 37°C (n=4). IL-12 was analyzed via ELISA while IgG-647 was measured via fluorescence intensity according to its respective standard curve.

The efficacy of the IL-12/ α PD-1 PBP hydrogels on melanoma were assessed *in-vivo* using a syngeneic B16F10 murine model (**Figure 34A**). Age-matched female mice were inoculated with 200,000 B16F10 cells and randomized according to size 9 days later; the average tumor size at the point of treatment was 25-50 mm². Mice were treated with a single injection of one of the following: 1) PBP hydrogel loaded with 30 μ g of IL-12 and approximately 130 μ g of α PD-1 antibody (G1), 2) IL-12 and α PD-1 antibody in saline (G2), 3) PBP hydrogel without IL-12 and α PD-1 antibody (G3), and 4) saline (G4). Treatments were only given to one primary site. Blood was drawn and samples were collected as indicated. Over the course of the study, we observed a significant inhibition of tumor growth at both the primary and contralateral sites

Figure 34. Controlled Delivery of IL-12/ α PD-1 Antibody *In-vivo*. **A.** Timeline of *in-vivo* experiments. 6-8 week old female C57BL/6J mice are bilaterally inoculated with subcutaneous injections of 200,000 B16F10 cells. 100 μ L of treatment was given only to one site (primary). Tumor sizes were measured every two days. Blood and samples were collected as indicated. **B.** Tumor size was tracked for both primary and contralateral sites over time (Controlled Delivery (G1): n=12, Bolus Treatment (G2): n=8, Empty Vehicle (G3): n=8, No Treatment (G4): n=5, mean \pm SD). **C.** Kaplan-Meier survival curves indicate significant differences compared to mice receiving controlled delivery treatments; arrow indicates time of treatment (n=4 for all groups, log-rank test, *p<0.05, **p<0.01, ****p<0.0001). Serum samples were analyzed for **D.** IL-12, **E.** α PD-1 antibody, and **F.** IFN- γ on days 1, 4, and 7 post-treatment. Significance was assessed compared to mice receiving no treatment (D1: n=6, D4: n=6, D7: n=4, mean \pm SD, ordinary one-way ANOVA with post-hoc Tukey correction for multiple comparisons, *p<0.05, **p<0.01, ***p<0.001, ****p<0.0001, #p<0.05 between G1 and G2 on D7). **G.** Intratumoral levels of IL-12 on days 4 and 10 post-treatment were analyzed after tumor digestion (n=4, mean \pm SD, ordinary one-way ANOVA with post-hoc Tukey correction for multiple comparisons, *p<0.05, **p<0.01, ***p<0.001).



Treatment Groups	Proteins	Vehicle
Controlled Delivery	IL-12, α PD-1 Ab	Coacervate, PBP hydrogel
Bolus Treatment	IL-12, α PD-1 Ab	---
Empty Vehicle	---	Coacervate, PBP hydrogel
No Treatment	---	---

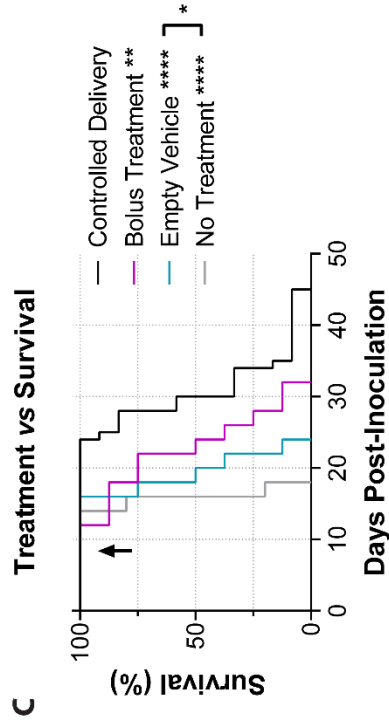
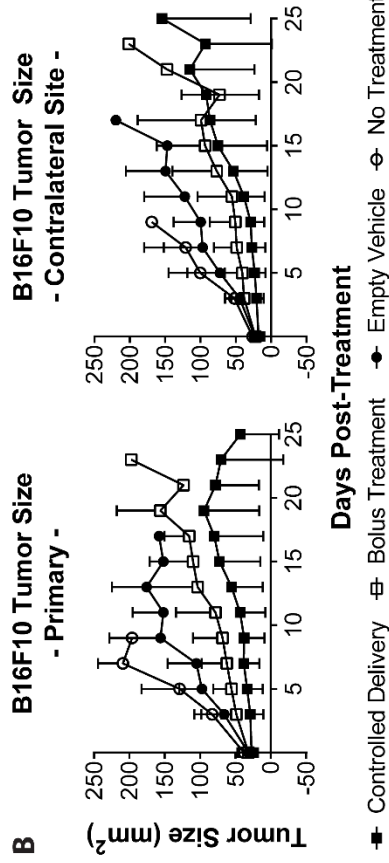
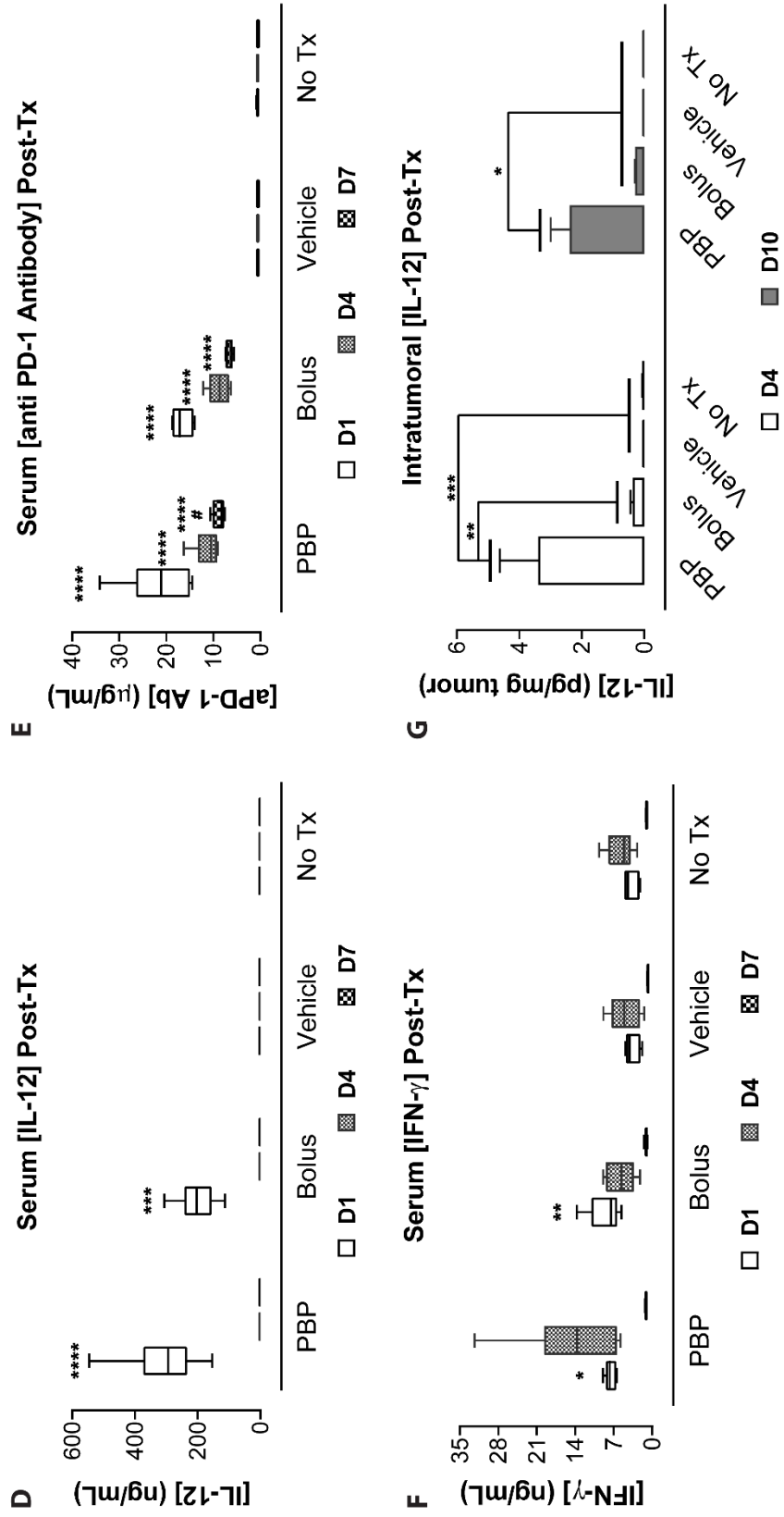


Figure 34 continued



when mice were treated with any form of IL-12 and α PD-1 antibody (**Figure 34B**). Interestingly, G3 (empty vehicle) appeared to show some level of anti-tumor activity compared to G4 and their difference was significant D7 post-treatment (**** $p < 0.0001$). Mice in G4 succumbed quickly to melanoma, which did not allow us to assess statistical significance with other groups. Importantly, while there was no significant difference in the primary tumor size of mice in G1 vs. G2, significance differences between G1 vs G3 did not carry over to G2 vs. G3 on numerous days (D5: *** vs. ns, D7: *** vs. ns, D9 and D11: *** vs. *, D13: ** vs. ns, * $p < 0.05$, ** $p < 0.01$, *** $p < 0.001$, ns: not significant). Despite the non-significance we observed in tumor size between G1 and G2, we observed a marked difference in terms of survival (**Figure 34C**). Mice receiving controlled versions of IL-12 and α PD-1 antibody showed significantly delayed death compared to mice in other groups. Also noteworthy is the significance we observed between G3 and G4, indicating that our PBP hydrogel has a small but significant effect on extending survival. We note that mice were euthanized when tumors reached a size larger than 400 mm². Other causes for euthanasia included ulceration and bleeding of the tumor, lethargy, and cachexia. In particular, mice exhibiting lethargy or cachexia generally displayed metastasis of the tumor to the draining lymph node (dLN) (**Figure 35**); YAP+ cells were assumed to be B16F10 cells in accordance to a previous study [138].

To assess the behind these differences in survival, we examined the blood for IL-12, α -PD1 antibody, and IFN- γ . Circulating levels of IL-12 showed a large significant spike in concentration one day post-treatment for mice in G1

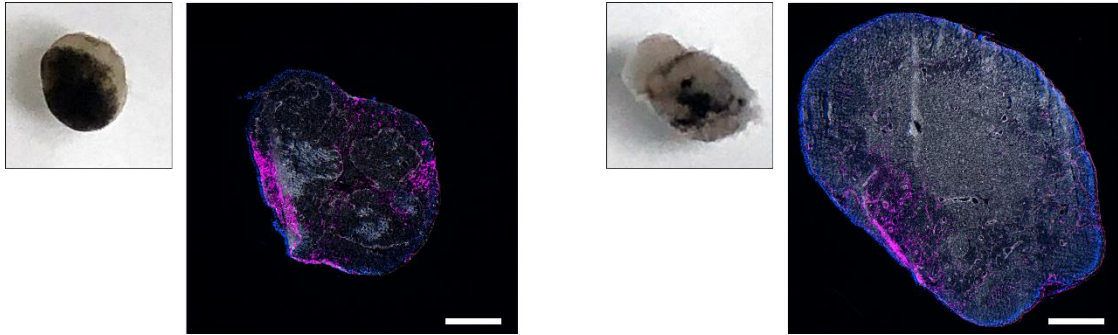


Figure 35. Metastasis of B16F10 Melanoma to dLN. Representative dLNs from sick mice were collected (left images) and sectioned at 10 µm thickness. Immunofluorescence staining of dLNs (right images) were carried out against YAP to assess metastatic tumor cells (magenta: YAP, white: f-actin, blue: nuclei, scale bar: 500 µm).

and G2 compared to those in G4 (**Figure 34D**). Mice in G3 were comparable to those in G4 and did not show any detectable levels of IL-12. Importantly, we were able to observe a drop to baseline levels of serum [IL-12] for mice in G1, which is important in minimizing inflammatory systemic effects induced by IL-12. Interestingly, the same was observed for mice receiving bolus versions of IL-12 as previously reported in humans, in which serum [IL-12] peaks at 8 hours post-injection [61]. In addition to IL-12, we also examined circulating levels of αPD-1 antibody (**Figure 34E**). Both mice in G1 and G2 showed a decrease in concentration over time, which was still significantly higher than those in G3 or G4. Of particular note, [αPD-1 antibody] for mice in G1 vs G2 move towards significance from D1 to D7, in which the differences trend towards significance on D4 ($p=0.0953$) and are significant on D7 ($\#p<0.05$). We also examined [IFN-γ] given that IL-12 induces its secretion from numerous cells (**Figure 34F**). Mice in G1 and G2 showed significantly increased levels of [IFN-γ] on the first day

post-treatment. Also, while mice in G1 show an increased level of [IFN- γ] on D4, it is not significantly different compared to that of G2, G3, and G4. Similar to IL-12, low serum [IFN- γ] is critical in minimizing systemic adverse side effects.

It should be noted that the quick drop-off in serum [IL-12] for mice in G2 is not due to the short half-life of IL-12 as mice in G1 also show the same drop. A more likely explanation is that the heparin-binding activity of IL-12 [68] could allow IL-12 to stay around in the ECM surrounding the site of subcutaneous injection. Indeed, we did not see the same complete drop in serum [α PD-1 antibody], despite its larger size that would theoretically impede its return to circulation. Given the severe adverse effects observed in early clinical trials [64], we expect different results overall if bolus IL-12 had been administered intravenously. Despite current clinical practice of using intravenous injections, we chose subcutaneous injections for bolus injections of IL-12 to minimize any potential toxicities and to provide mice in G2 with the best chance of survival. Importantly, despite low serum [IL-12] in G2, which could imply high concentrations local to the tumor, what we observed is that most of the bolus IL-12 is gone by 4 days post-treatment (**Figure 34G**). In stark contrast, intratumoral levels of IL-12 for mice in G1 are significantly higher than that of mice in all other groups, even at 10 days post-treatment. Collectively, we demonstrate that the delivery of IL-12 and α PD-1 antibody from PBP hydrogel significantly inhibits tumor growth.

4.3.5 PBP Treatment Inhibits B16F10 Intratumoral Angiogenesis and Induces Tumor Apoptosis

To better understand the mechanism behind the observed inhibition of tumor growth, we first examined the tumor environment for CD31 as a marker for angiogenesis (**Figure 36A**). Similar to the anti-angiogenic nature of PBP, we observed a significant decrease in angiogenesis on D4 when mice received the PBP hydrogel (G1 and G3). IL-12 has been shown to possess anti-angiogenic properties [78]. While we observed levels of angiogenesis to this effect (G2), we also report that our PBP hydrogel plays a role in minimizing angiogenesis, even later in the progression of the tumor (D10). Quantifying the percent of collapsed vessels on D10 indicates a significant difference between mice in G3 vs. G2 or G4 (**Figure 36C**). Mice in G1 trended towards a significantly higher proportion of collapsed vessels than those in G2 ($p=0.0881$). It should be noted that vessel collapse, while indicative of anti-angiogenesis, could prevent activated lymphocyte trafficking to the tumor. In this regard, a balance between angiogenesis and the lack thereof may be crucial. The area of blood vessels was also quantified, the results of which indicate a higher proportion of small ($<500 \mu\text{m}^2$) blood vessels in mice receiving any form of IL-12 and $\alpha\text{PD-1}$ antibody (**Figure 36D**, D4). On D10, mice in G2 and G4 possessed the highest proportion of small ($<1000 \mu\text{m}^2$) vessels, though it should be noted mice in G1 had the least total number of blood vessels (quantified from three separate immunofluorescent images; 15 in G1 vs. 26 for G2 and G3, and 60 for G4). Finally, we note an increase in lymphangiogenesis (white) on D10 in mice that did not receive any treatment (**Figure 37**, magenta: CD31, green: LYVE-1),

Figure 36. Controlled Delivery of IL-12/ α PD-1 Antibody Inhibits

Angiogenesis and Promotes Apoptosis/Necrosis of Tumor. **A.** Tumors are collected at D4 and D10 post-treatment and sectioned at 10 μ m.

Representative immunofluorescence stains against CD31 and LYVE-1 are shown (magenta: CD31, green: LYVE-1, teal: f-actin, blue: nuclei, scale bar: 200 μ m).

B. Representative H&E images at D4 post-treatment demonstrate the presence of large areas of apoptotic/necrotic tissue in mice receiving controlled delivery treatments. Apoptotic/necrotic areas are assessed to be areas of pink eosin stains without dark pigmentation and nuclei staining (scale bar: 200 μ m).

C. Proportion of collapsed blood vessels at D10 post-treatment is quantified from 3 separate immunofluorescence images (mean \pm SD, ordinary one-way ANOVA with post-hoc Tukey correction for multiple comparisons, * $p < 0.05$).

D. Vessel area at D4 and D10 post-treatment is quantified from 3 separate immunofluorescence images and analyzed via ImageJ software.

E. Apoptotic/necrotic tissue area at D4 post-treatment is quantified from 3-6 separate H&E images (mean \pm SD, ordinary one-way ANOVA with post-hoc Tukey correction for multiple comparisons, * $p < 0.05$, ** $p < 0.001$, *** $p < 0.001$, **** $p < 0.0001$).

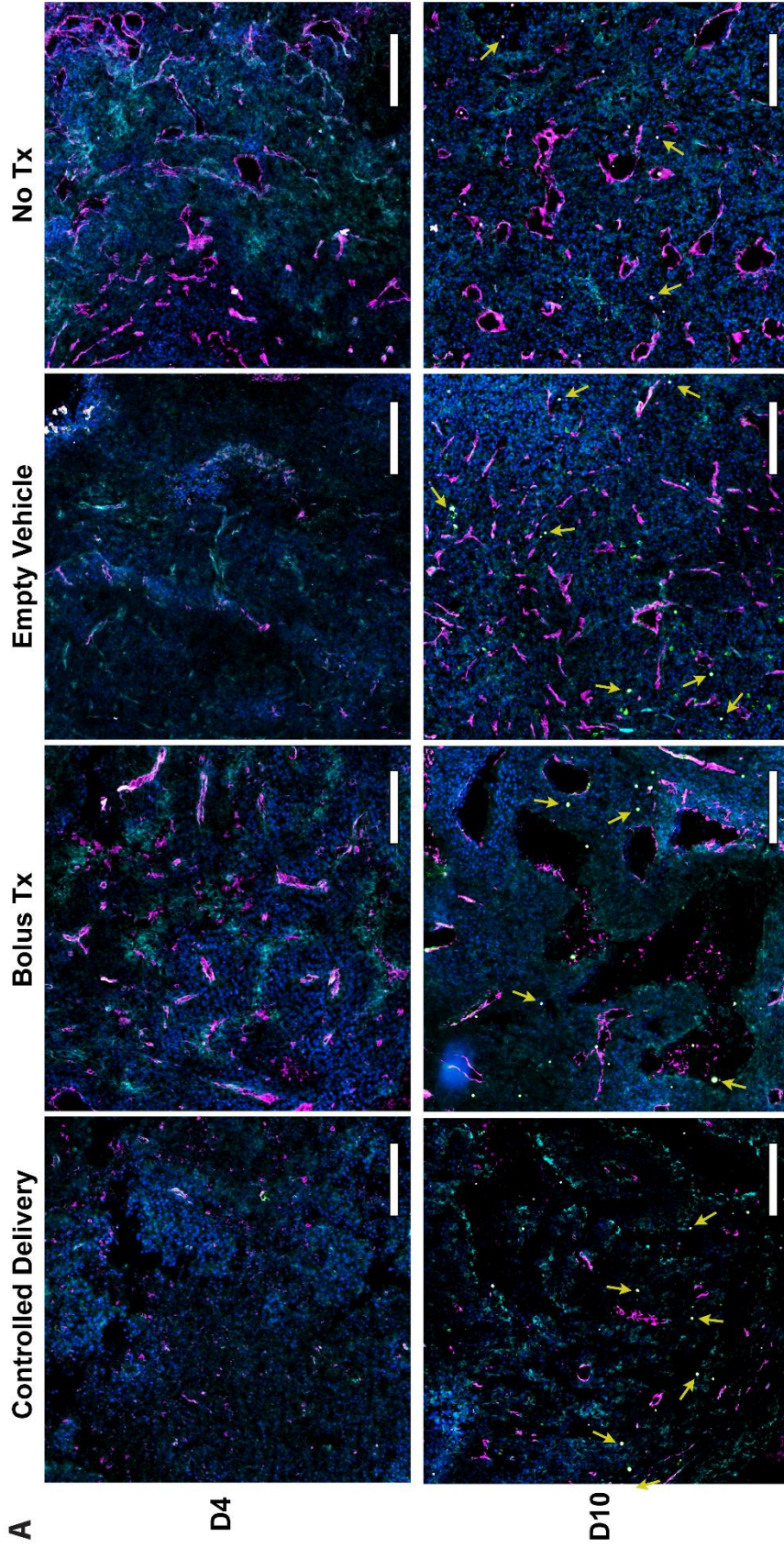
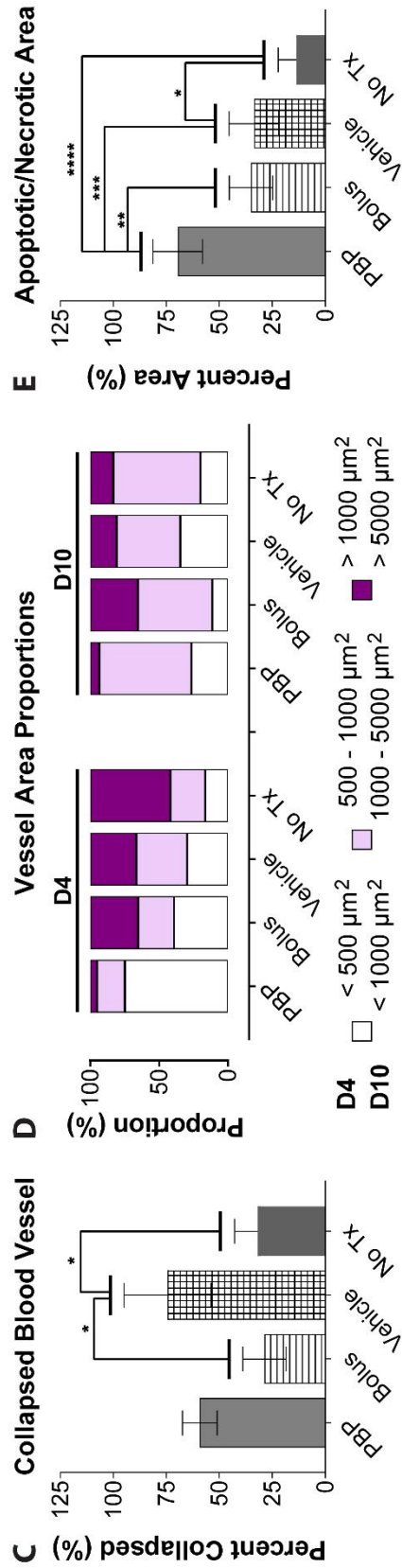
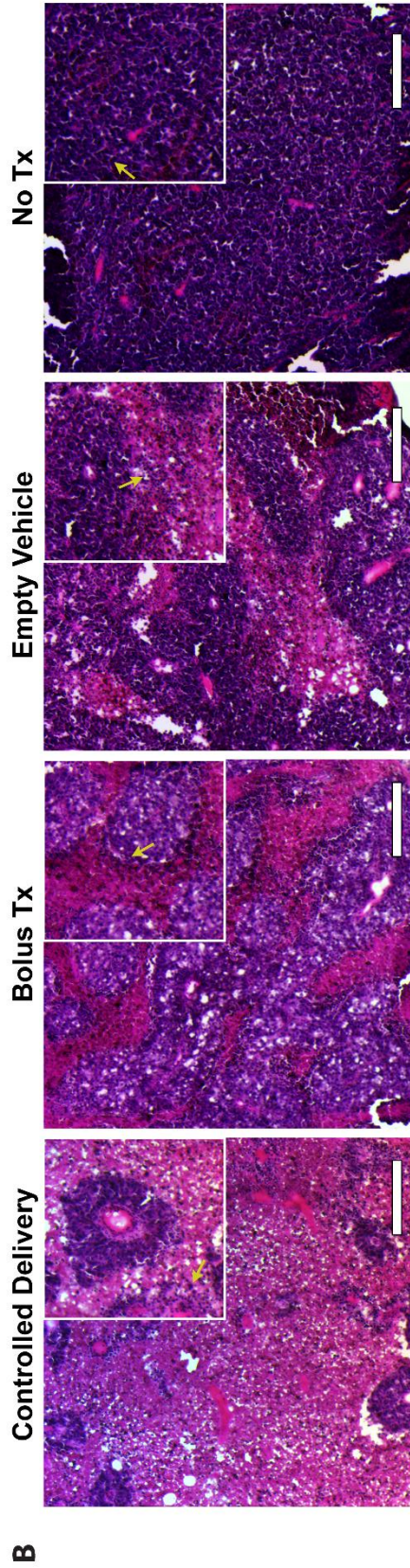


Figure 36 continued



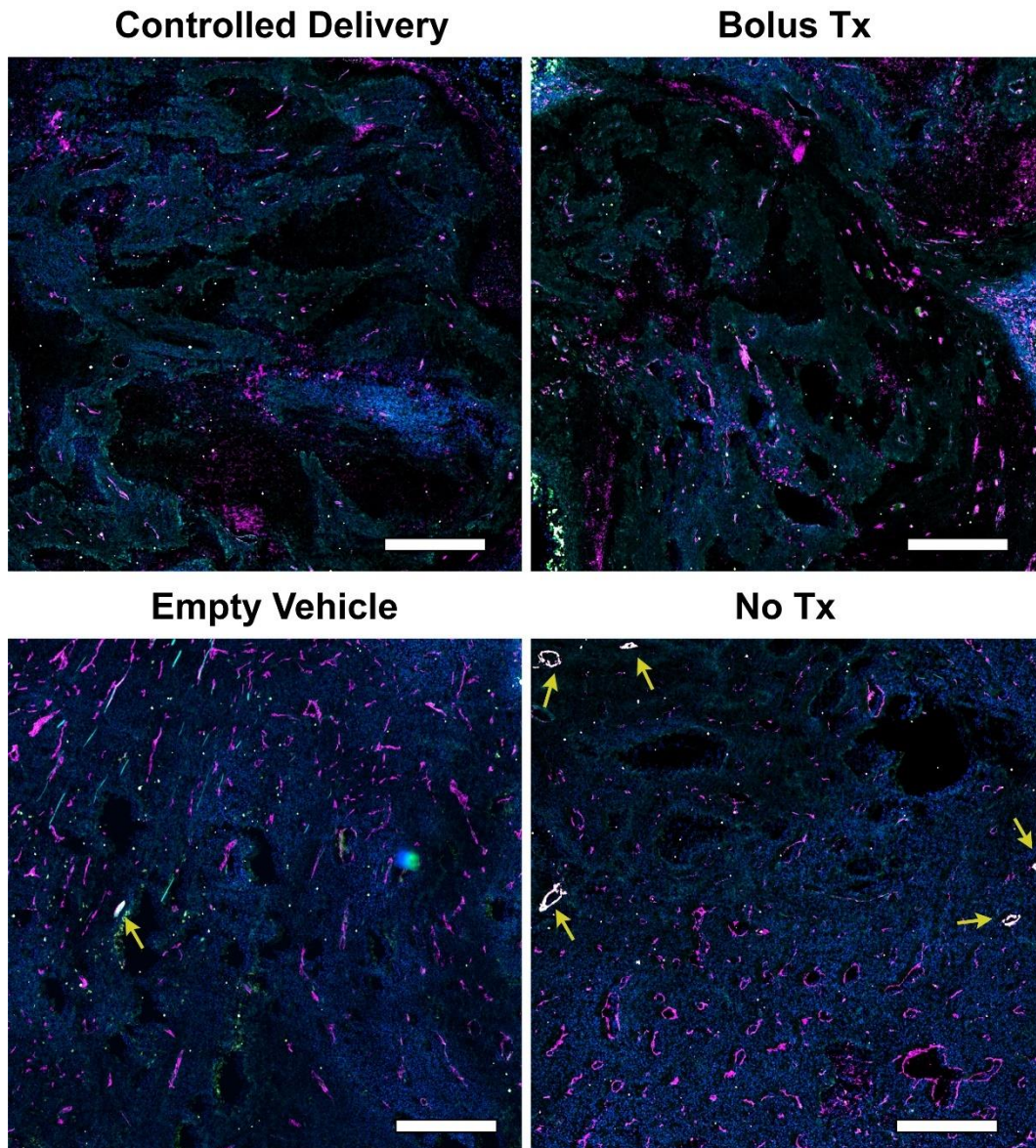


Figure 37. Controlled Delivery of IL-12/ α PD-1 Antibody Inhibits Tumor Lymphangiogenesis. Tumors from mice on D10 post-treatment are collected and sectioned at 10 μ m thickness. Representative images of immunofluorescence staining against CD31 and LYVE-1 are shown, in which yellow arrows indicate lymph vessels (magenta: CD31, green: LYVE-1, white: teal, blue: nuclei, scale bar: 500 μ m).

which could contribute to easier access to the LN for increased rates of metastasis; mice in G3 had a small number of lymph vessels while none could

be found for those in G1 and G2. On the other hand, there was no significant difference among CD31+LYVE-1+ cells that failed to form vessels (**Figure 38**).

Finally, we examined the extent of tissue apoptosis as an indicator of treatment efficacy (**Figure 36B** and **36E**). 4 days post treatment, we observed massive areas of apoptosis for mice in G1 as assessed by H&E staining, in which eosin stains in the absence of nuclei (pink areas) filled most of the image view. An image of the entire tumor for the different groups (**Figure 39**) further corroborates our observation. These apoptotic areas are different from hypoxia-induced necrosis of cells typically observed in the center of large tumors at later time points. Indeed, by D10, untreated mice took on a typical necrotic core phenotype (**Figure 40**). Mice in G1 and G2 continued to show levels of apoptotic tissue, though not to the extent as in D4. These results reveal that measurement-based survival assessments may not accurately reflect efficacy of treatments as large apoptotic/necrotic areas could significantly contribute to the perceived size of a tumor.

4.3.6 Innate and Adaptive Immune Response Plays a Role in Tumor Inhibition

To understand the cells involved in the observed inhibition, we first probed the dLN for NK1.1+ cells on D4 post-treatment (**Figure 41**). We were able to see a significant population of CD3-NK1.1+ NK cells in all mice with the exception of G4 (334 ± 155). In particular, while mice from G3 had more NK cells than those in G4 (1099 ± 214), the number of NK cells increased drastically for mice in G1 and G2. Mice from G2, which had the second highest number of NK cells (3553 ± 572), exhibited an over 10-fold increase over mice from G4.

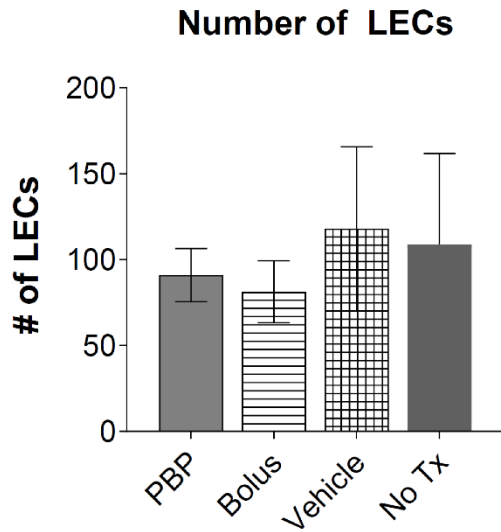


Figure 38. Number of Intratumoral LECs is Not Affected by Treatment. Tumors are analyzed for CD31+LYVE-1+ cells that have not formed vessels (numbers are quantified from at 3 separate immunofluorescence images of D10 tumors, mean \pm SD).

Nearly double the number of cells were detected from G4 (6134 ± 158), which were augmented 18.4-fold over that in untreated mice. Interestingly, a statistically-insignificant but observable increase in the number of CD3+NK1.1+ NKT cells was detected in mice from G1 (1673 ± 779) and G2 (1602 ± 1317) compared to those from G3 (180 ± 156) and G4 (155 ± 132). Immunofluorescence images of the tumors on D4 similarly show a large presence of NK1.1+ cells for mice in G1 compared to those treated with bolus versions of IL-12 and α PD-1.

We then examined the dLN and tumor environment for the presence of cytotoxic CD8 α + T cells. A large increase in the proportion of CD3+CD8 α + T cells was observed on D4 in the dLNs of mice from G1 compared to those in the other groups (**Figure 42A**). When normalized to the mass of the tumor, mice

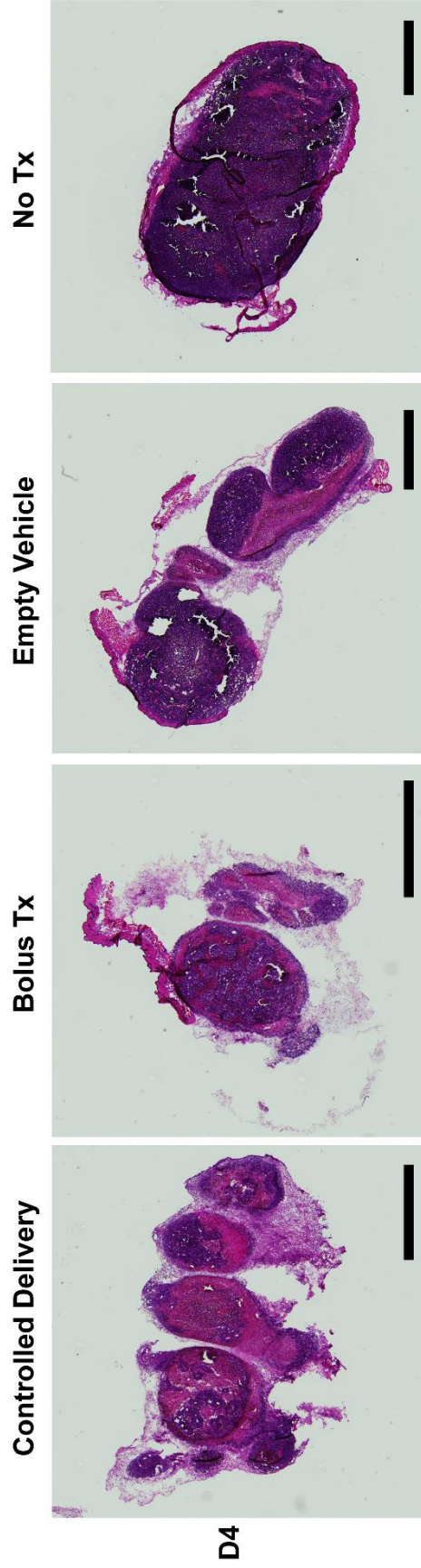


Figure 39. Controlled Delivery of IL-12/ α PD-1 Antibody Increases Apoptotic/Necrotic Areas.

H&E images of entire tumors at D4 post-treatment indicate large areas of apoptotic/necrotic tissue in mice receiving controlled delivery treatments. Apoptotic/necrotic areas are assessed to be areas of pink eosin stains without dark pigmentation and nuclei staining (scale bar: 2mm).

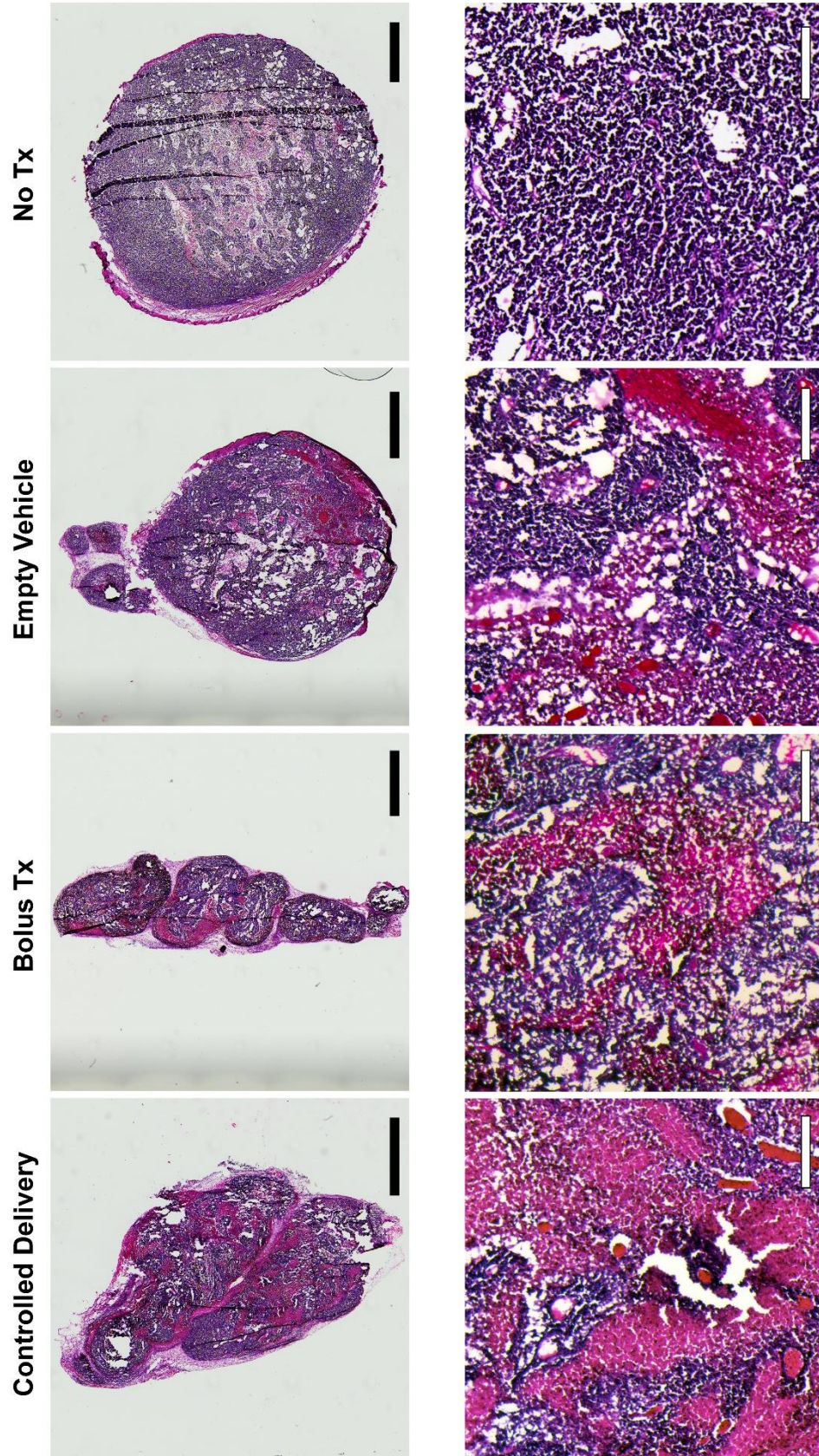


Figure 40. Increased Apoptotic/Necrotic Areas by Treatment Continues into D10 Post-treatment.

H&E images of entire tumors are taken at D10 post-treatment. Apoptotic/necrotic areas continue to occupy a large proportion of tumor for mice receiving controlled delivery treatments (top scale bar: 2 mm, bottom scale bar: 200 μ m)

from G1 continued to exhibit an increased level of CD8 α T cell proliferation (69,285 \pm 32,649); mice from G2 had less CD8 α + T cells (41,747 \pm 2,495) but more than those from G3 (18,834 \pm 16,695) and G4 (26,222 \pm 25,596). The proliferation of CD8 α + T cells was not only restricted to the dLN as large significant increases in intratumoral CD8 α + T cells were also observed on D4 for mice in G1 (34.31 \pm 1.68 cells/mg tumor; intratumoral numbers of CD8 α + T cells for G2, G3, and G4 were 24.96 \pm 3.86, 10.07 \pm 0.43, and 5.88 \pm 3.08 cells/mg tumor, respectively (G1 vs. G2: p=0.0751 and **p<0.01 for G1 vs. G3 and G4). Despite these increases, a larger proportion of CD3+CD8 α +IFN- γ + cells were observed in mice from G2 than G1 (**Figure 42B**). When accounting for tumor mass, however, mice from G1 and G2 had similar numbers of IFN- γ + T cells (15.45 \pm 2.54 vs. 18.60 \pm 3.41).

By D10, the number of CD3+CD8 α + T cells in the LN were similar for all 4 groups (data not shown). The tumor, however, continued to show a difference in CD3+CD8 α + T cells, with mice from G1 and G2 showing higher numbers per mass than those from G3 and G4 (G1: 12.26 \pm 5.08, G2: 13.56 \pm 5.86, G3: 3.33 \pm 4.21, G4: 0.37 \pm 0.07 cells/mg tumor). Immunofluorescence images of the tumor on D10 further corroborate our observations (**Figure 42C**, top). Importantly, while the total number of CD3+CD8 α + T cells dropped considerably from D4 to D10 for both G1 and G2, a higher proportion and larger number of CD3+CD8 α +IFN- γ + T cells were detected in G1 than G2 (**Figure 42C**, bottom) (G1: 2.02 \pm 0.61; G2: 1.19 \pm 0.94; G3: 0.36 \pm 0.56; G4: 0.02 \pm 0.01 cells/mg tumor). Given that IL-12 has been shown to reduce the

Figure 41. Controlled Delivery of IL-12/ α PD-1 Antibody Affects Early Immune Response Mediated by NK Cells. **A.** Representative flow cytometry plots of cells from dLNs stained for CD3 and NK1.1 indicate large presence of NK cells in mice treated with controlled delivery (n=2). **B.** Representative immunofluorescence images of tumors at D4 post-treatment show the presence of large numbers of NK cells (yellow: NKp46, white: f-actin, blue: nuclei). **C.** NK (CD3-NK1.1+) and NKT (CD3+NK1.1+) cells in dLNs are quantified from flow cytometry plots (mean \pm SD, n=2, ordinary one-way ANOVA with post-hoc Tukey correction for multiple comparisons, **p<0.01, ***p<0.001).

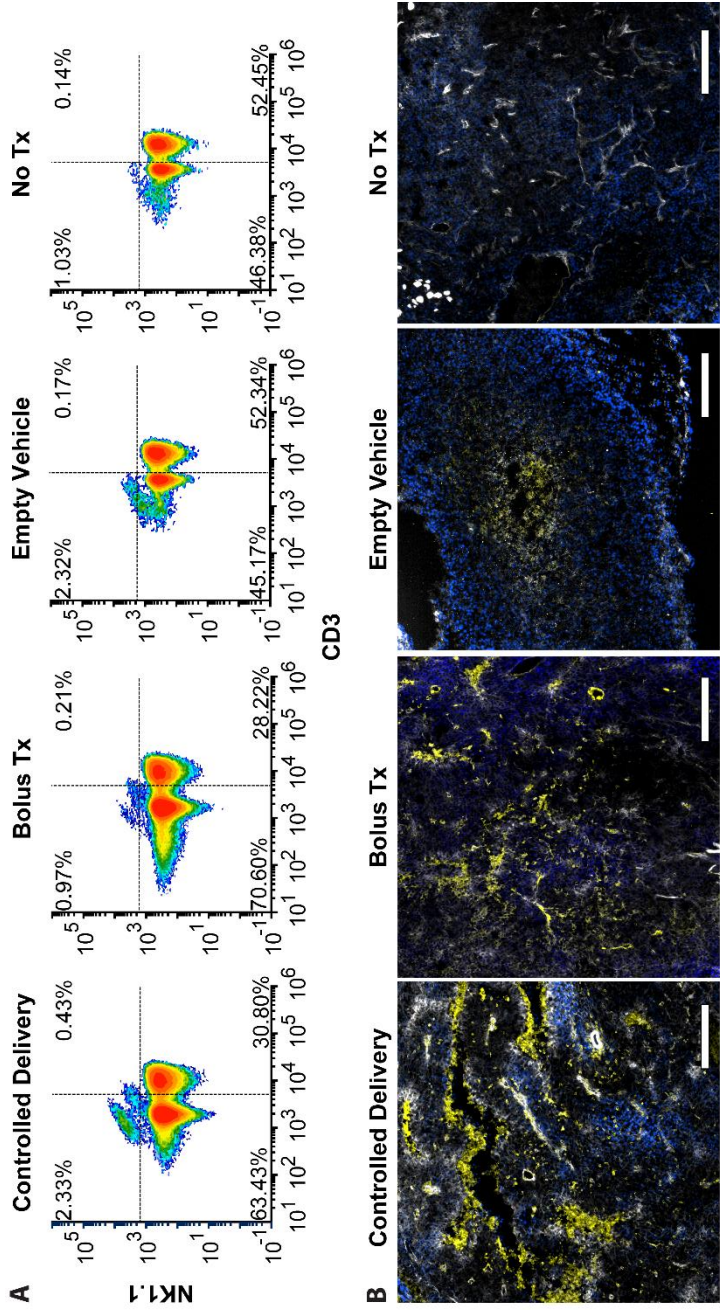
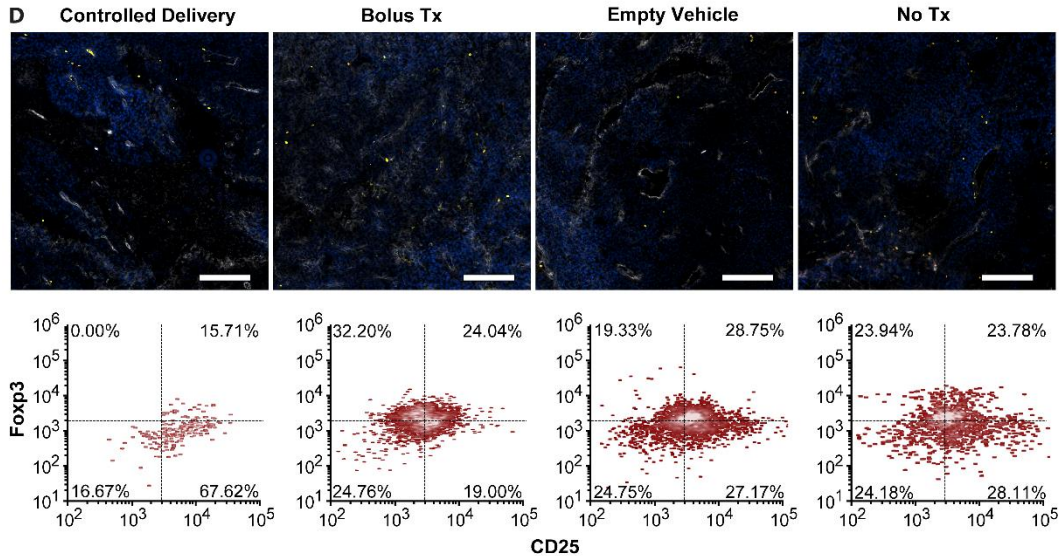
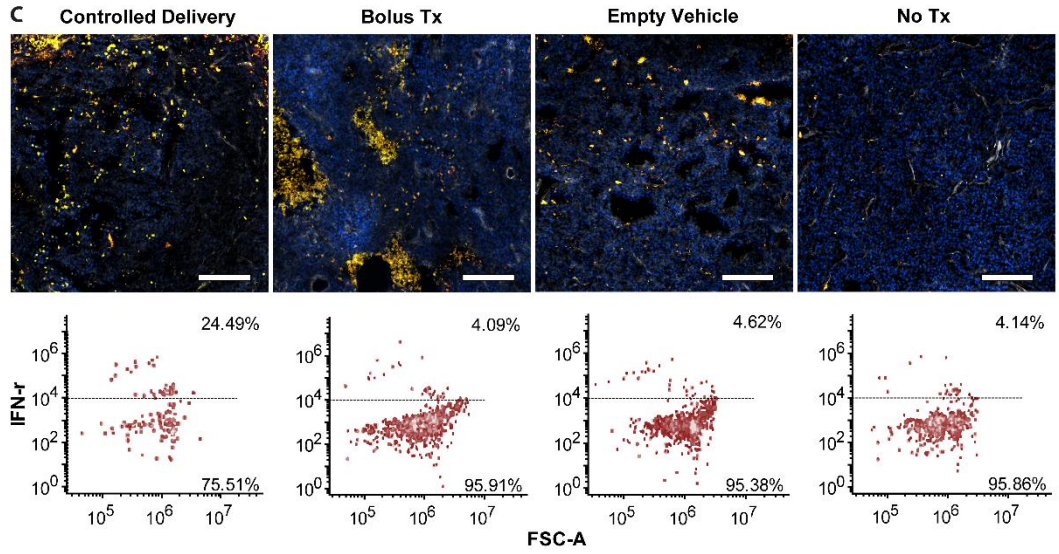
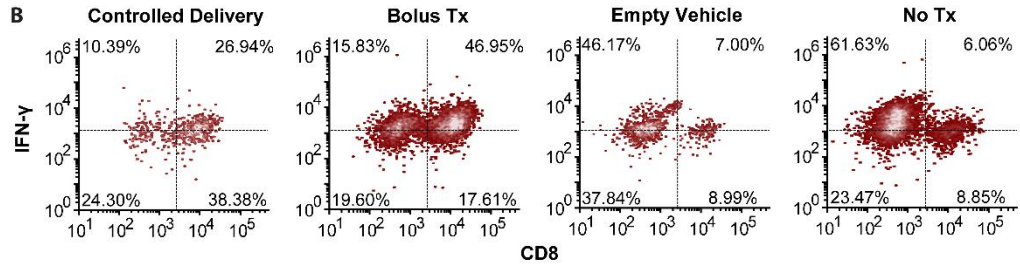
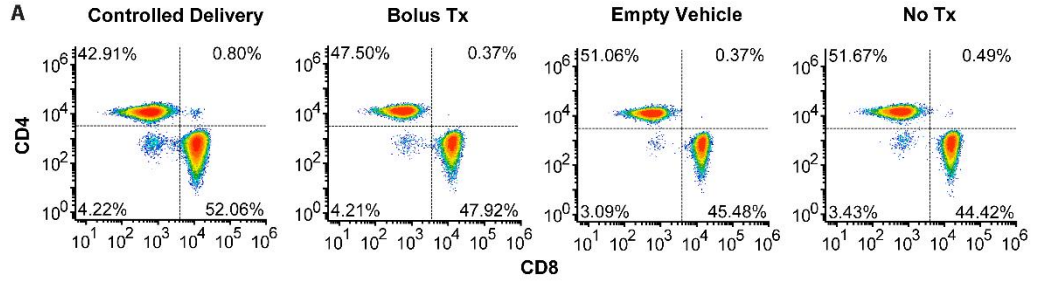


Figure 42. Controlled Delivery of IL-12/ α PD-1 Antibody Affects Adaptive Immune Response Mediated by CD8 α T Cells. **A.** Cells from dLNs at D4 post-treatment are gated on CD3 and analyzed for CD4 and CD8 α populations via flow cytometry. Quantification of data indicates the proliferation of CD3+CD8 α + cells in the dLNs of mice receiving controlled delivery treatments. **B.** At D4 post-treatment, larger proportions of intratumoral CD3+CD8 α +IFN- γ + cells were detected in mice receiving bolus forms of treatment; normalization with tumor mass, however, yields similar numbers of IFN- γ + cells per mg of tumor with mice receiving controlled delivery treatments. **C.** Representative immunofluorescence images of intratumoral CD3+CD8 α + cells and **D.** CD4+FoxP3+ cells at D10 post-treatment (upper panels, yellow: CD8 α or CD4, red: CD3 or FoxP3, white: f-actin, blue: nuclei, scale bar: 200 μ m). Though there were similar numbers of CD8 α + cells between mice receiving controlled delivery and bolus treatments, a higher proportion of CD3+CD8 α +IFN- γ + cells were detected when mice received controlled delivery treatments (C, lower panel). While more CD4+FoxP3+ cells were observed in mice receiving no treatment, there was no significant difference across groups when accounting for tumor mass.



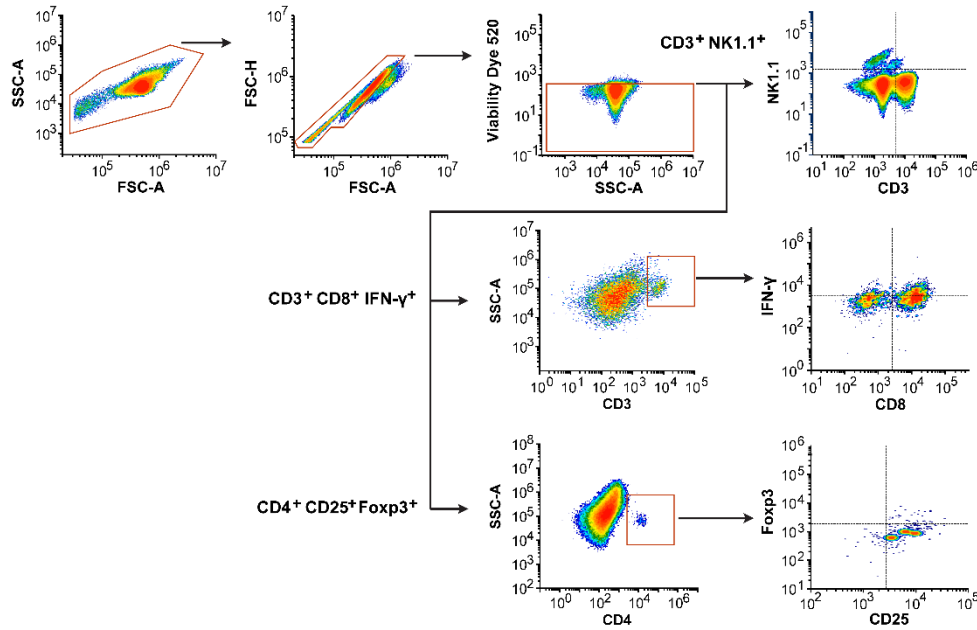


Figure 43. Representative Gating Strategy. Representative gating strategies are shown for the isolation of NK1.1+, CD8+IFN- γ +, and CD4+CD25+ cells.

proliferation of CD4+CD25+Foxp3+ Tregs, we also looked for their intratumoral presence (**Figure 42D**). Surprisingly, while there appeared to be more Tregs in mice from G4, after accounting for tumor mass, there was no significant ratio between CD3+CD8 α + T cells and CD4+CD25+Foxp3+ Tregs was greatest in mice from G1 (10.2 ± 3.48) compared to G2 (5.84 ± 4.55), G3 (5.08 ± 6.38), and G4 (0.30 ± 0.46). Gating strategies for each immune cell subtype we examined are included (**Figure 43**).

Finally, to verify the significance of each immune cell subtype we examined (e.g. NK, CD4 T cell, and CD8 T cell), we treated mice with PBP hydrogel containing IL-12 and α PD-1 antibody and knocked down either NK1.1, CD8 α , or CD4 (**Figure 44**). Mice receiving CD8 α antibodies showed a significant reduction in their survival compared to control mice (** $p < 0.01$),

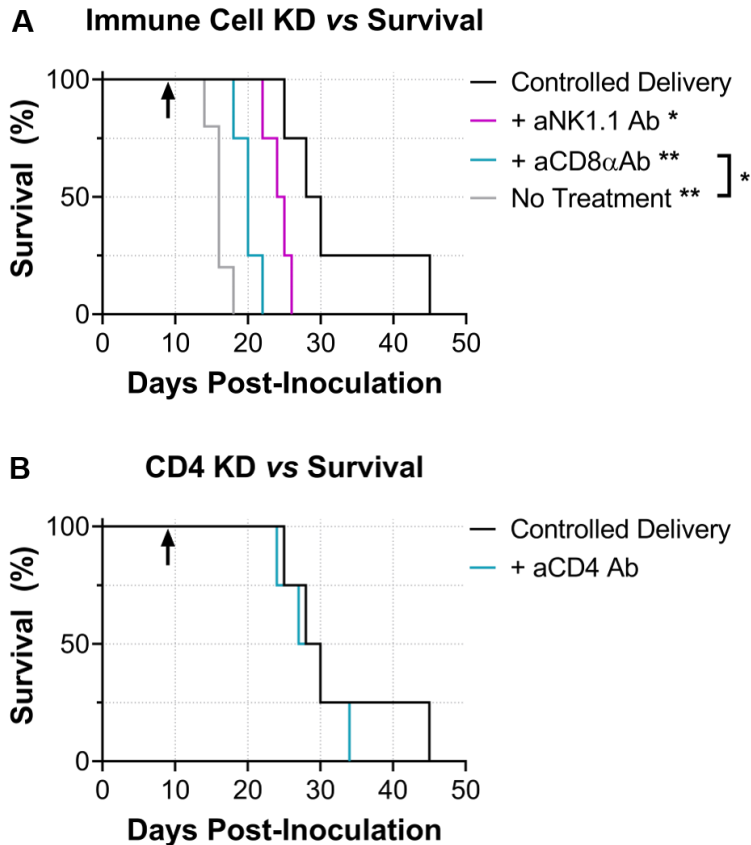


Figure 44. Effect of Immune Cell Knock-down on Survival of Mice. Mice receive intraperitoneal injections of anti-NK1.1, anti-CD8 α , or anti-CD4 antibodies one day prior to receiving controlled delivery formulations of IL-12 and α PD-1 on D0 (arrow). After an initial 200 μ g dose, mice receive 100 μ g twice a week until termination of the experiment (n=4, log-rank test, *p<0.05, **p<0.01).

indicating the large role CD8 α + T cells play in this particular study. However, these mice still showed a significantly prolonged survival compared to untreated mice (*p<0.05), indicating that other immune subsets may play a role in mitigating the inhibition of CD8 α . Mice with NK1.1 knocked down also exhibit significantly shortened survival times (*p<0.05). Surprisingly, mice in which CD4+ T cells were knocked down did not show a significant difference in survival

compared to control mice, which corroborates our observations with CD4+CD25+Foxp3+ T cells in the tumor environment (**Figure 42D**).

4.5 Conclusions

In this study, we engineer a novel polycation, PBP, with strong demonstrated anti-angiogenic capacity both *in-vitro* and *in-vivo*. The combination of PBP, α CD, and heparin results in a shear-thinning hydrogel that allows for the delivery of α PD-1 antibody. Together with heparin-based complex coacervates for the delivery of IL-12, the resulting composite hydrogel reliably delivers a potent combination of immunotherapeutic proteins as demonstrated in a preclinical B16F10 mouse melanoma model. The anti-angiogenic nature of the hydrogel combined with increased local concentrations of IL-12 play a role in diminished markers for angiogenesis, including a decrease in blood vessels and an increase in collapsed blood vessels. Large apoptotic areas were also observed in mice receiving controlled delivery treatments, attributable to the large intratumoral presence of NK and CD8 α T cells. A general inhibition of tumor growth was observed not only in primary tumor sites but also in untreated contralateral sites, suggestive of a systemic immune response. Collectively, we present data on the combined use of recombinant IL-12 and α PD-1 antibody for the first time and demonstrate its potential to significantly prolong survival in established tumors when delivered in a sustained fashion. Ultimately, we propose a reconsideration of recombinant immunotherapeutic protein therapies, and in effect, a departure from the current use of checkpoint-inhibitor-based monotherapy towards a complementary combinatory approach.

Chapter 5.

Conclusions and Future Directions

Melanoma is the deadliest type of skin cancer and continues to increase in its incidence. Traditional modes of therapy utilizing dacarbazine have proven to be ineffective, with average survival rates of less than one year [6]. These inefficiencies quickly led to the approval and use of immunotherapeutic proteins (*i.e.* IL-2) [11], yet again rapidly transitioning towards therapies dominated by the use of checkpoint inhibitors such as α CTLA-4 and α PD-1 antibodies. Despite the marked improvement in patient response rate, emerging data from both the clinic and academia points to deficits in the much-acclaimed use of checkpoint inhibitors. Repeated injections contribute to exorbitant costs that are unsustainable [31] and combination therapies with multiple checkpoint inhibitors or with chemotherapy drugs result in significant adverse side effects [30]. Equally important, the therapeutic potential of checkpoint inhibitors is restricted to a subset of patients, in which a lowly immunogenic tumor environment with sparse numbers of immune cells precludes an efficacious outcome [57, 59, 60]. Simply put, we have come full circle, in which recombinant immunotherapeutic proteins – once undesired due to their toxicity – are now needed to complement the activity of checkpoint inhibitors.

In this context, we presented work utilizing IL-12 in the course of this dissertation. IL-12 offers numerous advantages including but not limited to: 1) activation of NK cell activity [74], 2) enhanced activation of CD8+ T cells [75], 3)

DC-mediated increase in Th1 responses [76], and 4) induction of anti-angiogenic factors [78]. In conjunction with recombinant IL-12, we demonstrate the efficacy of its combination with α PD-1 antibody for the first time. Given the numerous issues of using bolus forms of immunotherapies as discussed elsewhere in this dissertation and by others, we examined the utility of injectable complex coacervate- and hydrogel-based vehicles as a means to increase local concentrations of therapy.

In the first part of this work, we examined a previously unexplored avenue of using complex coacervation to deliver immunotherapeutic proteins for anti-cancer applications. Our use of a heparin-based complex coacervate platform yielded extremely high loading efficiencies that are difficult to obtain in other particulate-type vehicles, and is amenable to injections due to the low interfacial energy exhibited between coacervates. Furthermore, we demonstrated significantly improved protection of IL-12 in a potentially harsh tumor environment as well as an increase in IL-12 bioactivity compared to bolus forms of IL-12. Using mice bearing B16F10, a highly aggressive solid tumor, we demonstrated a systemic response, in which mice receiving IL-12 coacervates showed the greatest inhibition of tumor growth. Finally, while we showed that intratumoral NKp46+, CD8 α +, and CD4+FoxP3+ cells collectively play a role in this inhibition, we underscored the need for a complementary approach with checkpoint inhibitors.

In the second part of this dissertation, we focused on the polymer used to form controlled delivery vehicles and viewed it as an opportunity to confer

functionality to the delivery vehicle itself for further anti-cancer efficacy. In particular, we focused on betaine as a pendant group given its individual roles in reducing angiogenesis [116] and preventing cancer as a supplement [109]. Motivated by these roles, we grafted betaine onto a polyester backbone to generate a novel polycation, B-PED. Despite the high cationic charge by B-PED, we observed excellent *in-vitro* and *in-vivo* biocompatibility. Of particular note, we demonstrated a dose-responsive anti-angiogenic effect *in-vitro* as well as a unimodal antibacterial response against *Staphylococcus aureus*. Finally, we assessed the potential of B-PED to form complex coacervates with heparin and determined its potential utilization as a controlled delivery device.

In the last part of this work, we set out to combine the first and second parts of this dissertation. Given the limited efficacy of delivering IL-12 alone, we proposed its combination with α PD-1 antibody. However, we observed limited encapsulation of antibody into our heparin-based complex coacervates due to the lack of heparin-binding sites on IgG. To circumvent this issue, we looked towards another injectable delivery vehicle for the delivery of α PD-1 antibody. Taking inspiration from the anti-angiogenic nature of B-PED, we further modified it to be able to form a polyrotaxane-based hydrogel. The resulting betaine- and PEG-grafted polymer (PBP) demonstrated excellent anti-angiogenic properties in both *in-vitro* and *in-vivo* assays, and upon the addition of α CD and heparin, resulted in a shear-thinning hydrogel. Collectively, we engineered a composite hydrogel platform, in which IL-12 was delivered from both complex coacervates and PBP hydrogel, and α PD-1 antibody from PBP hydrogel only. The

encapsulated IL-12/ α PD-1 antibody reliably delivered a potent combination of immunotherapeutic proteins as demonstrated in a B16F10 melanoma model, in which we observed diminished markers for angiogenesis and increased areas of apoptosis. Moreover, their controlled delivery resulted in significant increases in dLN and intratumoral NK cells, as well as increased CD8 α :Treg ratios. Collectively, we presented data on the combined use of recombinant IL-12 and α PD-1 antibody for the first time and demonstrated its potential to significantly prolong survival in mice with established tumors.

The development of injectable therapies for immunotherapeutic proteins that 1) induce the proliferation of effector cells (*i.e.* IL-12) and 2) remove their inhibitory signals (*i.e.* α PD-1 antibody) could lead to improved responses for a broader range of patients. While we successfully demonstrated the potential of combining a recombinant protein with a checkpoint inhibitor, it should be noted that complete eradication of the tumor was not observed. Along these lines, a number of questions need to be considered. First, our use of a single injection of therapy greatly reduces the total amount of administered protein. Current studies examining the use of checkpoint inhibitors and other recombinant proteins such as IL-2 utilize vastly greater amounts of protein. Due to the lack of a controlled delivery vehicle, such studies administer proteins over several injections. In this sense, increasing a single injection into even two injections could provide better therapeutic outcome in our model.

A second aspect to consider is our route of administration, in which subcutaneous injections were used for all groups. It is worth noting that many

clinical procedures as well as most academic studies use intravenous (IV) injections. However, subcutaneous injections have been shown to provide similar therapeutic benefit compared to IV injections [139, 140], which are commonly associated with increased systemic toxicities. Our choice of subcutaneous injections for bolus protein groups was based on such results, resulting in a rigorous standard for controlled delivery groups. Indeed, the same proteins delivered via IV injections most likely would have degraded faster or elicited potentially lethal side effects, perhaps leading to artificially-inflated significant differences with mice receiving controlled delivery formulations. Interestingly, fear of change and injection site reactions list the reasons behind patient reluctance to switch from IV to subcutaneous injections [141]. Granted these preferences are noted among patients with non-life-threatening conditions (*i.e.* treatment ensures survival unlike cancer), a transition from IV to subcutaneous injections is currently underway in the clinic. Along these lines, future work that assesses the delivery of immunotherapeutic proteins should similarly examine subcutaneous routes of administration as was performed in this dissertation.

Finally, the combination of surgery with our proposed treatment could lead to enhanced benefits. A concern with surgical resection is that immune cells with active anti-tumor activities are also eliminated. However, resection also removes the immunosuppressive environment. Given our results demonstrating a large increase in the proliferation of NK and T cells, assuming the preservation of dLNs, a combinatory approach of surgery with the controlled

delivery of immunotherapeutic proteins could provide better therapeutic outcomes in our murine melanoma model. Also, given that persistent high tumor antigen load plays a role in the induction of T cell exhaustion [142]– our results also demonstrate a decrease in IFN- γ -secreting functional T cells – removal of the bulk of tumor load could be beneficial. Furthermore, along these lines, combining IL-12 and α PD-1 antibody with other non-redundant factors in T cell exhaustion (e.g. α CTLA-4, α TIM-3, α CD40) [142] could render effective treatment strategies.

Ultimately, we demonstrate the use of injectable controlled delivery vehicles as a means to address a need in the localized delivery of immunotherapeutic proteins. The consequent mitigation of dose-related toxicities should allow for future studies examining more combinatory approaches with checkpoint inhibitors. We also highlight the potential benefit of using custom-tailored delivery vehicles with anti-cancer properties and propose a departure from current IV-based monotherapies.

Chapter 6.

References

- [1] Global Health Estimates 2016: Disease Burden by Cause, Age, Sex, by Country and by Region, 2000-2016., World Health Organization, Geneva 2018.
- [2] B. Cao, F. Bray, H. Beltrán-Sánchez, O. Ginsburg, S. Soneji, I. Soerjomataram, Benchmarking Life Expectancy and Cancer Mortality: Global Comparison with Cardiovascular Disease 1981-2010, *BMJ* 357 (2017).
- [3] Cancer Facts & Figures 2017, American Cancer Society, Atlanta, 2017.
- [4] H.N. Noone AM, Krapcho M, Miller D, Brest A, Yu M, Ruhl J, Tatalovich Z, Mariotto A, Lewis DR, Chen HS, Feuer EJ, Cronin KA (eds), *Seer Cancer Statistics Review, 1975-2015*. <https://seer.cancer.gov/csr/1975_2015/>, (2018).
- [5] S.B. Edge, C.C. Compton, The American Joint Committee on Cancer: The 7th Edition of the Ajcc Cancer Staging Manual and the Future of Tnm, *Annals of surgical oncology* 17(6) (2010) 1471-4.
- [6] B. Domingues, J.M. Lopes, P. Soares, H. Pópulo, Melanoma Treatment in Review, *Immunotargets Ther* 7 (2018) 35-49.
- [7] M.S. Soengas, S.W. Lowe, Apoptosis and Melanoma Chemoresistance, *Oncogene* 22(20) (2003) 3138-3151.
- [8] H.J. Gogas, J.M. Kirkwood, V.K. Sondak, Chemotherapy for Metastatic Melanoma, *Cancer* 109(3) (2007) 455-464.
- [9] D.S. Chen, I. Mellman, Oncology Meets Immunology: The Cancer-Immunity Cycle, *Immunity* 39(1) (2013) 1-10.
- [10] J. Pahl, A. Cerwenka, Tricking the Balance: Nk Cells in Anti-Cancer Immunity, *Immunobiology* 222(1) (2017) 11-20.

[11] S.A. Rosenberg, Il-2: The First Effective Immunotherapy for Human Cancer, *The Journal of Immunology* 192(12) (2014) 5451-5458.

[12] M.B. Atkins, M.T. Lotze, J.P. Dutcher, R.I. Fisher, G. Weiss, K. Margolin, J. Abrams, M. Sznol, D. Parkinson, M. Hawkins, C. Paradise, L. Kunkel, S.A. Rosenberg, High-Dose Recombinant Interleukin 2 Therapy for Patients with Metastatic Melanoma: Analysis of 270 Patients Treated between 1985 and 1993, *Journal of clinical oncology : official journal of the American Society of Clinical Oncology* 17(7) (1999) 2105-16.

[13] R. Bright, B.J. Coventry, N. Eardley-Harris, N. Briggs, Clinical Response Rates from Interleukin-2 Therapy for Metastatic Melanoma over 30 Years' Experience: A Meta-Analysis of 3312 Patients, *Journal of immunotherapy (Hagerstown, Md. : 1997)* 40(1) (2017) 21-30.

[14] W.N. D'Souza, K.S. Schluns, D. Masopust, L. Lefrancois, Essential Role for Il-2 in the Regulation of Antiviral Extralymphoid Cd8 T Cell Responses, *Journal of immunology (Baltimore, Md. : 1950)* 168(11) (2002) 5566-72.

[15] W.N. D'Souza, L. Lefrancois, Il-2 Is Not Required for the Initiation of Cd8 T Cell Cycling but Sustains Expansion, *Journal of immunology (Baltimore, Md. : 1950)* 171(11) (2003) 5727-35.

[16] L.M. D'Cruz, L. Klein, Development and Function of Agonist-Induced Cd25+Foxp3+ Regulatory T Cells in the Absence of Interleukin 2 Signaling, *Nature immunology* 6(11) (2005) 1152-9.

[17] M.F. Bachmann, A. Oxenius, Interleukin 2: From Immunostimulation to Immunoregulation and Back Again, *EMBO Rep* 8(12) (2007) 1142-1148.

[18] S. Marabondo, H.L. Kaufman, High-Dose Interleukin-2 (Il-2) for the Treatment of Melanoma: Safety Considerations and Future Directions, *Expert Opinion on Drug Safety* 16(12) (2017) 1347-1357.

[19] R.J. Sullivan, K.T. Flaherty, New Strategies in Melanoma: Entering the Era of Combinatorial Therapy, *Clinical Cancer Research* 21(11) (2015) 2424-2435.

[20] K. Wing, Y. Onishi, P. Prieto-Martin, T. Yamaguchi, M. Miyara, Z. Fehervari, T. Nomura, S. Sakaguchi, Ctla-4 Control over Foxp3⁺ Regulatory T Cell Function, *Science* 322(5899) (2008) 271-275.

[21] J.A. Seidel, A. Otsuka, K. Kabashima, Anti-Pd-1 and Anti-Ctla-4 Therapies in Cancer: Mechanisms of Action, Efficacy, and Limitations, *Front Oncol* 8 (2018) 86-86.

[22] S.R. Gordon, R.L. Maute, B.W. Dulken, G. Hutter, B.M. George, M.N. McCracken, R. Gupta, J.M. Tsai, R. Sinha, D. Corey, A.M. Ring, A.J. Connolly, I.L. Weissman, Pd-1 Expression by Tumour-Associated Macrophages Inhibits Phagocytosis and Tumour Immunity, *Nature* 545 (2017) 495.

[23] T.S. Lim, V. Chew, J.L. Sieow, S. Goh, J.P. Yeong, A.L. Soon, P. Ricciardi-Castagnoli, Pd-1 Expression on Dendritic Cells Suppresses Cd8(+) T Cell Function and Antitumor Immunity, *Oncoimmunology* 5(3) (2016) e1085146.

[24] S. Kleffel, C. Posch, S.R. Barthel, H. Mueller, C. Schlapbach, E. Guenova, C.P. Elco, N. Lee, V.R. Juneja, Q. Zhan, C.G. Lian, R. Thomi, W. Hoetzenecker, A. Cozzio, R. Dummer, M.C. Mihm, Jr., K.T. Flaherty, M.H. Frank, G.F. Murphy, A.H. Sharpe, T.S. Kupper, T. Schatton, Melanoma Cell-Intrinsic Pd-1 Receptor Functions Promote Tumor Growth, *Cell* 162(6) (2015) 1242-56.

[25] O. Talay, C.-H. Shen, L. Chen, J. Chen, B7-H1 (Pd-L1) on T Cells Is Required for T-Cell-Mediated Conditioning of Dendritic Cell Maturation, *Proceedings of the National Academy of Sciences* 106(8) (2009) 2741-2746.

[26] R.M. Gibbons Johnson, H. Dong, Functional Expression of Programmed Death-Ligand 1 (B7-H1) by Immune Cells and Tumor Cells, *Front Immunol* 8 (2017) 961-961.

[27] O. Hamid, C. Robert, A. Daud, F.S. Hodi, W.-J. Hwu, R. Kefford, J.D. Wolchok, P. Hersey, R.W. Joseph, J.S. Weber, R. Dronca, T.C. Gangadhar, A. Patnaik, H. Zarour, A.M. Joshua, K. Gergich, J. Elassaiss-Schaap, A. Algazi, C. Mateus, P. Boasberg, P.C. Tume, B. Chmielowski, S.W. Ebbinghaus, X.N. Li, S.P. Kang, A. Ribas, Safety and Tumor Responses with LAMBROLIZUMAB (Anti-Pd-1) in Melanoma, *New England Journal of Medicine* 369(2) (2013) 134-144.

[28] Unit Conversion Table. <<https://www.rndsystems.com/resources/technical-information/unit-conversion-table>>, (accessed June 12, 2019.).

[29] N. Acquavella, H. Kluger, J. Rhee, L. Farber, H. Tara, S. Ariyan, D. Narayan, W. Kelly, M. Sznol, Toxicity and Activity of a Twice Daily High-Dose Bolus Interleukin 2 Regimen in Patients with Metastatic Melanoma and Metastatic Renal Cell Cancer, *Journal of Immunotherapy* 31(6) (2008) 569-576.

[30] J. Larkin, V. Chiarion-Sileni, R. Gonzalez, J.J. Grob, C.L. Cowey, C.D. Lao, D. Schadendorf, R. Dummer, M. Smylie, P. Rutkowski, P.F. Ferrucci, A. Hill, J. Wagstaff, M.S. Carlino, J.B. Haanen, M. Maio, I. Marquez-Rodas, G.A. McArthur, P.A. Ascierto, G.V. Long, M.K. Callahan, M.A. Postow, K. Grossmann, M. Sznol, B. Dreno, L. Bastholt, A. Yang, L.M. Rollin, C. Horak, F.S. Hodi, J.D. Wolchok, Combined Nivolumab and Ipilimumab or Monotherapy in Untreated Melanoma, *N Engl J Med* 373(1) (2015) 23-34.

[31] A. Andrews, Treating with Checkpoint Inhibitors—Figure \$1 Million Per Patient, *American Health & Drug Benefits* 8(Spec Issue) (2015) 9-9.

[32] J.H. Donohue, S.A. Rosenberg, The Fate of Interleukin-2 after in Vivo Administration, *Journal of immunology* (Baltimore, Md. : 1950) 130(5) (1983) 2203-8.

[33] S. Lee, K. Margolin, Cytokines in Cancer Immunotherapy, *Cancers* (Basel) 3(4) (2011) 3856-3893.

[34] C.H. June, J.T. Warshauer, J.A. Bluestone, Is Autoimmunity the Achilles' Heel of Cancer Immunotherapy?, *Nature Medicine* 23 (2017) 540.

[35] W. Song, L. Shen, Y. Wang, Q. Liu, T.J. Goodwin, J. Li, O. Dorosheva, T. Liu, R. Liu, L. Huang, Synergistic and Low Adverse Effect Cancer Immunotherapy by Immunogenic Chemotherapy and Locally Expressed Pd-L1 Trap, *Nature Communications* 9(1) (2018) 2237.

[36] M.A. Postow, J. Chesney, A.C. Pavlick, C. Robert, K. Grossmann, D. McDermott, G.P. Linette, N. Meyer, J.K. Giguere, S.S. Agarwala, M. Shaheen, M.S. Ernstoff, D. Minor, A.K. Salama, M. Taylor, P.A. Ott, L.M. Rollin, C. Horak, P. Gagnier, J.D. Wolchok, F.S. Hodi, Nivolumab and Ipilimumab Versus Ipilimumab in Untreated Melanoma, *New England Journal of Medicine* 372(21) (2015) 2006-2017.

[37] S. Rahimian, M.F. Fransen, J.W. Kleinovink, M. Amidi, F. Ossendorp, W.E. Hennink, Polymeric Microparticles for Sustained and Local Delivery of Anticd40 and Antictla-4 in Immunotherapy of Cancer, *Biomaterials* 61 (2015) 33-40.

[38] H.C. Hill, T.F. Conway, M.S. Sabel, Y.S. Jong, E. Mathiowitz, R.B. Bankert, N.K. Egilmez, Cancer Immunotherapy with Interleukin 12 and Granulocyte-Macrophage Colony-Stimulating Factor-Encapsulated Microspheres,

Coinduction of Innate and Adaptive Antitumor Immunity and Cure of Disseminated Disease 62(24) (2002) 7254-7263.

[39] O.A. Ali, D. Emerich, G. Dranoff, D.J. Mooney, In Situ Regulation of Dc Subsets and T Cells Mediates Tumor Regression in Mice, *Science translational medicine* 1(8) (2009) 8ra19-8ra19.

[40] O.A. Ali, N. Huebsch, L. Cao, G. Dranoff, D.J. Mooney, Infection-Mimicking Materials to Program Dendritic Cells in Situ, *Nature Materials* 8 (2009) 151.

[41] C. Wang, J. Wang, X. Zhang, S. Yu, D. Wen, Q. Hu, Y. Ye, H. Bomba, X. Hu, Z. Liu, G. Dotti, Z. Gu, In Situ Formed Reactive Oxygen Species-Responsive Scaffold with Gemcitabine and Checkpoint Inhibitor for Combination Therapy, *Science translational medicine* 10(429) (2018) eaan3682.

[42] R.S. Riley, C.H. June, R. Langer, M.J. Mitchell, Delivery Technologies for Cancer Immunotherapy, *Nature Reviews Drug Discovery* 18(3) (2019) 175-196.

[43] W.B. Liechty, D.R. Kryscio, B.V. Slaughter, N.A. Peppas, Polymers for Drug Delivery Systems, *Annu Rev Chem Biomol Eng* 1 (2010) 149-173.

[44] H. Chu, N.R. Johnson, N.S. Mason, Y. Wang, A [Polycation:Heparin] Complex Releases Growth Factors with Enhanced Bioactivity, *Journal of Controlled Release* 150(2) (2011) 157-163.

[45] H. Chu, J. Gao, C.-W. Chen, J. Huard, Y. Wang, Injectable Fibroblast Growth Factor-2 Coacervate for Persistent Angiogenesis, *Proceedings of the National Academy of Sciences* 108(33) (2011) 13444-13449.

[46] N.R. Johnson, Y. Wang, Controlled Delivery of Heparin-Binding Egf-Like Growth Factor Yields Fast and Comprehensive Wound Healing, *Journal of Controlled Release* 166(2) (2013) 124-129.

[47] H.K. Awada, D.W. Long, Z. Wang, M.P. Hwang, K. Kim, Y. Wang, A Single Injection of Protein-Loaded Coacervate-Gel Significantly Improves Cardiac Function Post Infarction, *Biomaterials* 125 (2017) 65-80.

[48] W.C.W. Chen, B.G. Lee, D.W. Park, K. Kim, H. Chu, K. Kim, J. Huard, Y. Wang, Controlled Dual Delivery of Fibroblast Growth Factor-2 and Interleukin-10 by Heparin-Based Coacervate Synergistically Enhances Ischemic Heart Repair, *Biomaterials* 72 (2015) 138-151.

[49] P. Berraondo, I. Etxeberria, M. Ponz-Sarvisé, I. Melero, Revisiting Interleukin-12 as a Cancer Immunotherapy Agent, *Clinical Cancer Research* 24(12) (2018) 2716-2718.

[50] C.R. Day, S.A. Kempson, Betaine Chemistry, Roles, and Potential Use in Liver Disease, *Biochimica et Biophysica Acta (BBA) - General Subjects* 1860(6) (2016) 1098-1106.

[51] R. Bingula, C. Dupuis, C. Pichon, J.Y. Berthon, M. Filaire, L. Pigeon, E. Filaire, Study of the Effects of Betaine and/or C-Phycocyanin on the Growth of Lung Cancer A549 Cells in Vitro and in Vivo, *Journal of Oncology* (2016) 11.

[52] S. Sun, X. Li, A. Ren, M. Du, H. Du, Y. Shu, L. Zhu, W. Wang, Choline and Betaine Consumption Lowers Cancer Risk: A Meta-Analysis of Epidemiologic Studies, *Scientific Reports* 6 (2016) 35547.

[53] R.F. Zhou, X.L. Chen, Z.G. Zhou, Y.J. Zhang, Q.Y. Lan, G.C. Liao, Y.M. Chen, H.L. Zhu, Higher Dietary Intakes of Choline and Betaine Are Associated with a Lower Risk of Primary Liver Cancer: A Case-Control Study, *Scientific Reports* 7 (2017) 9.

[54] M.C. Brunner, C.A. Chambers, F.K.-M. Chan, J. Hanke, A. Winoto, J.P. Allison, Ctl α -4-Mediated Inhibition of Early Events of T Cell Proliferation, *The Journal of Immunology* 162(10) (1999) 5813-5820.

[55] H. Nishimura, M. Nose, H. Hiai, N. Minato, T. Honjo, Development of Lupus-Like Autoimmune Diseases by Disruption of the Pd-1 Gene Encoding an Itim Motif-Carrying Immunoreceptor, *Immunity* 11(2) (1999) 141-151.

[56] G.J. Freeman, A.J. Long, Y. Iwai, K. Bourque, T. Chernova, H. Nishimura, L.J. Fitz, N. Malenkovich, T. Okazaki, M.C. Byrne, H.F. Horton, L. Fouser, L. Carter, V. Ling, M.R. Bowman, B.M. Carreno, M. Collins, C.R. Wood, T. Honjo, Engagement of the Pd-1 Immunoinhibitory Receptor by a Novel B7 Family Member Leads to Negative Regulation of Lymphocyte Activation, *The Journal of Experimental Medicine* 192(7) (2000) 1027.

[57] J. Haanen, Converting Cold into Hot Tumors by Combining Immunotherapies, *Cell* 170(6) (2017) 1055-1056.

[58] G. Yu, Y. Wu, W. Wang, J. Xu, X. Lv, X. Cao, T. Wan, Low-Dose Decitabine Enhances the Effect of Pd-1 Blockade in Colorectal Cancer with Microsatellite Stability by Re-Modulating the Tumor Microenvironment, *Cellular & Molecular Immunology* 16(4) (2019) 401-409.

[59] H. Tang, J. Qiao, Y.X. Fu, Immunotherapy and Tumor Microenvironment, *Cancer letters* 370(1) (2016) 85-90.

[60] K.M. Mahoney, P.D. Rennert, G.J. Freeman, Combination Cancer Immunotherapy and New Immunomodulatory Targets, *Nature reviews. Drug discovery* 14(8) (2015) 561-84.

[61] E. Bajetta, M. Del Vecchio, R. Mortarini, R. Nadeau, A. Rakhit, L. Rimassa, C. Fowst, A. Borri, A. Anichini, G. Parmiani, Pilot Study of Subcutaneous Recombinant Human Interleukin 12 in Metastatic Melanoma, *Clinical cancer research : an official journal of the American Association for Cancer Research* 4(1) (1998) 75-85.

[62] M. Ahmadzadeh, S.A. Rosenberg, Il-2 Administration Increases Cd4(+)Cd25(Hi) Foxp3(+) Regulatory T Cells in Cancer Patients, *Blood* 107(6) (2006) 2409-2414.

[63] J. Zhao, J. Zhao, S. Perlman, Differential Effects of Il-12 on Tregs and Non-Treg T Cells: Roles of Ifn- γ , Il-2 and Il-2r, *PLoS ONE* 7(9) (2012) e46241.

[64] W. Lasek, R. Zagożdżon, M. Jakobisiak, Interleukin 12: Still a Promising Candidate for Tumor Immunotherapy?, *Cancer Immunology, Immunotherapy* 63(5) (2014) 419-435.

[65] J.P. Leonard, M.L. Sherman, G.L. Fisher, L.J. Buchanan, G. Larsen, M.B. Atkins, J.A. Sosman, J.P. Dutcher, N.J. Vogelzang, J.L. Ryan, Effects of Single-Dose Interleukin-12 Exposure on Interleukin-12-Associated Toxicity and Interferon- γ Production, *Blood* 90(7) (1997) 2541-2548.

[66] S. Kim, J. Huang, Y. Lee, S. Dutta, H.Y. Yoo, Y.M. Jung, Y. Jho, H. Zeng, D.S. Hwang, Complexation and Coacervation of Like-Charged Polyelectrolytes

Inspired by Mussels, Proceedings of the National Academy of Sciences 113(7) (2016) E847-E853.

[67] J. Qin, D. Priftis, R. Farina, S.L. Perry, L. Leon, J. Whitmer, K. Hoffmann, M. Tirrell, J.J. de Pablo, Interfacial Tension of Polyelectrolyte Complex Coacervate Phases, ACS Macro Letters 3(6) (2014) 565-568.

[68] M. Hasan, S. Najjam, M.Y. Gordon, R.V. Gibbs, C.C. Rider, Il-12 Is a Heparin-Binding Cytokine, The Journal of Immunology 162(2) (1999) 1064-1070.

[69] S. Jayanthi, B.P. Koppolu, K.G. Nguyen, S.G. Smith, B.K. Felber, T.K.S. Kumar, D.A. Zaharoff, Modulation of Interleukin-12 Activity in the Presence of Heparin, Scientific reports 7(1) (2017) 5360.

[70] B.J. Zern, H. Chu, A.O. Osunkoya, J. Gao, Y. Wang, A Biocompatible Arginine-Based Polycation, Advanced Functional Materials 21(3) (2011) 434-440.

[71] T. Hattori, K. Kimura, E. Seyrek, P.L. Dubin, Binding of Bovine Serum Albumin to Heparin Determined by Turbidimetric Titration and Frontal Analysis Continuous Capillary Electrophoresis, Analytical biochemistry 295(2) (2001) 158-67.

[72] G.R. Starbeck-Miller, H.-H. Xue, J.T. Harty, Il-12 and Type I Interferon Prolong the Division of Activated Cd8 T Cells by Maintaining High-Affinity Il-2 Signaling in Vivo, The Journal of Experimental Medicine 211(1) (2014) 105-120.

[73] J. Chehimi, S.E. Starr, I. Frank, M. Rengaraju, S.J. Jackson, C. Llanes, M. Kobayashi, B. Perussia, D. Young, E. Nickbarg, Natural Killer (Nk) Cell Stimulatory Factor Increases the Cytotoxic Activity of Nk Cells from Both Healthy Donors and Human Immunodeficiency Virus-Infected Patients, The Journal of Experimental Medicine 175(3) (1992) 789-796.

[74] C. Zhang, J. Zhang, J. Niu, Z. Zhou, J. Zhang, Z. Tian, Interleukin-12 Improves Cytotoxicity of Natural Killer Cells Via Upregulated Expression of Nkg2d, Human immunology 69(8) (2008) 490-500.

[75] C.J. Henry, D.A. Ornelles, L.M. Mitchell, K.L. Brzoza-Lewis, E.M. Hiltbold, Il-12 Produced by Dendritic Cells Augments Cd8+ T Cell Activation through the

Production of the Chemokines Ccl1 and Ccl17, *Journal of immunology* (Baltimore, Md. : 1950) 181(12) (2008) 8576-8584.

[76] C. Heufler, F. Koch, U. Stanzl, G. Topar, M. Wysocka, G. Trinchieri, A. Enk, R.M. Steinman, N. Romani, G. Schuler, Interleukin-12 Is Produced by Dendritic Cells and Mediates T Helper 1 Development as Well as Interferon-Gamma Production by T Helper 1 Cells, *European journal of immunology* 26(3) (1996) 659-68.

[77] S. Suzuki, Y. Umezu, Y. Saijo, G. Satoh, Y. Abe, K. Satoh, T. Nukiwa, Exogenous Recombinant Human Il-12 Augments Mhc Class I Antigen Expression on Human Cancer Cells in Vitro, *The Tohoku journal of experimental medicine* 185(3) (1998) 223-6.

[78] A.L. Angiolillo, C. Sgadari, G. Tosato, A Role for the Interferon-Inducible Protein 10 in Inhibition of Angiogenesis by Interleukin-12, *Annals of the New York Academy of Sciences* 795 (1996) 158-67.

[79] C. Ishan, L.R. J., Heparin-Protein Interactions, *Angewandte Chemie International Edition* 41(3) (2002) 390-412.

[80] J. Yu, T. Mitsui, M. Wei, H. Mao, J.P. Butchar, M.V. Shah, J. Zhang, A. Mishra, C. Alvarez-Breckenridge, X. Liu, S. Liu, A. Yokohama, R. Trotta, G. Marcucci, Jr., D.M. Benson, T.P. Loughran, Jr., S. Tridandapani, M.A. Caligiuri, Nkp46 Identifies an Nkt Cell Subset Susceptible to Leukemic Transformation in Mouse and Human, *J Clin Invest* 121(4) (2011) 1456-1470.

[81] O. Preynat-Seauve, P. Schuler, E. Contassot, F. Beermann, B. Huard, L.E. French, Tumor-Infiltrating Dendritic Cells Are Potent Antigen-Presenting Cells Able to Activate T Cells and Mediate Tumor Rejection, *The Journal of Immunology* 176(1) (2006) 61-67.

[82] J.M. den Haan, S.M. Lehar, M.J. Bevan, Cd8(+) but Not Cd8(-) Dendritic Cells Cross-Prime Cytotoxic T Cells in Vivo, *J Exp Med* 192(12) (2000) 1685-96.

[83] J. Gummel, F. Cousin, F. Boué, Counterions Release from Electrostatic Complexes of Polyelectrolytes and Proteins of Opposite Charge: A Direct Measurement, *Journal of the American Chemical Society* 129(18) (2007) 5806-5807.

[84] D. Priftis, N. Laugel, M. Tirrell, Thermodynamic Characterization of Polypeptide Complex Coacervation, *Langmuir* 28(45) (2012) 15947-15957.

[85] T.Y. Dora Tang, C. Rohaida Che Hak, A.J. Thompson, M.K. Kuimova, D.S. Williams, A.W. Perriman, S. Mann, Fatty Acid Membrane Assembly on Coacervate Microdroplets as a Step Towards a Hybrid Protocell Model, *Nature Chemistry* 6(6) (2014) 527-533.

[86] E. Sokolova, E. Spruijt, M.M.K. Hansen, E. Dubuc, J. Groen, V. Chokkalingam, A. Piruska, H.A. Heus, W.T.S. Huck, Enhanced Transcription Rates in Membrane-Free Protocells Formed by Coacervation of Cell Lysate, *Proceedings of the National Academy of Sciences* 110(29) (2013) 11692-11697.

[87] A.M. Bakry, S. Abbas, B. Ali, H. Majeed, M.Y. Abouelwafa, A. Mousa, L. Liang, Microencapsulation of Oils: A Comprehensive Review of Benefits, Techniques, and Applications, *Comprehensive Reviews in Food Science and Food Safety* 15(1) (2016) 143-182.

[88] E. Spruijt, A.H. Westphal, J.W. Borst, M.A. Cohen Stuart, J. van der Gucht, Binodal Compositions of Polyelectrolyte Complexes, *Macromolecules* 43(15) (2010) 6476-6484.

[89] D.S. Hwang, J.H. Waite, M. Tirrell, Promotion of Osteoblast Proliferation on Complex Coacervation-Based Hyaluronic Acid – Recombinant Mussel Adhesive Protein Coatings on Titanium, *Biomaterials* 31(6) (2010) 1080-1084.

[90] S. Ishii, J. Kaneko, Y. Nagasaki, Development of a Long-Acting, Protein-Loaded, Redox-Active, Injectable Gel Formed by a Polyion Complex for Local Protein Therapeutics, *Biomaterials* 84 (2016) 210-218.

[91] C.-H. Kuo, L. Leon, E.J. Chung, R.-T. Huang, T.J. Sontag, C.A. Reardon, G.S. Getz, M. Tirrell, Y. Fang, Inhibition of Atherosclerosis-Promoting MicromRNAs Via Targeted Polyelectrolyte Complex Micelles, *Journal of Materials Chemistry B: Materials for Biology and Medicine* 2(46) (2014) 8142-8153.

[92] N. Pippa, R. Kalinova, I. Dimitrov, S. Pispas, C. Demetzos, Insulin/Poly(Ethylene Glycol)-Block-Poly(L-Lysine) Complexes: Physicochemical Properties and Protein Encapsulation, *The Journal of Physical Chemistry B* 119(22) (2015) 6813-6819.

[93] D. Vehlow, R. Schmidt, A. Gebert, M. Siebert, K.S. Lips, M. Müller, Polyelectrolyte Complex Based Interfacial Drug Delivery System with Controlled Loading and Improved Release Performance for Bone Therapeutics, *Nanomaterials* 6(3) (2016) 53.

[94] L. Baruch, M. Machluf, Alginate-Chitosan Complex Coacervation for Cell Encapsulation: Effect on Mechanical Properties and on Long-Term Viability, *Biopolymers* 82(6) (2006) 570-9.

[95] A.B. Kayitmazer, A.F. Koksall, E. Kilic Iyilik, Complex Coacervation of Hyaluronic Acid and Chitosan: Effects of Ph, Ionic Strength, Charge Density, Chain Length and the Charge Ratio, *Soft Matter* 11(44) (2015) 8605-12.

[96] D.R. Miller, S. Das, K.-Y. Huang, S. Han, J.N. Israelachvili, J.H. Waite, Mussel Coating Protein-Derived Complex Coacervates Mitigate Frictional Surface Damage, *ACS Biomaterials Science & Engineering* 1(11) (2015) 1121-1128.

[97] L. Pellegrini, D.F. Burke, F. von Delft, B. Mulloy, T.L. Blundell, Crystal Structure of Fibroblast Growth Factor Receptor Ectodomain Bound to Ligand and Heparin, *Nature* 407(6807) (2000) 1029-34.

[98] M. Teran, M.A. Nugent, Synergistic Binding of Vascular Endothelial Growth Factor- α and Its Receptors to Heparin Selectively Modulates Complex Affinity, *The Journal of biological chemistry* 290(26) (2015) 16451-62.

[99] C.W. Vander Kooi, M.A. Jusino, B. Perman, D.B. Neau, H.D. Bellamy, D.J. Leahy, Structural Basis for Ligand and Heparin Binding to Neuropilin B Domains, *Proceedings of the National Academy of Sciences* 104(15) (2007) 6152-6157.

[100] C. Butstraen, F. Salaün, Preparation of Microcapsules by Complex Coacervation of Gum Arabic and Chitosan, *Carbohydrate Polymers* 99 (2014) 608-616.

[101] P.M. de la Torre, Y. Enobakhare, G. Torrado, S. Torrado, Release of Amoxicillin from Polyionic Complexes of Chitosan and Poly(Acrylic Acid). Study of Polymer/Polymer and Polymer/Drug Interactions within the Network Structure, *Biomaterials* 24(8) (2003) 1499-506.

[102] Y. Hao, M. Zhang, J. He, P. Ni, Magnetic DNA Vector Constructed from Pdmaema Polycation and Pegylated Brush-Type Polyanion with Cross-Linkable Shell, *Langmuir* 28(15) (2012) 6448-6460.

[103] X. Meng, S.L. Perry, J.D. Schiffman, Complex Coacervation: Chemically Stable Fibers Electrospun from Aqueous Polyelectrolyte Solutions, *ACS Macro Letters* 6(5) (2017) 505-511.

[104] A. Salehi, P.S. Desai, J. Li, C.A. Steele, R.G. Larson, Relationship between Polyelectrolyte Bulk Complexation and Kinetics of Their Layer-by-Layer Assembly, *Macromolecules* 48(2) (2015) 400-409.

[105] V.S. Trubetskoy, S.C. Wong, V. Subbotin, V.G. Budker, A. Loomis, J.E. Hagstrom, J.A. Wolff, Recharging Cationic DNA Complexes with Highly Charged Polyanions for in Vitro and in Vivo Gene Delivery, *Gene Therapy* 10(3) (2003) 261-271.

[106] M.B. Burg, J.D. Ferraris, Intracellular Organic Osmolytes: Function and Regulation, *The Journal of biological chemistry* 283(12) (2008) 7309-7313.

[107] N. Kumar, N. Kishore, Protein Stabilization and Counteraction of Denaturing Effect of Urea by Glycine Betaine, *Biophysical Chemistry* 189 (2014) 16-24.

[108] M. Lever, S. Slow, The Clinical Significance of Betaine, an Osmolyte with a Key Role in Methyl Group Metabolism, *Clinical Biochemistry* 43(9) (2010) 732-744.

[109] P. Detopoulou, D.B. Panagiotakos, S. Antonopoulou, C. Pitsavos, C. Stefanadis, Dietary Choline and Betaine Intakes in Relation to Concentrations of Inflammatory Markers in Healthy Adults: The Attica Study, *The American Journal of Clinical Nutrition* 87(2) (2008) 424-430.

[110] A. Okano, N.A. Isley, D.L. Boger, Peripheral Modifications of [Ψ [Ch₂nh]Tpg₄]Vancomycin with Added Synergistic Mechanisms of Action Provide Durable and Potent Antibiotics, *Proceedings of the National Academy of Sciences* 114(26) (2017) E5052-E5061.

[111] P.G. Petronini, E.M. De Angelis, P. Borghetti, A.F. Borghetti, K.P. Wheeler, Modulation by Betaine of Cellular Responses to Osmotic Stress, *Biochemical Journal* 282(Pt 1) (1992) 69-73.

[112] I. Villa, P. Senesi, A. Montesano, A. Ferraretto, F. Vacante, A. Spinello, M. Bottani, S. Bolamperti, A. Rubinacci, L. Luzi, I. Terruzzi, Betaine Promotes Cell Differentiation of Human Osteoblasts in Primary Culture, *Journal of Translational Medicine* 15 (2017) 132.

[113] L. Munaron, S. Antoniotti, D. Lovisolo, Intracellular Calcium Signals and Control of Cell Proliferation: How Many Mechanisms?, *Journal of Cellular and Molecular Medicine* 8(2) (2004) 161-8.

[114] H. Chu, J. Gao, Y. Wang, Design, Synthesis, and Biocompatibility of an Arginine-Based Polyester, *Biotechnology Progress* 28(1) (2012) 257-264.

[115] D. Fischer, Y. Li, B. Ahlemeyer, J. Kriegelstein, T. Kissel, In Vitro Cytotoxicity Testing of Polycations: Influence of Polymer Structure on Cell Viability and Hemolysis, *Biomaterials* 24(7) (2003) 1121-31.

[116] E.Y. Yi, Y.J. Kim, Betaine Inhibits in Vitro and in Vivo Angiogenesis through Suppression of the Nf-KappaB and Akt Signaling Pathways, *International journal of oncology* 41(5) (2012) 1879-85.

[117] G. Andres, D. Leali, S. Mitola, D. Coltrini, M. Camozzi, M. Corsini, M. Belleri, E. Hirsch, R.A. Schwendener, G. Christofori, A. Alcamì, M. Presta, A Pro-Inflammatory Signature Mediates Fgf2-Induced Angiogenesis, *Journal of Cellular and Molecular Medicine* 13(8b) (2009) 2083-108.

[118] R.C. James, J.G. Pierce, A. Okano, J. Xie, D.L. Boger, Redesign of Glycopeptide Antibiotics: Back to the Future, *ACS Chemical Biology* 7(5) (2012) 797-804.

[119] F. Nederberg, Y. Zhang, J.P.K. Tan, K. Xu, H. Wang, C. Yang, S. Gao, X.D. Guo, K. Fukushima, L. Li, J.L. Hedrick, Y.-Y. Yang, Biodegradable Nanostructures with Selective Lysis of Microbial Membranes, *Nature Chemistry* 3(5) (2011) 409-414.

[120] G. Wu, Q. Yang, M. Long, L. Guo, B. Li, Y. Meng, A. Zhang, H. Wang, S. Liu, L. Zou, Evaluation of Agar Dilution and Broth Microdilution Methods to

Determine the Disinfectant Susceptibility, *Journal of Antibiotics* 68(11) (2015) 661-665.

[121] A. Kanazawa, T. Ikeda, T. Endo, A Novel Approach to Mode of Action of Cationic Biocides Morphological Effect on Antibacterial Activity, *Journal of Applied Bacteriology* 78(1) (1995) 55-60.

[122] C.G. Park, C.A. Hartl, D. Schmid, E.M. Carmona, H.J. Kim, M.S. Goldberg, Extended Release of Perioperative Immunotherapy Prevents Tumor Recurrence and Eliminates Metastases, *Science translational medicine* 10(433) (2018).

[123] S. Tugues, S.H. Burkhard, I. Ohs, M. Vrohings, K. Nussbaum, J. Vom Berg, P. Kulig, B. Becher, New Insights into Il-12-Mediated Tumor Suppression, *Cell Death Differ* 22(2) (2015) 237-246.

[124] W. Peng, C. Liu, C. Xu, Y. Lou, J. Chen, Y. Yang, H. Yagita, W.W. Overwijk, G. Lizée, L. Radvanyi, P. Hwu, Pd-1 Blockade Enhances T-Cell Migration to Tumors by Elevating Ifn- γ Inducible Chemokines, *Cancer research* 72(20) (2012) 5209-5218.

[125] C.S. Garris, S.P. Arlauckas, R.H. Kohler, M.P. Trefny, S. Garren, C. Piot, C. Engblom, C. Pfirschke, M. Siwicki, J. Gungabeesoon, G.J. Freeman, S.E. Warren, S. Ong, E. Browning, C.G. Twitty, R.H. Pierce, M.H. Le, A.P. Algazi, A.I. Daud, S.I. Pai, A. Zippelius, R. Weissleder, M.J. Pittet, Successful Anti-Pd-1 Cancer Immunotherapy Requires T Cell-Dendritic Cell Crosstalk Involving the Cytokines Ifn- γ and Il-12, *Immunity* 49(6) (2018) 1148-1161.e7.

[126] S. Dias, R. Boyd, F. Balkwill, Il-12 Regulates Vegf and Mmps in a Murine Breast Cancer Model, *International journal of cancer* 78(3) (1998) 361-5.

[127] S. Mitola, M. Strasly, M. Prato, P. Ghia, F. Bussolino, Il-12 Regulates an Endothelial Cell-Lymphocyte Network: Effect on Metalloproteinase-9 Production, *Journal of immunology (Baltimore, Md. : 1950)* 171(7) (2003) 3725-33.

[128] D.A. Canton, S. Shirley, J. Wright, R. Connolly, C. Burkart, A. Mukhopadhyay, C. Twitty, K.E. Qattan, J.S. Campbell, M.H. Le, R.H. Pierce, S. Gargosky, A. Daud, A. Algazi, Melanoma Treatment with Intratumoral Electroporation of Tavokinogene Telseplasmid (Pil-12, Tavokinogene Telseplasmid), *Immunotherapy* 9(16) (2017) 1309-1321.

[129] J.K. Fallon, A.J. Vandever, J. Schlom, J.W. Greiner, Enhanced Antitumor Effects by Combining an IL-12/Anti-DNA Fusion Protein with Avelumab, an Anti-Pd-L1 Antibody, *Oncotarget* 8(13) (2017) 20558-20571.

[130] M.P. Hwang, X. Ding, J. Gao, A.P. Acharya, S.R. Little, Y. Wang, A Biocompatible Betaine-Functionalized Polycation for Coacervation, *Soft Matter* 14(3) (2018) 387-395.

[131] X. Ding, J. Gao, H. Awada, Y. Wang, Dual Physical Dynamic Bond-Based Injectable and Biodegradable Hydrogel for Tissue Regeneration, *Journal of Materials Chemistry B* 4(6) (2016) 1175-1185.

[132] X. Ding, P.G. Miller, M.P. Hwang, J. Fu, Y. Wang, Scale-up Synthesis of a Polymer Designed for Protein Therapy, *European Polymer Journal* 117 (2019) 353-362.

[133] A. Harada, J. Li, M. Kamachi, The Molecular Necklace: A Rotaxane Containing Many Threaded α -Cyclodextrins, *Nature* 356(6367) (1992) 325-327.

[134] E.K. Go, K.J. Jung, J.M. Kim, H. Lim, H.K. Lim, B.P. Yu, H.Y. Chung, Betaine Modulates Age-Related Nf-Kappab by Thiol-Enhancing Action, *Biological & pharmaceutical bulletin* 30(12) (2007) 2244-9.

[135] A.J. Majmundar, W.J. Wong, M.C. Simon, Hypoxia-Inducible Factors and the Response to Hypoxic Stress, *Molecular cell* 40(2) (2010) 294-309.

[136] A. Harada, A. Hashizume, H. Yamaguchi, Y. Takashima, Polymeric Rotaxanes, *Chemical Reviews* 109(11) (2009) 5974-6023.

[137] G. Wenz, Cyclodextrin Polyrrotaxanes Assembled from a Molecular Construction Kit in Aqueous Solution, *Journal of Polymer Science Part A: Polymer Chemistry* 47(23) (2009) 6333-6341.

[138] C.-k. Lee, S.-h. Jeong, C. Jang, H. Bae, Y.H. Kim, I. Park, S.K. Kim, G.Y. Koh, Tumor Metastasis to Lymph Nodes Requires Yap-Dependent Metabolic Adaptation, *Science* 363(6427) (2019) 644-649.

[139] J. López-Jiménez, J. Pérez-Oteyza, A. Muñoz, C. Parra, L. Villalón, P. Ramos, M. Maldonado, J. García-Laraña, E. Otheo, E. Roldán, A. García-

Avello, J. Odriozola, Subcutaneous Versus Intravenous Low-Dose Il-2 Therapy after Autologous Transplantation: Results of a Prospective, Non-Randomized Study, *Bone Marrow Transplantation* 19(5) (1997) 429-434.

[140] M.F. Fransen, M. Sluijter, H. Morreau, R. Arens, C.J.M. Melief, Local Activation of Cd8 T Cells and Systemic Tumor Eradication without Toxicity Via Slow Release and Local Delivery of Agonistic Cd40 Antibody, *Clinical Cancer Research* 17(8) (2011) 2270-2280.

[141] D. Pollard, S. Chaplin, Subcutaneous Injection: Learning from Experience in Other Specialties, 5(1) (2018) 35.

[142] A. Schietinger, P.D. Greenberg, Tolerance and Exhaustion: Defining Mechanisms of T Cell Dysfunction, *Trends in Immunology* 35(2) (2014) 51-60.